Effects of Engine Operating Conditions on Catalyst Light-Off and Combustion Variability

by

Jan H. Baron

Dipl.-Ing., RWTH Aachen University (2014)
Diplôme d'Ingénieur, École Centrale Paris (2014)

Submitted to the Department of Mechanical Engineering
in partial fulfillment of the requirements for the degree of

Doctor of Philosophy

at the

MASSACHUSETTS INSTITUTE OF TECHNOLOGY

February 2018

Signature redacted

Author .....
Department of Mechanical Engineering
January 19, 2018

Signature redacted

Certified by .....
Wai K. Cheng
Professor of Mechanical Engineering
Thesis Supervisor

Signature redacted

Accepted by .....
Rohan Abeyaratne, Quentin Berg Professor of Mechanics
Chairman, Department Committee on Graduate Theses

Effects of Engine Operating Conditions on Catalyst Light-Off and Combustion Variability

by

Jan H. Baron

Submitted to the Department of Mechanical Engineering
on January 19, 2018, in partial fulfillment of the
requirements for the degree of
Doctor of Philosophy

Abstract

Greenhouse gas targets for passenger car internal combustion engines as well as increasingly stringent emissions legislation around the globe require innovative development approaches for future engine generations. At the same time, trade-offs can limit important design parameters necessitating fundamental understanding of the parameters involved.

Toxic tail pipe emissions of gasoline engines are often associated with the efficiency of three-way catalytic converters and the time they take to reach light-off temperature, since a well-functioning converter reduces the tail pipe emissions by up to 99 %. Previous research suggests that exhaust gas back pressure could potentially improve converter light-off, though a thorough understanding is absent. With an experimental approach, the influence of back pressure on the converter reaction kinetics was investigated with a custom-built flow bench. Subsequently, the light-off characteristic of the converter with back pressure was investigated, with a typical downsized, turbocharged four-cylinder GDI engine used to incorporate physical effects from engine operation. Based on these experimental results a converter light-off model was developed that accurately simulates converter light-off with back pressure.

Fuel consumption or greenhouse gas emissions are largely influenced by an engine's thermodynamic efficiency and its knock tendency for optimum combustion phasing. Cycle-to-cycle variation (CCV) of the combustion can potentially reduce the efficiency significantly. An experimental approach was used to derive a fundamental understanding of CCV for non-knocking combustion. A simple geometric interpretation of combustion CCV was developed by parameterization of the heat release schedule. With the developed metric, the influence of charge motion, mixture quality, and residual gas fraction on combustion CCV was quantified. Thereafter, the impact of CCV on knocking combustion was investigated. A dominant CCV being the so called hot spot, its influence on CCV of knock was simulated and quantified with experiments. Furthermore, it was shown that the knock tendency of the engine was improved substantially by strongly increased tumble charge motion for direct-injection, even though the overall influence of the hot spot on the CCV of knock was

similar. The improved knock tendency led to efficiency gains of approximately three percent.

Thesis Supervisor: Wai K. Cheng
Title: Professor of Mechanical Engineering

Acknowledgments

First and foremost I want to thank my advisor Professor Wai K. Cheng without whom I would not be writing these words today. He accepted me as a visiting student and subsequently as a PhD student into the Sloan Automotive Lab, his advice and guidance was invaluable to me throughout the years.

Many thanks to the members of my committee Professor Wai K. Cheng, Professor John B. Heywood and Professor Ahmed F. Ghoniem, who with their curiosity, patience and helpful discussions, helped me gain valuable, new insights into the internal combustion engine and created an extremely supportive work environment.

Furthermore, I want to thank the members of the Engine and Fuels Consortium Borg Warner, Fiat Chrysler, Ford and GM that supported this research. Thanks for the feedback, discussions and support from Richard Davis, and Justin Ketterer of GM, Tom Leone of Ford, Ron Reese of Fiat Chrysler, and David Roth of Borg Warner.

Thanks also to the staff, my colleagues and fellow students of the Sloan Automotive Lab at MIT for their support. And thank you to Pinar and Reshma from the Electrochemical Energy Lab at MIT.

Last but not least, I want to thank my family, my parents and my brother, who have always supported me with all the seemingly impossible ideas that I ever had. And especially my dad whose health has suffered unanticipated hardship throughout the final stage of my studies. I want to thank them, and Sandra for supporting me throughout the journey of my doctoral studies at MIT.

Contents

List of Figures

List of Tables

Chapter 1

Introduction

The emission of anthropogenic greenhouse gas (GHG) and the resulting increase in its total atmospheric GHG concentration is a major contributor to the Northern Hemisphere Temperature Anomaly or global climate change[23]. In 2014, in the United States alone the greenhouse gas emissions amounted to 6870×10^6 t of CO_2 equivalent, 26 % of which were produced by the transportation sector. Passenger cars and light-duty trucks are the largest contributor of the transportation sector with 60.2 % of the GHG emissions[21]. The US fleet was 96 % gasoline powered in 2014[15].

Burning HCs inherently produces CO_2, as the fully oxidized combustion product of the carbon atoms. And hence the amount of carbon dioxide produced for a given amount of useful work depends on the efficiency of the internal combustion engine[45]. Next to greenhouse gas an internal combustion engine also produces toxic pollutants such as unburned HCs and CO. Due to the short timescale of the combustion event in intermittent engines, the combustion is not complete leaving small quantities of these unburned or partially oxidized combustion products. At high combustion peak temperatures nitrogen oxides (NO_x) are also formed in significant amount.

In an effort to reduce the amount of toxic pollutants from combustion engines, governing bodies around the world have put legislation in place to regulate those emissions[29]. Since the amount of pollutants per unit energy produced depends on the operating condition of the engine, driving cycles have been defined that aim to represent average driving behavior. The total tail pipe emissions accumulated over the

entire driving cycle are regulated. While the specific driving profiles differ between different regulations they all have similar characteristics, i.e. cold-start, low-load and higher load operation[8]. Another common feature is that they all become more stringent with time.

The New European Driving Cycle (NEDC), and the federal test procedure (FTP75) introduced by the Environmental Protection Agency (EPA), are common driving cycles to access emissions including cold-start, that are used in their respective regions as well as many others. The CO_2 emissions are usually regulated across the fleet of all cars sold by a manufacturer. In the US this is the Corporate Average Fuel Economy (CAFE) standard, with limits of 35.5 mpg or 250 g CO_2 mile^{-1} in 2016[71].

Exhaust gas aftertreatment is usually required to meet stringent emissions regulations for toxic pollutants, since their concentration in the exhaust gas exiting the engine is usually significantly higher than the regulated limit. Gasoline engines that are operated stoichiometrically commonly use the three-way catalytic converter (TWC) for exhaust gas aftertreatment, since it was developed in 1981[47]. The toxic pollutants HC, CO and NO_x together with O_2 are converted on its catalytic surface to the non-toxic products CO_2, H_2O, and N_2.

At operating temperature, when the catalytic converter reached full "light-off", a well functioning TWC converts more than 99 % of the CO and HC species in the exhaust gas[6]. However, below the light-off point the conversion efficiency is significantly lower, so that the pollutants practically pass the converter unchanged at low temperatures, for instance at cold-start[22]. The three-way catalytic converter is usually a passive component in the exhaust system, which reaches light-off and maintains operating temperature through heat transfer from the exhaust gas passing through it.

Downsizing, and turbocharging together with direct-injection is a potentially effective measure to increase the efficiency of traditional, naturally aspirated gasoline engines and hence reduce their GHG emissions[33]. The throttle losses of a downsized engine are reduced significantly at part-load, since the smaller engine operates at relatively higher load. Resulting in increased efficiency because of similar friction losses.

However, the torque output of the smaller engine is limited by the amount of air that fits into the smaller cylinder, since the air-fuel ratio is usually fixed. The charge density can be increased by turbocharging together with an intercooler, allowing a larger amount of fuel to be burned. As a result the cylinder peak pressure and temperature increase, which can result in autoignition or engine knock[41]. To avoid the harmful effect of knock on the engine a so called knock-sensor detects autoignition and mitigates it by retarding the spark timing. A delayed spark timing, however, reduces the efficiency of the engine. A more stable combustion with little variability allows the engine to be operated closer to the knock-limit without intervention of the knock-sensor. Engine performance and efficiency at part-load also improves with higher combustion stability.

The thesis will cover two topics; first, the influence of increased exhaust back pressure on the catalytic converter light-off. The accumulated emission of toxic pollutants over the certification cycle depends strongly on the time it takes the TWC to reach light-off after cold-start. Second, it will quantify the influence of engine and operating parameters on the cycle-to-cycle variation of the combustion event in a turbocharged direct-injected gasoline engine. A smaller combustion variability allows the engine to be operated closer to the knock-limit at high loads as well as more stable combustion at part load, both increases engine efficiency and reduces GHG emissions.

Chapter 2

Part I: Exhaust Back Pressure Effect on Catalyst Light-Off

Challenges in three-way catalytic converter light-off and common solutions found in literature are described in this chapter. Furthermore it will be discussed that a detailed understanding of back pressure during light-off is practically not existent in literature and how these will be developed based on some previous preliminary research. Finally the goals and expectations of this research project will be outlined.

2.1 Introduction and Motivation

Low exhaust gas mass flow and temperature are characteristic for engine operation in a certification cycle right after cold-start. This phenomena is exacerbated for downsized, turbocharged four-cylinder engines, because of the relatively small overall swept volume of the engine and heavily throttled operation mode.

Following the cold-start in certification cycles, the engine typically idles without any external load only running engine auxiliaries such as water pump and generator. In the federal test procedure (FTP75) certification cycle, the vehicle stands still idling for 20 s followed by moderate acceleration, compare Figure 2-1. Fast Three-way catalytic converter light-off is crucial during this period as the engine out emissions pass the converter unchanged before it reaches its conversion or light-off temperature.

Once the converter reached full light-off it converts more than 99 % of the unburned hydrocarbon and carbon monoxide species in the exhaust gas. As a result more than 80 % of the regulated emissions (CO, HC, NO_x) are emitted during the first two minutes following cold-start [57].

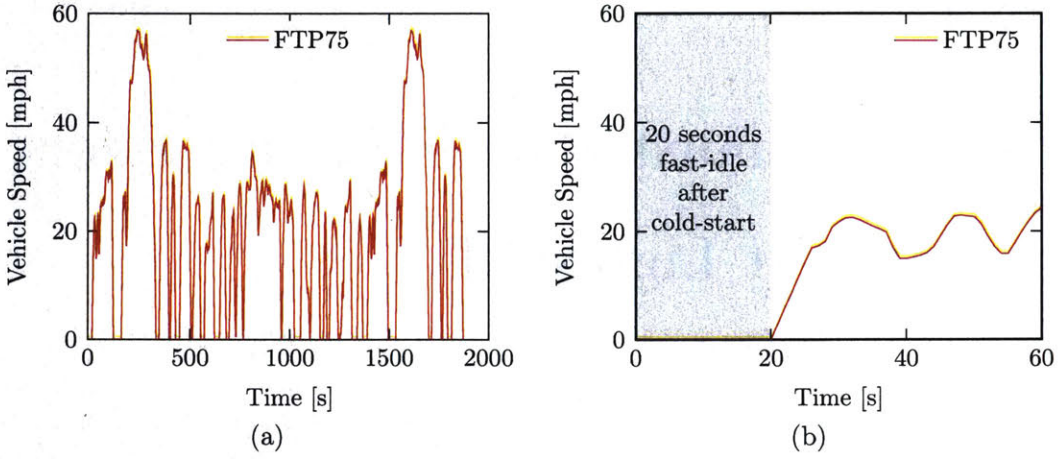

Figure 2-1: The vehicle speed profile of the FTP75 certification cycle is depicted in 2-1a throughout its entire duration of 1877 s. The initial cold-start period consisting of 20 s fast-idle is shown in 2-1b as well as the subsequent 40 s of lower load operation.

Over the last couple of decades many solutions have been proposed in various research projects and some have been implemented in stock engine calibrations or exhaust systems. Solutions range from passive to active components, while the former are heavily favored due to generally lower costs associated with these components and the relative short usage after cold-start compared to engine system lifetime. Their application and challenges as detailed in literature will be discussed in the next section.

2.2 Background and Literature Review

Many three-way catalytic converters are close coupled in current production vehicles as opposed to an underfloor configuration that was common prior to stringent emission regulations starting to be introduced towards the end of the twentieth century [57]. For naturally aspirated engines the converter is usually connected to the exhaust runner,

while it is at the turbine outlet for turbocharged vehicles, capturing exhaust gas enthalpy before it is lost to the exhaust system via heat transfer. Research by Otto et al.[57] shows that for a specific BMW production vehicle neither ultra low emission vehicle (ULEV) nor low emission vehicle (LEV) emission levels can be achieved during the FTP75 certification cycle with an underfloor converter, whereas it can be reached with a close coupled converter. At a clock time of 35 s in the FTP75 cycle, the exhaust gas temperature reaches 500 °C and 80 °C at 300 mm and 1400 mm from the exhaust valve respectively for that specific vehicle[57]. Williamson et al.[73] achieved ULEV emission levels with an underfloor converter, though only for a large engine of 3.8 L displacement volume and with an optimized cell structure, and increased and optimized precious metals loading on the surface.

Close coupled converters reach light-off temperature faster, but have to endure larger thermal stress due to higher temperatures during high load engine operation and hence are more prone to aging. Waltner et al.[72] have found that reducing the oxygen storage capacity improved the aging stability of the converter by lowering the catalyst peak temperature at high speed driving conditions. Temperatures exceeding 1050 °C can lead to drastic thermal aging of the converter and are potentially caused by ignition retard and misfire, requiring robust control mechanisms for close coupled converters[43].

Delayed spark timing is a commonly used strategy usually combined with a close coupled converter to reduce the engine light-off time at the beginning of the certification cycle[5]. In a FTP75 engine test Gallo and Guerra[22] observed that the light-off temperature they defined to be at 300 °C at converter inlet was reached 5 s earlier for a spark retard of 14 °CA compared to baseline value.

Increasing the idling speed of the engine after cold start increases the exhaust gas mass flow and hence the exhaust gas enthalpy flow rate to the three-way catalytic converter. During the so called fast-idle, an engine speed of 1200 min^{-1} is typical. However, Ball and Moser[5] have conducted research with idling speeds of up to 1700 min^{-1} ramped down towards 1500 min^{-1} at the end of the idling phase at a clock time of 20 s into the FTP75 certification cycle. With such an aggressive fast-

idling speed they achieve partial zero emission vehicle (PZEV) emission levels without an air pump, however, they note that the drop in engine speed from $1500\,\mathrm{min}^{-1}$ to $1000\,\mathrm{min}^{-1}$ when shifting into drive may be unpleasant to the driver[5].

The use of secondary air is an effective way to improve converter light-off and reduce HC emissions, though it requires an air pump as additional hardware to the engine system. That way the engine can be operated rich with hotter exhaust gas, while additional air is pumped into the exhaust manifold leading to thermal oxidation and heat release in the oxygen rich exhaust environment. Lee and Heywood[42] found that by operating the engine 20 % rich and using 100 % secondary air, a light-off time of only 4.2 s could be achieved and HC tailpipe emissions very reduced significantly by 46 % compared to baseline operating conditions. Similarly, Ball and Moser[5] found that air injection led to a raise of the exhaust gas temperature at converter inlet from 500 °C to 950 °C before the first acceleration in FTP75 certification cycle. Borland and Zhao[10] also found that thermal oxidation in the manifold using secondary air was effective in raising exhaust gas temperature and lowering the converter-in HC concentration, noting that mixture quality of secondary air and exhaust gas was paramount.

An alternative to a costly air pump for direct-injected engines is split injection[5]. Injection and ignition can be deactivated for one cylinder that serves as an air pump supplying oxygen to the exhaust system for post oxidation, while the other cylinders are operated rich with higher exhaust gas temperatures. Lang and Cheng[40] observed a 400 % increase in exhaust gas enthalpy and a 90 % reduction in converter-in HC concentration using a four-cylinder engine using one cylinder as an air pump.

Another control strategy is adjusting the valve overlap for engine systems with variable valve timing (VVT). Cedrone and Cheng[14] observed that with increased valve overlap the exhaust gas enthalpy flow rate to the converter increased, due to higher residual gas fraction, slower combustion and resulting increase in exhaust gas mass flow.

Active heating elements can potentially speed up the converter light-off significantly. However, they are less common because they are usually costly, require larger

auxiliary systems and strategies to prevent failure. An electrically heated converter was implemented in the BMW Alpina B12, a low volume production vehicle and sold in Europe and Japan[25]. Hanel et al.[25] achieved European and LEV emission levels with the electrically heated converter, which was otherwise not possible. Furthermore Pace and Presti[58] investigated operation strategies of the heated converter that would allow for lower precious metal loading of the catalytic surface especially for hybrids, in which case the heating system could be self-financing. Further reduction in light-off time for the electrically heated converter was observed by Murphy et al.[53] with an Electrically Initiated Chemically Heated Catalyst. Heat release from organic chemicals that are injected into the electrically pre-heated converter increase its temperature significantly while at the same time reducing the electrical power requirements of the pre-heated converter[53].

Up until the year 2017 to the author's knowledge, back pressure was not used as a converter light-off strategy in commercially available vehicles. Back pressure decreases engine efficiency and hence increases fuel consumption[68], making it undesirable during conventional engine operation. Preliminary research from Cedrone and Cheng[14], however, showed potential benefits of back pressure on converter light-off. Delaying the spark timing from $-2\,°\text{CA}$ aTDC to $13\,°\text{CA}$ aTDC without back pressure increased the exhaust gas enthalpy flow rate by 84 % from 5 kW to 9.2 kW, compare Figure 2-2. With back pressure the enthalpy flow rate increases further by 55 % from 9.2 kW to 14.3 kW for a spark timing of $13\,°\text{CA}$ aTDC[14]. It is important to note that the exhaust enthalpy flow rate was measured in the exhaust runner and not at converter inlet. Furthermore the results were obtained at steady state and not during a warm-up transient after cold-start. And hence further research is necessary to fully understand the influence of back pressure on the light-off behavior of the converter and the engine system as a whole following cold-start.

Similarly to current engine systems back pressure does not explicitly appear in converter light-off models as a parameter. The governing partial differential equations for heat transfer are usually expressed on a per volume basis, however, the geometric volume of the converter is independent of back pressure[36,65]. Back pressure factors

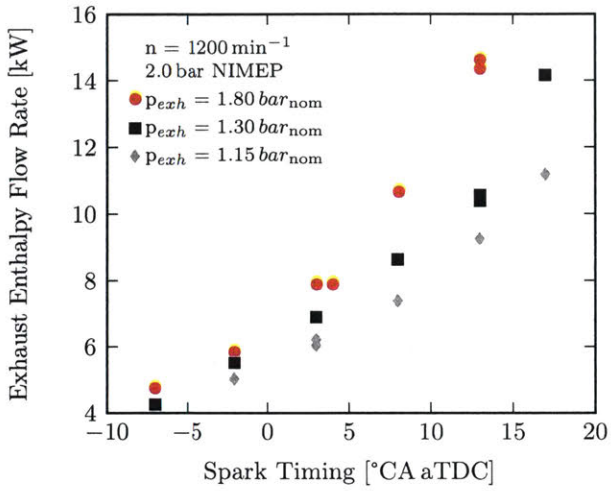

Figure 2-2: Sensible exhaust gas enthalpy flow rate increases with spark timing delay and nominal back pressure, reproduced from Cedrone and Cheng[14]. Nominal back pressure refers to the exhaust pressure during motoring at wide open throttle.

in implicitly as it influences the density of the exhaust gas. An excellent paper by Shaw et al.[67] categorizes models commonly found in literature by the amount of sub-models describing physical and chemical effects such as oxygen storage, conversion kinetics and thermal model as well as their respective detail, ranging from zero to three-dimensional.

Shaw et al.[67] found their lumped or zero dimensional model to agree well with experimental data, though no information can be derived on where inside the converter specifically the HC light-off occurs. Sabatini et al.[65] developed a one-dimensional model that agrees well with experimental observations and allows to determine where HC conversion occurs. Furthermore[61] develop a detailed expression for the position and speed with which the boundary of the reaction front advances in axial direction of the converter. Two-dimensional models are more accurate but require longer computation times and more advanced methods such as alternating direction implicit (ADI) method[36].

Many reaction kinetic models in literature focuses on finding rate expressions for the main reactions happening on the catalytic surface of the three-way catalytic converter, since finding a complete formulation for the locally highly unsteady reactions is nearly impossible. In their very detailed light-off model Koltsakis et al.[36] focus on

rate expressions for six reactions, oxidation of CO, H_2, slow HC, and fast HC by either oxygen or water, as well as NO reduction. They note, however, that the parameters in the kinetic expressions will vary from converter to converter and will have to be determined individually. Matthess et al.[46] found an empirical approach to determine the parameters in rate expressions by using light-off curves derived from flow bench tests with binary mixtures for seven dominant CO and HC oxidation reactions. Rate expressions for oxygen uptake and release by the storage material have been found quite accurate when modeled to be proportional to relative oxygen content above or below stoichiometric[11].

Less common models are post-oxidation sub-models and for close coupled converters pulsating flow inside the converter caused by the intermittent operation on the engine in vicinity of the converter inlet. Heller and Wachtmeister[26] developed a post-oxidation model that simulates heat release from thermal oxidation in the exhaust port with secondary air to improve exhaust system configurations. Yoshizawa et al.[74] note the influence of pulsating flow on the radial temperature distribution of the converter and propose and improved multidimensional thermal model for close coupled converters.

2.3 Research Goals

This research aims to quantify the influence of back pressure on three-way catalytic converter converter light-off by

- investigating the influence of back pressure on the catalytic conversions kinetics in flow bench experiments,
- and the influence of back pressure on the engine and exhaust system with three-way catalytic converter during fast-idle operation after cold-start.

Subsequently a model will be developed to accurately describe the converter light-off with back pressure under transient conditions following engine cold-start.

Chapter 3

Experimental Setup Catalyst Light-Off with Back Pressure

The light-off behavior of a three-way catalytic converter with back pressure was investigated with the experimental apparatus described in this chapter. In a first set of experiments, the converter's behavior to back pressure was investigated at a custom build flow bench independent of engine operating condition. In a second step, the light-off behavior during engine cold-start was investigated at the engine test bench. The same catalytic converter was used for both experiments.

As an indicator for converter light-off propane as a surrogate for unburned hydrocarbons was chosen based on three reasons. First, the emission regulations for hydrocarbons are the strictest. Second, the hydrocarbons require a higher temperature level for conversion inside the catalytic converter than carbon monoxide, compare Heywood[27]. Lastly, the nitrogen oxides emissions are of lesser concern during engine cold-start and converter light-off, due to the relatively low engine peak pressures and temperatures at fast-idle.

3.1 Catalytic Converter

An aluminum oxide converter with a platinum catalyst was used for all experiments, on the flow bench and with the research engine. The converter used is a state of

the art three-way catalytic converter that is commercially available with production engines from General Motors Company (GM), which are similar to the LNF research engine used in this study. The two-liter, two-brick converter has a cell density of 750 cells per square inch (CPI). It has been equipped with several sensors; an Omega® PX302-series absolute pressure sensor was installed just upstream of the first brick to measure the exhaust back pressure. Furthermore, four k-type thermocouples have been installed along the centerline to measure the temperature profile throughout the converter during light-off. The first thermocouple (T1) measures the converter inlet temperature just upstream of the first brick. Three more thermocouples (T2,T3, and T4) measure the temperature of each brick and halfway in between the two bricks respectively, compare Figure 3-1 for the location of the aforementioned sensors. The k-type thermocouple response time is approximately 0.2 s and the temperature range −200 °C to 1250 °C. The pressure transducer's response time is approximately 1 ms and the pressure range is 0 psi to 50 psi or 0 bar to 3.45 bar.

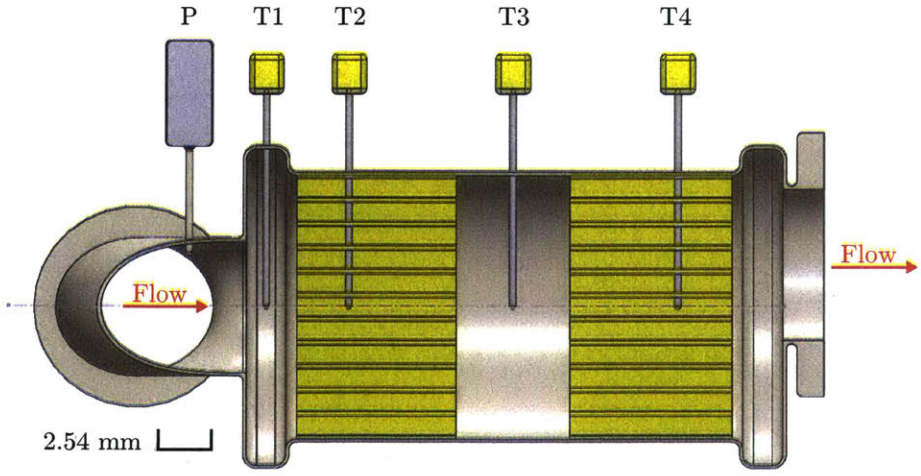

Figure 3-1: Schematic drawing of the three-way catalytic converter used in the flow bench and engine experiments. Drawing to scale except for the channel size for illustrative purposes. The actual channel height is significantly smaller, in the order of 0.9 mm at a cell density of 750 cells per square inch. The k-type thermocouples are labeled T1-T4 and the pressure sensor is labeled P

3.2 Flow Bench

A flow bench for the life-sized TWC was designed and build, to investigate the converter's reaction kinetics in a controlled environment independent of engine operation parameters. The schematic of the flow bench including the converter is shown in Figure 3-2. The reactants, propane (C_3H_8) and oxygen from air, can either be bypassed to the exhaust trench or passed through the catalytic converter, after passing the in-pipe mixing chamber and heater. The propane serves as a surrogate for unburned HCs. The feed gas is balanced by nitrogen, a surrogate for the non-reactive components of the burned gas. Water vapor has not been added to the feed gas for practical reasons, though it would have likely influenced the conversion efficiency of the converter to some degree.

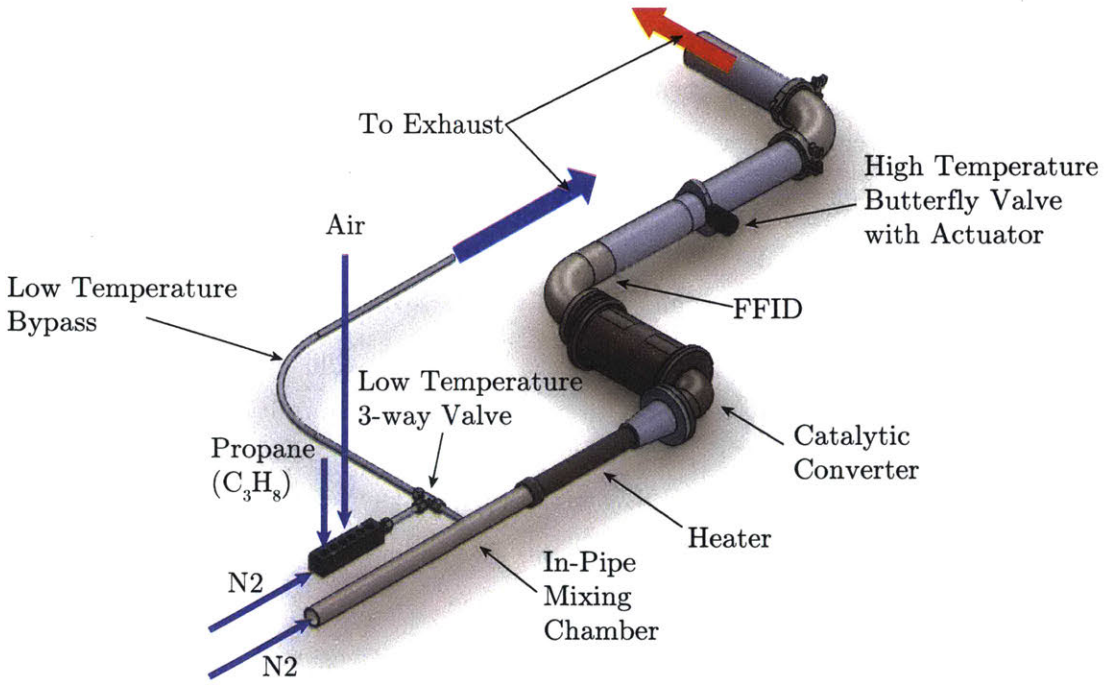

Figure 3-2: Setup of the flow bench for actual sized TWC including feed gas flow path. The main nitrogen feed gas is supplied by a liquid N_2 reservoir and pre-heated before entering the flow meter (not shown in the drawing).

All gases are metered in with mass flow controllers with an accuracy of 2 % from the setpoint. Due to the large flow rate of nitrogen feed gas, it is supplied from a liquid reservoir and requires to be pre-heated to room temperature before enter-

ing the mass flow controller. Mass flow controllers and pre-heater are not shown in Figure 3-2. A fast flame ionization detector (FFID) is used to measure the hydrocarbon concentration downstream from the converter. Together with the upstream HC concentration known from the mass flow meters, it can be used to determine the converter's conversion efficiency for hydrocarbons, defined by

$$\eta_{HC-Conversion} = \frac{\tilde{x}_{HC_{downstream}}}{\tilde{x}_{HC_{upstream}}} \tag{3.1}$$

where $\eta_{HC-Conversion}$ is the converter's HC conversion efficiency, and $x\tilde{_{HC}}$ is the molar HC concentration. It is paramount that the hydrocarbon molecules are uniformly distributed in the feed gas. For that purpose an in-pipe mixer was designed with two main design elements. Firstly, the reactants enter the main nitrogen flow through a small delivery pipe. This pipe crosses the center of the main pipe perpendicularly, dividing the nitrogen flow to pass above and below it. The reactants pass into the main stream in a counterflow arrangement, through a total of ten holes in the delivery pipe, compare Figure 3-3. The ten holes are arranged in three rows, four center holes, positioned in direct counter-flow, and three each slightly upwards and slightly downwards in a sixty degree angle. Secondly, a stacked assembly of perforated plates creates some initial turbulence upstream of the delivery pipe that is intensified in a twelve-stage mixer downstream of it to create mixture uniformity.

3.3 Engine

The General Motors Ecotec Generation II, LNF engine was used for all engine light-off experiments. This commercially available engine is sold as the production engine in various General Motors Company (GM) cars with model year 2007 to 2012.

The direct injected, four-cylinder in-line engine has a swept volume of 1.998 L and a compressions ratio of 9.2:1. The rated peak output is 190 kW at an engine speed of 5300 min^{-1} and the peak torque is 353 N m at an engine speed of 2000 min^{-1}. The research engine is equipped with a twin-scroll turbocharger, as it is in its stock

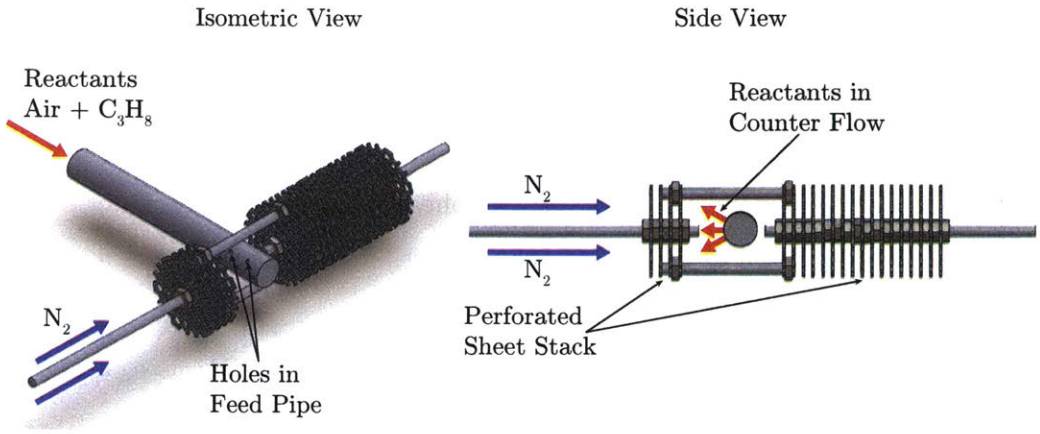

Figure 3-3: Schematic drawing of the flow bench's in-pipe mixing chamber. The reactants air, and propane are passed into the main nitrogen flow in counterflow through a small feed pipe with holes. The perforated sheet stacks up- and downstream of the feed pipe create turbulence for further mixing.

configuration. Furthermore it features a dual camshaft positioned in the cylinder head with continuously variable valve timing (VVT), and sodium-filled stainless steel Inconel exhaust valves. An aluminum piston, as well as steel forged crankshaft and connecting rods, compare Table 3.1 for engine configuration and further geometric details.

Table 3.1: Engine specifications and performance parameters of the GM second generation, Ecotec LNF engine.

Engine Specification	Value and Unit
Engine Displacement	1998 cm^3
Type	I-4 (In-line, 4-Cylinder)
Bore / Stroke	86 / 86 mm
Connecting Rod	145.5 mm
Compression Ratio	9.2:1
Peak Power	190 kW @ 5300 min^{-1}
Peak Torque	353 N m @ 2000 min^{-1}
Fuel Delivery	direct-injection
Electromagnetic Injector, Side Mounted	6-hole
Injector Inclination	25°
Spray Cone Angle	52°
Valve Timing	dual cam phasers, VVT
Turbocharger	twin-scroll

All converter light-off experiments were conducted at the same engine operating point, aside from back pressure variations. The operating point also known as fast-idle

operating condition is representative to operation immediately after cold-start. When a typical engine in an automobile during certification is idling except for running the auxiliary systems mechanically linked to the engine, such as the water pump and generator. As a representative load for these auxiliary systems a net indicated mean effective pressure of 2.0 bar was chosen with a corresponding engine speed of $1200\,\mathrm{min}^{-1}$, compare Table 3.2.

Table 3.2: Engine operating parameters for fast-idle operating condition during engine bench tests for converter light-off.

Fast-Idle Operating Condition	Value and Unit
Intake valve opening (IVO)	10 °CA aTDC
Intake valve closing (IVC)	60 °CA aBDC
Exhaust valve opening (EVO)	50 °CA bBDC
Exhaust valve closing (EVC)	−10 °CA aTDC
Engine Speed	$1200\,\mathrm{min}^{-1}$
Net indicated mean effective pressure	2 bar
Spark Timing	10 °CA aTDC
Lambda	1 –
Injection Pressure	50 bar
Coolant Temperature	20 °C

Even though the engine is equipped with dual camphasers, the valve timing remains that of the parked position at all times during the light-off experiments. Since the goal of this study is to investigate the influence of back pressure on the catalyst light-off behavior and not to find an optimized engine operation or valve timing strategy for converter light-off. To ensure cold-start conditions and for repeatability the engine coolant is conditioned to 20 °C, which is maintained throughout the entire experiment by an external chiller. The spark timing is fixed to 10 °CA aTDC, and the engine is operated stoichiometrically.

3.4 Test Bench

The LNF research engine is operated on a test bench. The engine's drive-shaft is permanently connected to an electric motor, which can be used to motor or crank the engine. In between the motor and engine a dynamometer is attached on the same shaft to absorb the energy produced by the engine, compare Figure 3-4. The dynamometer

can be controlled in either torque or speed mode. In the former setting it exerts a constant load on the shaft equal to the setpoint, in the later it exerts a torque between zero and it maximum torque in order to keep the shaft rotation at the setpoint speed using a proportional-integral-derivative (PID) controller. The dynamometer was operated in speed mode during all engine converter light-off experiments.

The fuel is supplied by a piston cylinder, that is pressurized by high pressure bottled nitrogen. A two-stage regulator reduces the bottle pressure to the piston driving pressure, which is hence independent of the fuel level in the cylinder resulting in a constant pressure level and an injection pressure set to 50 bar. Before reaching the injector, the gasoline is conditioned to 17.9 °C. The engine coolant is conditioned to 20 °C by a chiller that rejects heat to an external cooling circuit, not shown in Figure 3-4. The engine is furthermore equipped with a two-stage intercooler between the compressor exit of the turbo-charger and the intake throttle. In a first step the air is thoroughly cooled by a heat exchanger rejecting heat to the city water, which temperature varies by season. In a second step the intake air is reheated to the desired temperature by an electrical heater.

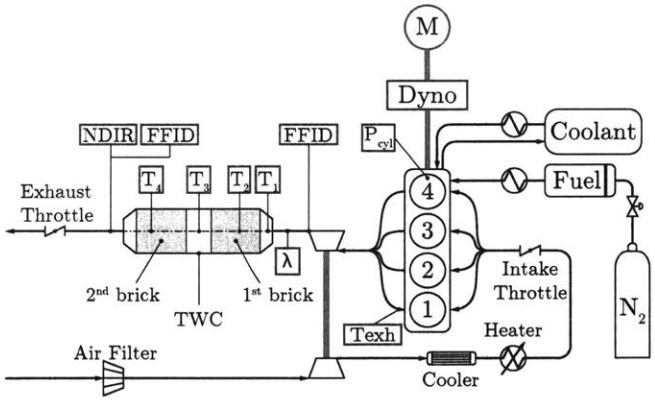

Figure 3-4: Test bench setup with the GM LNF research engine, peripherals and relevant sensors. The engine control system is not shown.

Controls and Sensors

The engine is controlled by a custom built computer code. The code requires the bottom dead center signal, the crank angle signal as well as the absolute cam position signal from the cam sensors. The engine control code allows to control the following parameters independent of engine operating condition; injector opening time with a resolution of 1 µs, as well as spark and valve timing both with a resolution of 1 °CA. The throttle can be actuated independently of the other engine controls, while the absolute position is not monitored the manifold air pressure serves as an indicator.

Absolute pressure sensors from Omega® measure the MAP and exhaust gas back pressure respectively. Additionally cylinder number four is outfitted with an in-cylinder pressure sensor, a cylinder in this setup is commonly called an indicated cylinder (compare Figure 3-4). The pressure sensor used is the Kistler 6125A, a piezoelectric transducer for high-temperature applications. The Kistler 5010B charge amplifier converts the charge signal from the piezoelectric transducer into an analog voltage proportional to the pressure sensed.

Exhaust System

Various thermocouples have been installed in the engine's exhaust system and catalytic converter to measure the temperature transients during the light-off experiments. All thermocouples used were k-type from Omega®. The engine out temperature of the exhaust gas is measured in the runner of cylinder number one, 10 cm downstream of the exhaust valve, compare Figure 3-4. Four more thermocouples are located inside the catalytic converter, compare Figure 3-1 for their locations. An oxygen sensor measures the air-fuel ratio just upstream of the catalytic converter. The sensor used is a Bosch LSU type sensor connected to an ETAS UEGO controller. The ETAS controller outputs an analog voltage that is proportional to the air-fuel equivalence ratio. A Cambustion fast flame ionization detector (FFID) was used to measure the hydrocarbon concentration in the exhaust gas up- and down-stream from the converter. Furthermore a Cambustion nondispersive infrared detector (NDIR) was used

to measure the CO and CO_2 concentration in the exhaust gas downstream from the converter. The Cambustion fast flame ionization detector and nondispersive infrared detector exhaust gas sampling systems both have millisecond response time, allowing to monitor the carbon monoxide and carbon dioxide in real time during light-off.

3.5 Data Acquisition and Processing

A LabVIEW code was developed to acquire the signals from the sensors mentioned above. The National Instruments cDAQ-9172 data acquisition (DAQ) chassis was used to physically acquire the sensor signals using various analogue input modules of type NI-9215 and NI-9211 type thermocouples modules. All signals except the manifold air pressure and in-cylinder pressure were sampled with the same data acquisition system using the same trigger and sample clock at a moderate sample rate of 100 Hz, which is sufficiently high considering the rather slow thermal processes and thermocouple response time. The manifold air pressure and in-cylinder pressure measurement were sampled hadware timed at a much higher rate of 1 °CA which at an engine speed of $1200\,\mathrm{min}^{-1}$ corresponds to a sampling rate of 7200 Hz. It is advantageous to sample the in-cylinder pressure in the crank angle domain, since the calculation of engine operating condition related parameters, such as net indicated mean effective pressure compare Section ??, requires the knowledge of the cylinder volume and hence the piston position, which can be calculated for a given crank angle position.

The Kistler piezoelectric pressure transducer used for in-cylinder pressure sampling (compare Section 3.4) experiences long-term drift in its setup with the charge amplifier due to its working principle. To correct this drift, the in-cylinder pressure measurement is pegged to the manifold air pressure when the piston is close to bottom dead center. At that time the MAP and in-cylinder pressure are assumed to be the same, due to the relatively low piston speed and reasonably wide opened intake valve dynamic pressure effects are negligible and there is almost pressure equilibrium. See section Pegging on page 88 for a detailed explanation of the pegging process adopted.

The net indicated mean effective pressure is calculated with the Rassweiler-Withrow method using crank angle sampled in-cyinder pressure data[64].

Chapter 4

Catalyst Light-Off with Back Pressure

This chapter quantifies how back pressure influences the hydrocarbon conversion kinetics of the three-way catalytic converter determined by flow bench experiments at quasi steady state and for dynamic pressure changes. Subsequently the same converter is used in engine bench tests to quantify the influence of back pressure on engine operating condition and exhaust gas system for light-off during fast-idle after cold-start.

The results obtained at the flow bench and engine test bench are used to determine a suitable simulation model that can accurately describe the converter light-off behavior with back pressure.

4.1 Flow Bench Experiments

Static Back Pressure

A quasi-steady state experiment was developed for the flow bench to investigate the influence of back pressure on the conversion kinetics of the three-way catalytic converter independently from engine behavior or other dynamic effects. For repeatability of the experiments the converter was pre-conditioned and cleaned before and after

each experiment strictly according to the following procedure, shown in Figure 4-1.

Initially the temperature is ramped up quickly from room temperature of 25 °C to 190 °C where it is maintained for 6 min for the converter and flow bench piping to reach thermal equilibrium. During this initial phase the feed gas consist only of inert nitrogen and the pressure in the apparatus is equal to the ambient pressure. Furthermore the fast flame ionization detector is calibrated during this period minimizing drift due to sudden temperature rise. From minute six of the experiment onwards the reactants (propane and oxygen from air) are added to the feed gas and passed through the converter, and the back pressure is adjusted to the target value. The actual experiment starts at a clock time of 7 min. The temperature is ramped up at a linear gradient of 5 °C min^{-1}, which is a common value found in literature ensuring quasi thermal equilibrium or quasi-steady state[46].

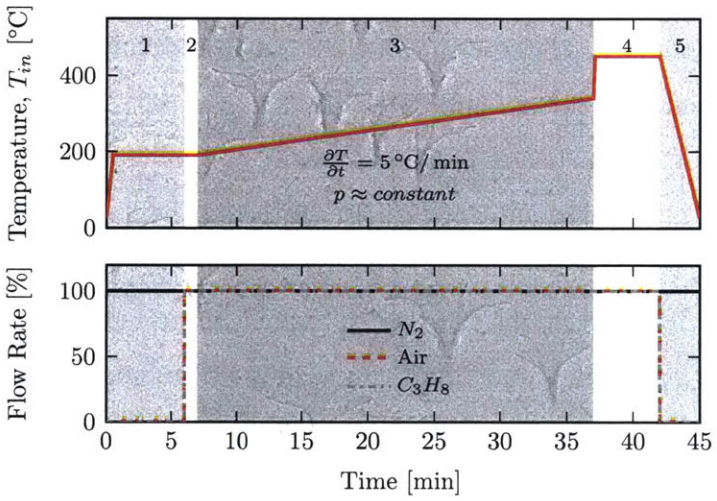

Figure 4-1: The five stages of the quasi-steady state experiment; (1) warm-up phase, (2) pressure adjustment, (3) quasi-steady state experiment, (4) high temperature cleaning, and (5) cool-down in inert atmosphere. The converter inlet temperature evolution is shown in the top graph and the relative mass flow rates through each flow controller is shown below.

The converter reaches full light-off before 340 °C, which is the final temperature of the experiment. Subsequently the converter is cleaned and conditioned for the next experiment. Nitrogen and the reactants are flown through the converter at an inlet temperature of 450 °C, as a result any reactants on the catalytic surface are converted and leaving the catalytic surface of the converter, this process stabilizes the catalytic

surface. Sometimes longer stabilization times and different temperatures are found in literature[46], but sensitivity tests with the flow bench utilized have shown good repeatability for the stabilization time used. Lastly the converter is cooled down with only nitrogen as feed gas in a pure nitrogen atmosphere, from 450 °C to 25 °C.

A range of operating conditions was investigated at different absolute back pressures ranging from 1.03 bar to 2.07 bar, and total mass flow rates of feed gas from 30 kg h^{-1} to 40 kg h^{-1}. The molar propane concentration was kept constant at a nominal value of 450 *ppm* C_3, to minimize the heat release from hydrocarbons and thus the temperature gradient in axial direction. The air and nitrogen flow rates can be calculated for a given propane concentration for stoichiometric gas compositions, which denotes a ratio of O_2 to C_3H_8 that allows to fully oxidize all carbon and hydrogen atoms. Any multiple of that O_2 concentration for the same amount of C_3H_8 is defined as λ. The ratio of O_2 toC_3H_8 in the feed gas for stoichiometric or lean mixture is governed by

$$C_3H_8 + 5\,\lambda\,(O_2 + 3.76\,N_2) \longrightarrow 3\,CO_2 + 4\,H_2O + 18.81\,\lambda\,N_2 + (\lambda - 1)\,O_2 \quad (4.1)$$

which assumes a molar concentration of 21 % for O_2 and 79 % for N_2. And hence the ratio of the O_2 and C_3H_8 flow rate is given by

$$\frac{\dot{n}_{O_2}}{\dot{n}_{C_3H_8}} = 5 \cdot \lambda \quad (4.2)$$

Using this equation, the flow rates of all the feed gases can be calculated by target C_3H_8 concentration ($\tilde{x}_{C_3H_8,target}$) and mass conservation for the feed gas mass flow rate ($\dot{m}$).

$$\tilde{x}_{C_3H_8,target} = \frac{\dot{n}_{C_3H_8}}{\dot{n}_{O_2} + \dot{n}_{C_3H_8} + \dot{n}_{N_2}} = \frac{\dot{n}_{C_3H_8}}{\sum_i \dot{n}_i} = 450\,ppm \quad (4.3)$$

$$\dot{m} = \sum_i \dot{n}_i \cdot M_i \quad (4.4)$$

Where M_i is the molar mass of species i, and $\dot{n}_i$ the molar flow rate the respective

species. Furthermore the converter's operating condition is commonly characterized by the space velocity (SV), which is defined by

$$SV(\dot{m}, p, T) = \frac{\dot{V}}{V_{cat}} = \frac{\dot{m}/\rho}{V_{cat}} = \frac{\dot{m}}{V_{cat}} \cdot \frac{1}{\rho(T,p)} \tag{4.5}$$

where $\dot{m}$ is the mass flow rate, p the pressure, T the temperature, $\dot{V}$ the volumetric flow rate, ρ the density of the feed gas, and V_{cat} the volume of the three-way catalytic converter. Using the ideal gas law to express the density ρ, Equation 4.5 can be rearranged to,

$$SV = \frac{\dot{m}}{V_{cat}} \cdot \frac{R \cdot T}{p} = \frac{\dot{m} \cdot R}{V_{cat} \cdot p} \cdot T \tag{4.6}$$

where R is the ideal gas constant. For any given quasi-steady state experiment the feed gas mass flow rate and pressure is constant, while the temperature increases steadily. And hence a constant reference space velocity (SV_0) can be calculated by introducing the reference temperature (T_0) , that is characteristic for a given experiment and differs from the actual space velocity only by the instantaneous temperature of the converter.

$$SV = \frac{\dot{m}_{exp}}{p_{exp}} \cdot \frac{R \cdot T_0}{V_{cat}} \cdot \frac{T}{T_0} = SV_0 \cdot \frac{T}{T_0} \qquad [\mathrm{h}^{-1}] \tag{4.7}$$

The reference temperature T_0 is chosen to be 273.15 K, and SV_0 depends on quantities that are constant for a given converter and quasi-steady state experiment. The range of operating conditions investigated is summarized in Table 4.1.

At quasi-steady state hydrocarbon conversion efficiency of the converter seems to be independent of the mass flow rate and back pressure, but is only a function of the converter inlet temperature. Figure 4-2 shows the conversion efficiency for mass flow rates from 30 $\mathrm{kg\,h^{-1}}$ to 40 $\mathrm{kg\,h^{-1}}$ and low back pressures of approximately 1 bar as well as high back pressures of approximately 2 bar absolute. All conversion efficiency curves for the operating conditions mentioned line up on top of each other. The first hydrocarbon molecules start to get converted at a temperature just below 200 °C and full converter light-off is reached at a temperature around 300 °C, when more than

Table 4.1: Range of operating conditions for quasi-steady state experiment. The propane and oxygen concentration in the feed gas is kept constant for all operating conditions to limit heat release from hydrocarbon conversion.

Property	Range
Total Mass Flow, $\dot{m}$	$30\,\mathrm{kg\,h^{-1}}$ to $40\,\mathrm{kg\,h^{-1}}$
Pressure, p	1.03 bar to 2.07 bar
Temperature, T	190 °C to 340 °C
Reference Space Velocity, SV_0	$5702\,\mathrm{h^{-1}}$ to $15{,}030\,\mathrm{h^{-1}}$
Space Velocity, SV	$9668\,\mathrm{h^{-1}}$ to $33{,}738\,\mathrm{h^{-1}}$
C_3H_8 concentration	$450\,ppm\,C_3$
O_2 concentration	$2250\,ppm$
N_2 concentration	Balance
λ	1

99 % of the HC molecules in the feed gas are converted.

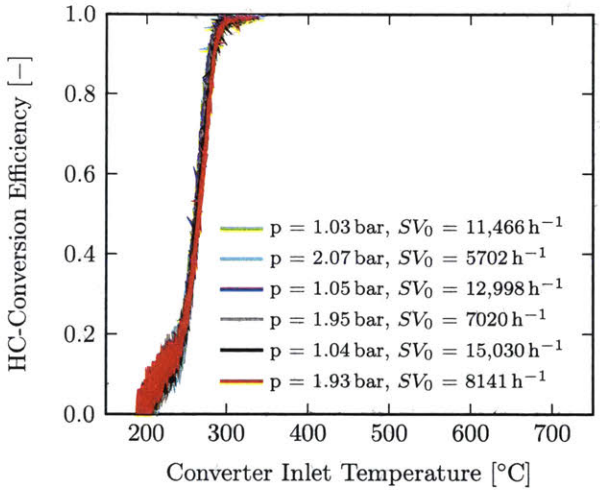

Figure 4-2: Hydrocarbon conversion efficiency at quasi-steady state does not depend on mass flow rate or back pressure for a wide range of operating conditions, for a mass flow rate from $30\,\mathrm{kg\,h^{-1}}$ to $40\,\mathrm{kg\,h^{-1}}$ and exhaust pressure from 1.03 bar to 2.07 bar. The feed gas composition is stoichiometric ($\lambda = 1$) for all operating conditions.

So far the feed gas composition was kept constant and stoichiometric, i.e. the molar fraction of the reactants O_2 and C_3H_8 was kept constant only the total flow rate was varied. The influence of the feed gas composition on the converter's light-off behavior was investigated in lambda sweeps. While the hydrocarbon concentration was kept constant at $450\,ppm\,C_3$ to limit heat release from C_3H_8 conversion, the O_2 content in the feed gas was increased up to twice its amount of the stoichiometric case ($\lambda = 2$). The overall mass flow rate of the feed gas was kept constant by adjusting

the nitrogen flow rate according to Equation 4.2 - 4.4.

Changing the feed gas composition from stoichiometric to lean had no influence on the hydrocarbon conversion efficiency of the converter for the range of conditions investigated, compare Figure 4-3. At quasi-steady state, the hydrocarbon conversion efficiency of the converter is only a function of temperature and not depending on mass flow rate, back pressure, or composition for stoichiometric or lean for the operating conditions investigated. Rich conditions were not investigated, since full conversion cannot be reached under rich conditions.

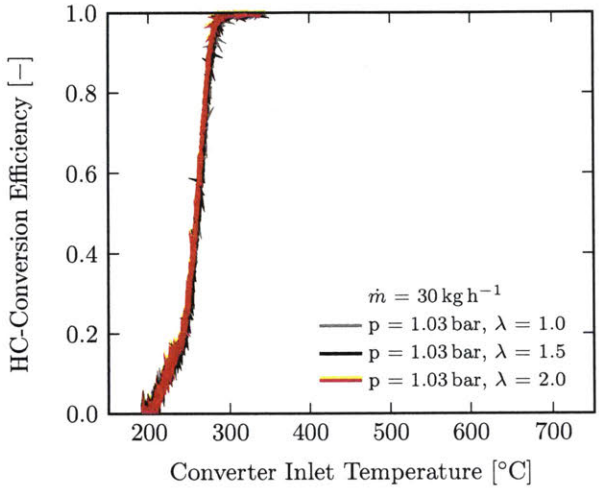

Figure 4-3: Oxygen to propane ratio does not influence the converter's conversion efficiency for hydrocarbons as long as the feed gas composition is stoichiometric or lean at quasi-steady state. A rich feed gas composition was not investigated, since complete oxidation is not possible.

Dynamic Pressure Changes

The quasi-steady state experiment gives valuable insight into the kinetics happening on the catalytic surface of the converter at a given temperature and pressure. The influence of dynamic back pressure changes on the C_3H_8 conversion efficiency was investigated with a pressure step change experiment.

The cleaning and cool down process of the step change experiment is the same as in the quasi-steady state experiment. However, the warm-up phase and the actual experiment is different. The temperature is kept constant throughout warm-up phase

and the entire experiment. During the warm-up phase and the first five minutes of the experiment, the pressure is ambient. After that the pressure is stepped up and down twice for five minutes each time, compare Figure 4-4. The first pressure step serves as reference for repeatability, while the second step change from high to low is evaluated. The butterfly throttle valve can be fully opened almost instantly, so that pressure falls to ambient, whereas the throttle position to step up the pressure is not clearly defined and it may take a few seconds to reach the respective position and target pressure. Subsequently the converter is cleaned and cooled down according to the same procedure as in the quasi-steady state experiment.

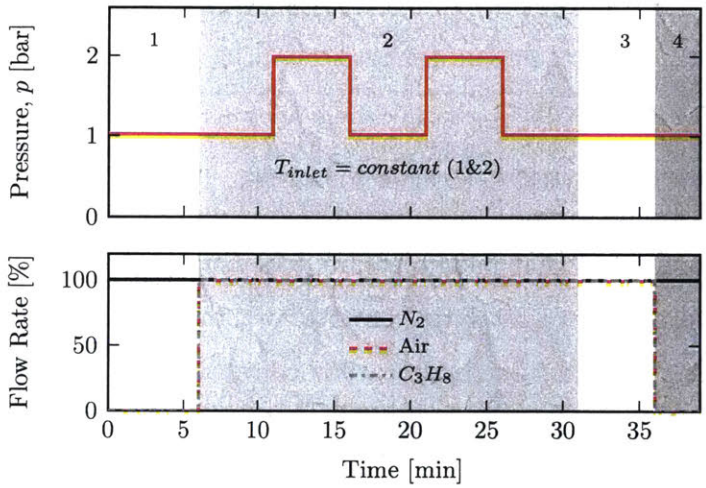

Figure 4-4: Pressure step change experiment; (1) warm-up phase, (2) step change experiment, (3) cleaning phase, and (4) cool-down or relaxation phase. The pressure is stepped up and down twice during the experiment, while the temperature is constant throughout warm-up and experiment. No reactants are present in the feed gas during the warm-up phase. Finally the converter is cleaned and cooled-down to relax the catalytic surface.

Dynamic pressure changes are not affecting the converter's hydrocarbon conversion efficiency for the operating conditions investigated. The hydrocarbon concentration in the gas exiting the converter and measured by the fast flame ionization detector downstream of the three-way catalytic converter is constant and the same before and after the pressure step change, compare Figure 4-5. The total concentration differs with the temperature, due to the respective light-off stage of the converter a different fraction of the hydrocarbon in the feed gas are converted. This behavior was observed for different mass flow rates from $30\,\mathrm{kg\,h^{-1}}$ to $40\,\mathrm{kg\,h^{-1}}$.

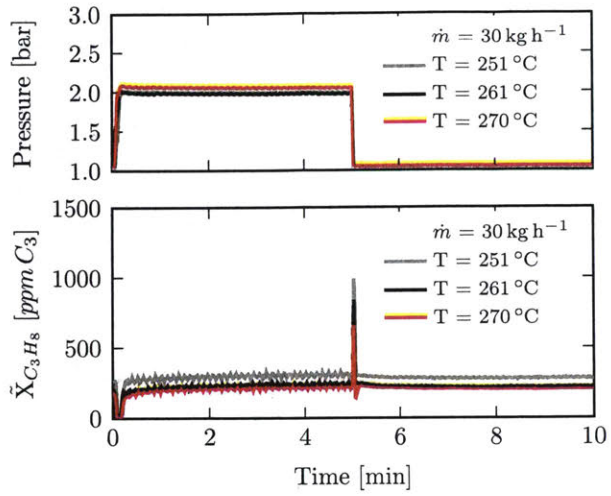

Figure 4-5: A step change in pressure does not influence the conversion efficiency of the converter at constant temperature, since the propane concentration in the gas downstream of the converter does not change with pressure. The spike in concentration during the pressure change is due to the pressure response of the analyzer. The step change in pressure is shown in the above graph, and the temperature is constant throughout the entire experiment.

It can be concluded that back pressure does not seem to influence the light-off behavior of the three-way catalytic converter whether the back pressure change is dynamic or static, but that the hydrocarbon conversion efficiency of the converter is only a function of temperature for the operating conditions investigated.

4.2 Engine Experiments

A change in back pressure alters the engine operation during fast-idle after cold start independently of the converter. Subsequently the converter's light-off behavior is changed due to shift in engine operation and possibly the back pressure influence on the exhaust system.

The pumping work of the engine increases with rising back pressure, an effect widely described and investigated in literature[9,17,68]. As the back pressure increases, the negative work of the pumping loop increases for throttled operation. To compensate for that effect and maintain the same net indicated mean effective pressure that is imposed by the fast-idle condition to run the engine's auxiliary systems, the engine needs to be de-throttled. As a result the manifold air pressure increases reducing

the difference in pressure to the exhaust stroke, partly compensating the increased pumping work. Furthermore the air flow into the engine increases and with it the amount of fuel injected due to stoichiometric operation increasing the positive work output from the high pressure loop, compare Figure 4-6.

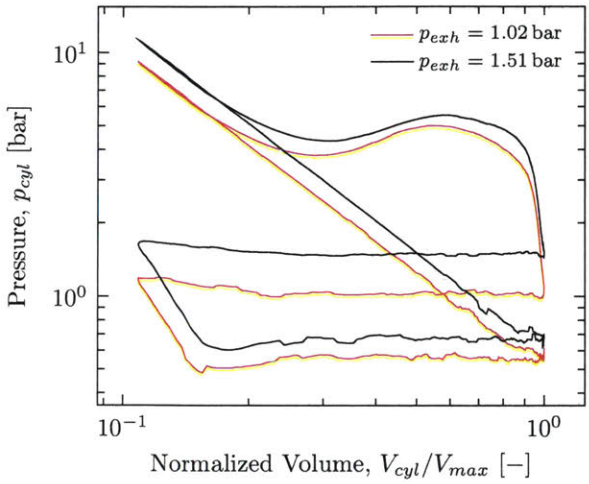

Figure 4-6: The negative work of the pumping loop increases with back pressure. To maintain the fast-idle condition, the engine needs to be de-throttled. Reducing the work of the pumping loop and increasing the in-cylinder charge, which also increases the positive work of the high-pressure loop.

The change in engine operating conditions has two effects on the converter's light-off behavior. First the exhaust gas mass flow increases due to de-throttling, second the blowdown process changes. When the exhaust valve opens and the hot gas expands into the exhaust system (blowdown), it expands less due to the higher exhaust gas back pressure yielding in an elevated exhaust gas temperature compared to lower exhaust back pressure.

The exhaust gas mass flow increases linearly with back pressure, as shown by engine simulations in GT-Power that agree well with engine bench tests, compare Figure 4-7. The exhaust gas mass flow for the fast idle condition without back pressure at an absolute exhaust pressure of 1.02 bar was measured to be 34.7 $\mathrm{kg\,h^{-1}}$ and increases by 31.1 % to 45.5 $\mathrm{kg\,h^{-1}}$ for a back pressure of 2.0 bar.

The influence of back pressure on the cycle-resolved temperature of the blowdown process across the exhaust valve is difficult to measure due to the short timescale of the blowdown process and the relatively long response time of the thermocouple. A

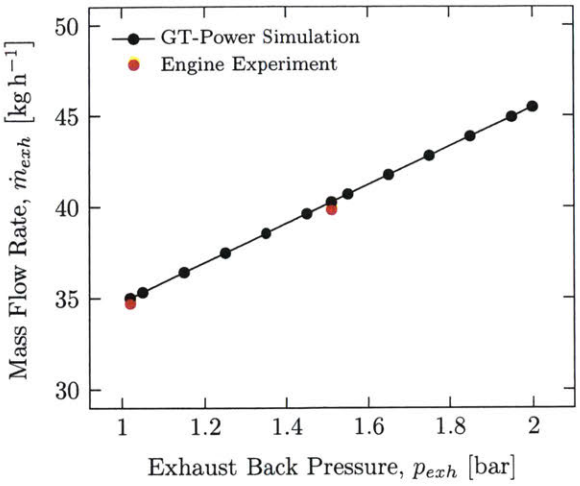

Figure 4-7: Exhaust gas mass flow increases linearly with back pressure for constant engine speed and load. The experimental data from the engine test matches the GT-Power simulation with an accuracy of one percent.

GT-Power simulation shows how the in-cylinder temperature of the burned mixture is effected when exhausting into an increased back pressure environment, compare Figure 4-8. When there first is a noticeable flow past the exhaust valve, the in cylinder temperature without back pressure drops to 1268 °C. At the same crank angle of 171 °CA aTDC the temperature with 2.0 bar back pressure is 12 % higher at 1419 °C.

At the engine test bench, the exhaust gas temperature due to blowdown is measured in the exhaust runner approximately 10 cm downstream from the exhaust valve. This location and thermocouple will henceforth be noted as *Temperature Exhaust Runner*. While it cannot resolve the temperature fluctuations from cycle-to-cycle, it measures an averaged temperature with a resolution of its response time of 0.2 s. Figure 4-9 depicts the temperature transient in the exhaust runner during the light-off experiment at the engine test bench. The exhaust gas temperature rises faster with back pressure in the runner and reaches 400 °C in the case of ambient back pressure and 480 °C in the case of 1.51 bar back pressure, both at a clock time of 90 s into the light-off experiment.

Two peculiarities are observed in Figure 4-9, while the blowdown is significantly different with back pressure resulting in an elevated exhaust gas temperature, those

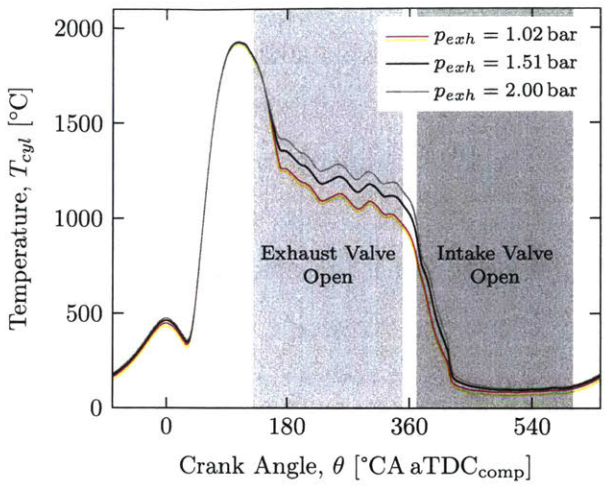

Figure 4-8: In-cylinder gas temperature is higher during the exhaust event in the case with back pressure compared to the baseline case, resulting in elevated exhaust gas enthalpy flow rate. The temperature evolution inside the cylinder prior to the exhaust event during compression and combustion is similar with and without back pressure. The temperatures remain the same in the beginning of the exhaust event, due to the minuscule lift of the exhaust valve.

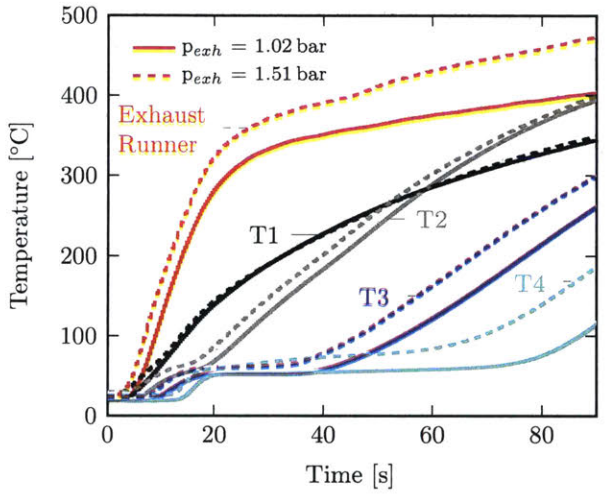

Figure 4-9: Temperature evolution during the fast-idle cold start engine experiment with and without back pressure. The temperature in the exhaust runner is higher with back pressure due to the different blowdown process. The temperature at converter inlet (T1) is the same with and without back pressure. Downstream throughout the converter the temperature rises slightly faster with back pressure because of the higher exhaust gas mass flow rate and hence larger enthalpy flow rate at same inlet temperature.

temperatures equalize at the converter inlet. Second, there is an initial sudden rise of the temperature throughout the entire converter, which subsequently plateaus at a constant value throughout the converter before it starts rising again. As it turns out this effect can be attributed to condensation of water vapor inside the converter.

However, first we want to find an explanation as to why the exhaust gas with back pressure at a larger mass flow rate and higher temperature in the exhaust runner enters the converter at the same temperature as without back pressure.

The difference in temperature drop from exhaust runner to converter inlet cannot be explained by the difference in heat transfer due to the different exhaust gas mass flow in the low back pressure case versus the high back pressure case (cf. Figure 4-9). The temperature drop due to heat transfer is governed by,

$$\Delta T = \int \frac{k \cdot (T - T_w) \cdot Nu \cdot F}{\dot{m} \cdot c_{pg} \cdot b} \, dx \tag{4.8}$$

where ΔT is the temperature drop along the flow path, k the thermal conductivity, T_w the wall temperature of the exhaust pipe, Nu the Nusselt number, F the perimeter of exhaust system cross section, $\dot{m}$ the exhaust gas mass flow, c_{pg} the exhaust gas heat capacity, and b the hydraulic diameter of exhaust system. The integration is along the flow path. For this flow at high Reynolds number, the Nusselt number is proportional to $\dot{m}^{0.8}$. The scaling with respect to the change of back pressure and hence mass flow is governed by,

$$\frac{\Delta T_2}{\Delta T_1} = \left(\frac{\dot{m}_1}{\dot{m}_2}\right)^{0.2} \cdot \frac{(\overline{T - T_w})_2}{(\overline{T - T_w})_1} \tag{4.9}$$

where the overbar denotes the average quantities along the flow path. Taking representative values at the 40 s point in Figure 4-9, $\Delta T_2/\Delta T_1$ due to heat transfer is 1.05. The observed value is 1.42, and hence the difference in temperature drop cannot be explained due to heat transfer.

A steady state engine test was performed to ensure the larger drop in temperature from exhaust runner to converter inlet with back pressure was not due to the transient conditions at cold-start. For low back pressure, the temperature in the exhaust runner is higher than at converter inlet by approximately 40 °C for a spark timing of −15 °CA aTDC, compare Figure 4-10. As the spark timing is delayed, the converter inlet temperature approaches the exhaust runner temperature until they become the same at a spark timing of approximately 6 °CA aTDC. For later spark timings the

converter inlet temperature is higher than the exhaust runner temperature, which indicates post-oxidation.. For the temperature of the exhaust gas to rise while flowing through a cooler pipe there needs to be some sort of heat generation. The same general behavior is observed in the high back pressure case, however the converter inlet temperature barely surpasses the exhaust runner temperature in that case. It is worthy to note though that for a spark timing of 10 °CA aTDC the converter inlet temperature with and without back pressure are practically the same which was also observed in the transient light-off experiment, compare Figure 4-9.

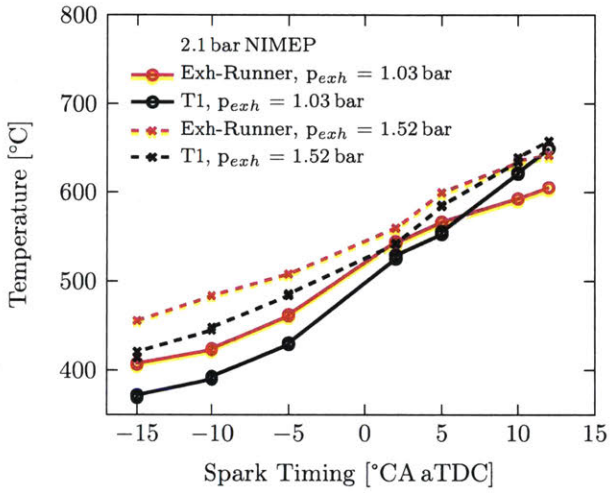

Figure 4-10: Exhaust gas temperature in the runner and converter inlet (T1) at steady state engine operation as a function of spark timing. For early spark timing the temperature in the the exhaust runner is higher than at the converter inlet. However, with spark retard the inlet temperature approaches the runner temperature. In the high back pressure case the converter inlet temperature is the same as the runner temperature for a spark timing of 10 °CA aTDC, while the inlet temperature surpasses the runner temperature in the low back pressure case. An indication for a more significant heat release in the low back pressure case.

The hydrocarbon concentration in the exhaust runner and at converter inlet was measured to quantify the heat release from HC conversion for the cold start light-off experiment. In the low back pressure case the hydrocarbon concentration in the exhaust runner stabilizes at approximately $6000\,ppm\,C_1$, after an initial spike during the engine start up process, compare Figure 4-11. In the high back pressure case the hydrocarbon concentration in the exhaust runner at engine out is significantly lower at approximately $3500\,ppm\,C_1$. In both cases the hydrocarbon concentration decreases along the flow path, due to hydrocarbon conversion. However, the drop from

exhaust runner to converter inlet is significantly larger in the low back pressure case, where it drops by 3000 $ppm\,C_1$ from 6000 $ppm\,C_1$ to 3000 $ppm\,C_1$. In the high back pressure case, the hydrocarbon concentration drops by 2000 $ppm\,C_1$ from 3500 $ppm\,C_1$ to 1500 $ppm\,C_1$. The difference in heat release due to HC conversion is proportional to the product of exhaust gas mass flow and drop in HC concentration between exhaust runner and converter inlet, since the molar mass is approximately constant for the exhaust gas.

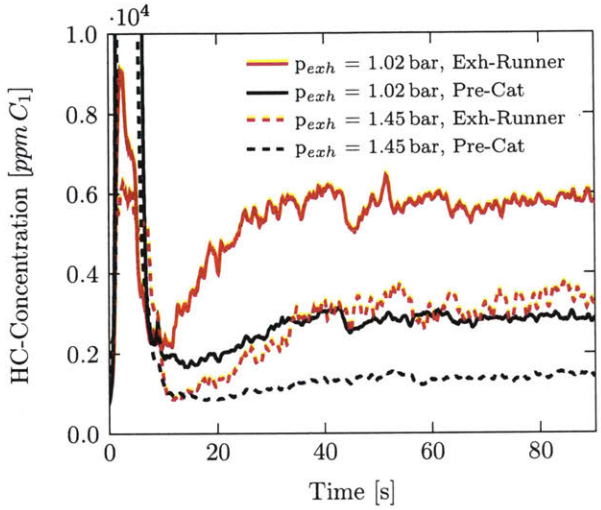

Figure 4-11: hydrocarbon concentration in the exhaust runner and at the converter inlet with an without back pressure. Total HC concentration as well as the drop in concentration from exhaust runner to converter is larger without back pressure, indicating larger heat release from HC post-oxidation compared to high back pressure case.

Condensation Effect

Condensation of water vapor in the exhaust gas causes the converter temperature to rise quickly during cold start. The rise occurs from room temperature to 54.2 °C throughout the entire converter within 10 s from the cold start in the low back pressure case of 1.02 bar, compare Figure 4-12. The temperature throughout the converter remains there for some time before it continues to rise. For the higher back pressure case the same characteristic is observed though the temperature rises slightly more to 61.5 °C for a back pressure of 1.51 bar. It is believed that this is due to the condensation of water vapor inside the converter and the associated release of latent

heat, the constant temperature can be attributed to the two-phase state. Since the partial pressure of water is higher with back pressure, the saturation temperature is slightly elevated compared to the low back pressure case.

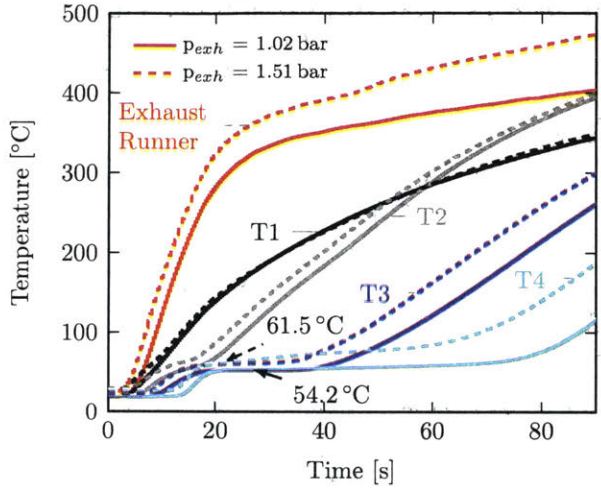

Figure 4-12: Condensation on the catalytic surface shortly after cold start. The converter temperature increases suddenly due to latent heat and plateaus at the saturation temperature, before the overall enthalpy flow causes the temperature to rise beyond the saturation temperature and condensation to cease. The saturation temperature in the low back pressure case is 54.2 °C and in the high back pressure case 61.5 °C, averaged between 20 s and 25 s.

To prove the hypothesis of condensation and the associated temperature rise inside the three-way catalytic converter we will determine the water vapor fraction in the exhaust gas and the corresponding saturation temperature. The two sources for water vapor in the exhaust gas are the water mass in the ambient, humid air used for gasoline combustion, and the other water as a product from burning the hydrocarbon fuel. Using the ideal gas law, the ambient pressure is the sum of partial pressure of water vapor and dry air. In other words, the ambient air's composition is made up of dry air and water vapor or mathematically,

$$p_{amb} = p_{\mathrm{H_2O}} + p_{air,dry} \tag{4.10}$$

$$1 = \frac{p_{\mathrm{H_2O}}}{p_{amb}} + \frac{p_{air,dry}}{p_{amb}} = \tilde{x}_{\mathrm{H_2O}} + \tilde{x}_{air,dry} \tag{4.11}$$

where p_{amb} is the known ambient pressure, $p_{\mathrm{H_2O}}$ the partial pressure of the water vapor, $p_{air,dry}$ the partial pressure of the dry air, and $\tilde{x}_{\mathrm{H_2O}}$ and $\tilde{x}_{air,dry}$ the volume

fractions of water vapor, and dry air respectively.

The water fraction in the ambient air can be calculated with the relative humidity, which determines the partial pressure of the water as a function of the water saturation pressure at the ambient air temperature by,

$$p_{\mathrm{H_2O}} \equiv \phi \cdot p_{\mathrm{H_2O,sat}}(T_{amb}) \tag{4.12}$$

$$\tilde{x}_{\mathrm{H_2O_{air,wet}}} = \frac{p_{\mathrm{H_2O}}}{p_{amb}} = \phi \cdot \frac{p_{\mathrm{H_2O,sat}}(T)}{p_{amb}} \equiv \alpha \tag{4.13}$$

where ϕ is the relative humidity, and $p_{\mathrm{H_2O,sat}}$ the saturation pressure of water at ambient temperature (T_{amb}). The volume fraction of dry air is defined once the water vapor content is known by Equation 4.11. Assuming that dry air is composed of only O_2 and N_2 the composition of wet air is given by,

$$Air_{wet} \equiv \tilde{x}_{\mathrm{H_2O}} \cdot \mathrm{H_2O} + \tilde{x}_{air,dry} \cdot (\tilde{x}_{O2,air} \cdot \mathrm{O_2} + \tilde{x}_{N2,air} \cdot \mathrm{N_2}) \tag{4.14}$$

$$\beta \equiv x_{\mathrm{O_2},air} = 0.21 \tag{4.15}$$

$$\gamma \equiv x_{\mathrm{N_2},air} = 0.79 \tag{4.16}$$

This assumption is a simplification as the air in the Earth's atmosphere contains other elements such as carbon dioxide and inert gases such as argon, neon, and helium. However, the concentration of these elements is minuscule, they are inert and their collective properties are similar to nitrogen for the purpose of this study and will be counted towards the N_2 concentration of the atmosphere. Using Equation 4.11 and Equations 4.13-4.16 the composition of wet air can be described by,

$$Air_{wet} = \alpha \cdot \mathrm{H_2O} + (1-\alpha) \cdot (\beta \cdot \mathrm{O_2} + \gamma \cdot \mathrm{N_2}) \tag{4.17}$$

Or rearranged per oxygen molecule wet air contains water and nitrogen in the following quantities:

$$\text{Composition of wet air with for 1mol } \mathrm{O_2}\text{:} \quad \mathrm{O_2} + \frac{\alpha}{(1-\alpha)\cdot\beta} \cdot \mathrm{H_2O} + \frac{\gamma}{\beta} \cdot \mathrm{N_2} \tag{4.18}$$

For stoichiometric combustion of humid air with a hydrocarbon fuel of composition CH_y the water vapor content in the exhaust gas can be calculated using the following formula for complete combustion,

$$CH_y + \nu \cdot (O_2 + \delta \cdot H_2O + \psi \cdot N_2) \longrightarrow \omega \cdot CO_2 + \zeta \cdot H_2O + \mu \cdot N_2 \tag{4.19}$$

The four unknowns (ν, ξ, ζ, and μ) are fully defined by an element balance for the four elements carbon, hydrogen, oxygen, and nitrogen.

$$\text{C}: \quad 1 = \omega \tag{4.20}$$

$$\text{H}: \quad y + 2 \cdot \nu \cdot \delta = 2 \cdot \zeta \tag{4.21}$$

$$0: \quad 2 \cdot \nu = 2 \cdot \xi + \zeta \tag{4.22}$$

$$\text{N}: \quad \nu \cdot \psi = \mu \tag{4.23}$$

The constants (δ and ψ) depend on the relative humidity of air and are defined by Equation 4.18. Solving the element balance yields,

$$\omega = 1 \tag{4.24}$$

$$\nu = (1 + \frac{y}{4}) \tag{4.25}$$

$$\delta = \frac{\alpha}{\beta \cdot (1 - \alpha)} \tag{4.26}$$

$$\psi = \frac{\gamma}{\beta} \tag{4.27}$$

$$\mu = \psi \cdot \nu \tag{4.28}$$

$$\zeta = \frac{y}{2} + \nu \cdot \delta \tag{4.29}$$

The unknown α can be calculated using the formula for the relative humidity. Table 4.2 depicts the values used to calculate the exhaust gas composition.

The exhaust pressure and ambient temperature in Table 4.2 are measured, while relative humidity and ambient pressure are estimated from measurements by weather stations for the day of the respective experiment. The fuel used is Halterman certifi-

Table 4.2: Constants used to calculate the partial pressure of water vapor in the exhaust gas from hydrocarbon conversion due to combustion and water vapor in the humid air for the engine experiment with and without back pressure. The corresponding saturation temperature from the NIST tables matches the observed temperature of the converter within half a degree celsius. The converter temperature was averaged for 5 s at a clock time from 20 s to 25 s of the experiment.

	w/o Back Pressure	w/ Back Pressure
H/C-ratio fuel, y [−]	1.82	1.82
$\tilde{x}_{O_2,amb}, \beta$ [−]	0.21	0.21
$\tilde{x}_{N_2,amb}, \gamma$ [−]	0.79	0.79
Relative Humidity, ϕ [%]	80	85
$p_{ambient}$ [bar]	1.005	1.005
$T_{ambient}$ [°C]	25.7	23.0
$p_{exhaust}$ [bar]	1.02	1.51
$p_{H_2O,exhaust}$ (calculated) [bar]	0.148	0.216
$T_{H_2O,sat}(p_{H_2O,exhaust})$ [°C]	53.7	61.7
T_{exh} (measured) [°C]	54.2	61.5

cation gasoline (HF0437) with a known, and fixed H/C-ratio of 1.82.

Figure 4-13 depicts the water saturation pressure as tabulated by NIST. The calculated value of the corresponding exhaust gas water vapor partial pressure for the engine experiment was added along with the measured temperature for the low and high back pressure case. The difference between those observed points and the water saturation curve is less or equal to half a degree Celsius.

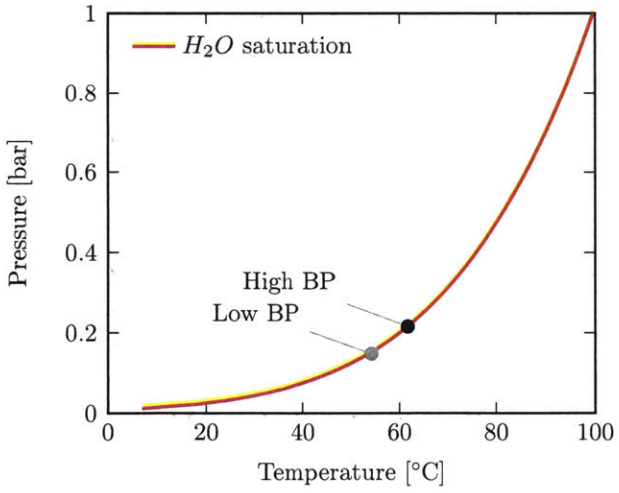

Figure 4-13: Water saturation pressure and temperature from National Institute of Standards and Technology[44]. The calculated partial pressure of the water vapor in the exhaust gas is marked against the temperature measured in the engine bench test on the abscissa. The deviation in each case is within half a Centigrade.

4.3 Catalyst Light-Off Modeling

Converter light-off models in literature characteristically are made up of several sub-models. All models are usually based on some kind of simplified geometry, furthermore there usually is a thermal-, a conversion-, and an O_2-storage model[67]. Depending on the application the detail of each model varies widely. In the following we'll discuss the necessary level of detail for each of those models required to accurately model converter light-off with back pressure before developing a suitable model that will be validated by experimental data.

The flow bench experiments have shown that the conversion efficiency of the converter was independent of back pressure for the relevant operating conditions, compare Section 4.1. And hence it is not necessary to develop a detailed, reaction based model for the conversion during light-off with back pressure, as many detailed reaction models without back pressure can be found in literature compare Section 2.2. Another drawback of detailed reaction models is that they are usually specific to a certain converter and require a lot of effort to adapt to different converters[?]. Here we'll be using the light-off curve from the flow bench experiment as a static temperature dependent conversion efficiency of the converter for hydrocarbon. The same curve is used for carbon monoxide conversion, but shifted towards lower temperatures by 45 °C based on a value found in literature[27].

The cerium oxide (CeO_2) allows the converter surface to store oxygen, which is released if the oxygen concentration in the feed gas falls below stoichiometric and zirconium oxide (ZrO_2) increases the high temperature stability of the CeO_2[54]. However, these effects are mostly noticeable during transient or acceleration periods in which the air to fuel ratio fluctuates significantly and is not important during the fast-idle period following cold start[67]. Henceforth, we will ignore the oxygen storage capacity of the converter and not develop any kind of oxygen storage sub-model.

Thermal light-off models in literature have been developed ranging from lumped to detailed three-dimensional models[67]. Lumped thermal models are usually not very useful to describe light-off because they cannot capture the significant temperature

gradient in axial direction of the converter that influences early conversion significantly. Instead lumped or simple 1D-models are used when real time processing with limited hardware capabilities is necessary[65].

While three-dimensional models are the most accurate, they require elaborate solvers, and significant computation time to numerically solve a reasonably sized mesh structure[36]. A one-dimensional thermal model can be used, that is relatively simple to solve, reduces computational time significantly, and at the same time describes the light-off reasonably well. The temperature gradient in radial direction is significantly less important than in axial direction as can be illustrated using a simple scaling argument. First the thermal resistances in radial direction are considered. The convective resistance (R_{conv}) between the gas and wall is given by,

$$R_{conv} = \frac{1}{h \cdot A} \tag{4.30}$$

where h is the convective heat transfer coefficient, which is a function of the Nusselt number (Nu), and A the cross-sectional area in radial direction. For internal, laminar flow in a square channel with constant wall heat flux, the Nu is a constant defined by,

$$Nu_{L_g} = \frac{h \cdot L_g}{k_g} = 3.61 \text{ [34]} \tag{4.31}$$

where L_g is the channel height, and k_g the heat conductivity of the gas. The conductive thermal resistance for the wall in radial direction is given by,

$$R_{cond} = \frac{L_w \cdot A}{k_w} \tag{4.32}$$

where L_w is the wall thickness, and k_w the heat conductivity of the wall. Substituting in rearranging Equations 4.30 - 4.32 gives the ratio of thermal resistances similar to the Biot number in radial direction as,

$$\frac{R_{cond}}{R_{conv}} = \frac{L_w}{k_w} \cdot h = \frac{L_w}{k_w} \cdot \frac{Nu_{L_g} \cdot k_g}{L_g} = Nu_{L_g} \cdot \frac{L_w}{L_g} \cdot \frac{k_g}{k_w}. \tag{4.33}$$

The wall thickness is approximately one tenth of the channel height. The heat conductivity of the substrate is in the order of $30\,\mathrm{W\,m^{-1}\,K}$ (value for aluminum oxide), and approximately three orders of magnitude larger than that of the exhaust gas ($0.02\,\mathrm{W\,m^{-1}\,K}$ for air), and hence the ratio of resistances can be estimated by,

$$\frac{R_{cond}}{R_{conv}} \approx Nu_{L_g} \cdot \frac{1}{10} \cdot \frac{1}{1000} < 4 \cdot 10^{-4} \tag{4.34}$$

And thus the thermal resistance of the wall in radial direction is negligible, meaning that the wall will be at practically the same temperature as the flow for a given axial position. In reality, there is a temperature gradient in radial direction due to the heat loss to the environment through the outer converter surface. However, it is relatively smaller than in axial direction and will henceforth be neglected.

The one-dimensional thermal model is based on a first law approach for each, the solid and gas phase. The control volume (CV) used to develop the conservation equations is shown in Figure 4-14.

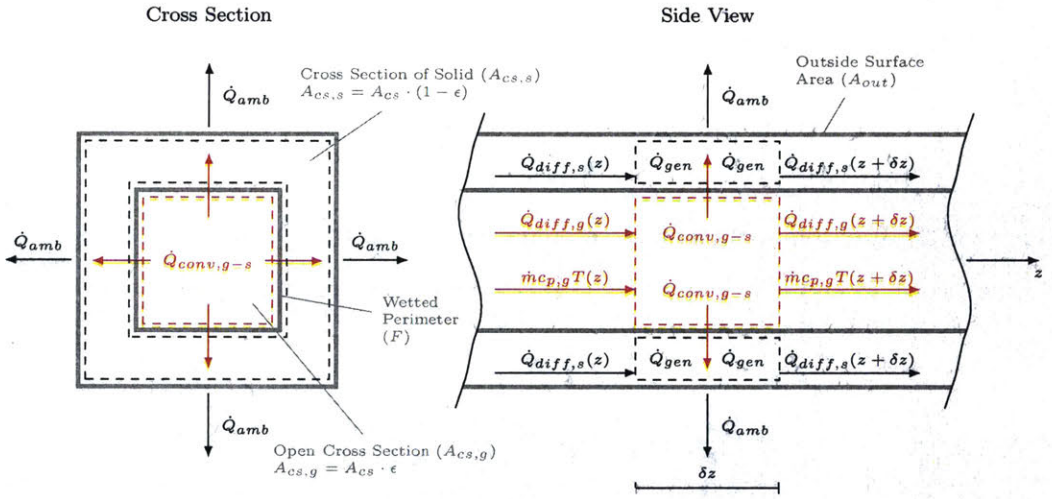

Figure 4-14: Schematic of a quadratic converter channel with control volume for gas phase (red) and solid phase (black). The associated heat flows are marked in the respective colors, and all geometric quantities are shown in gray. The wall dimensions are exaggerated for clarity, actual wall thickness is approximately one tenth of the channel height.

Conservation of energy dictates that the change of energy of the gas phase in the control volume is the sum of all energy flowing in and out of it in the absence of work.

$$\dot{E}_{CV,g} = \sum \dot{Q}_i - \cancelto{0}{\dot{W}} = \dot{Q}_{diff,g} - \dot{Q}_{conv,g} - \dot{Q}_{conv,g-s} \tag{4.35}$$

And hence the change of energy in the control volume of the gas phase is due to diffusion through the gas in axial direction, convection of the gas through the channel in axial direction and convective heat transfer between the gas and the converter wall. Using heat transfer correlations for the control volume shown in Figure 4-14 and substituting in to Equation 4.35

$$m_g c_{p,g} \frac{\delta T_g}{\delta t}\bigg|_{CV} = A_{cs,g} k_g \frac{\partial T_g}{\partial z} + \dot{m}_g c_{p,g} \left(T_g(z+\delta z) - T_g(z)\right) + hF\delta z(T_s - T_g)\bigg|_z \tag{4.36}$$

where the index g denotes quantities related to the exhaust gas, m_g the mass of exhaust gas in the CV, c_p the heat capacity, $A_{cs,g}$ the cross section of the channel perpendicular to the gas flow, k the heat conductivity, h the convective heat transfer coefficient between channel wall and gas, F the wetted perimeter of the channel, and T_s the temperature of the solid wall. The exhaust gas mass can be expressed in terms its density and the control volume,

$$m_g = \rho_g \cdot V_{CV} = \rho_g \cdot A_{cs,g} \cdot \delta z = \rho_g \cdot \epsilon \cdot A_{cs} \cdot \delta z \tag{4.37}$$

where ϵ is the fraction of open cross-sectional area of the total area (A_{cs}). Substituting in Equation 4.36 and dividing by ($A_{cs} \cdot \delta z$) yields and expression for a volume element of gas,

$$\epsilon \cdot \rho_g c_{p,g} \frac{\delta T_g}{\delta t}\bigg|_{CV} = \frac{\epsilon}{\delta z} \cdot k_g \frac{\partial T_g}{\partial z} + \frac{\dot{m}_g}{A_{cs}} c_{p,g} \frac{(T_g(z+\delta z) - T_g(z))}{\delta z} + h\frac{F}{A_{cs}}(T_s - T_g)\bigg|_z \tag{4.38}$$

taking the limit yields,

$$\epsilon \cdot \rho_g \cdot c_{p,g} \cdot \frac{\partial T_g}{\partial t} = \epsilon \cdot k_g \cdot \frac{\partial^2 T_g}{\partial z^2} + \frac{\dot{m}_g}{A_{cs}} \cdot c_{p,g} \cdot \frac{\partial T_g}{\partial z} + h \cdot \frac{F}{A_{cs}} \cdot (T_s - T_g) \tag{4.39}$$

a similar expression can be found in literature[65]. Similarly an expression for the solid phase can be developed. However, a generation term is added to the energy balance

because of heat release from carbon monoxide and hydrocarbon conversion on the catalytic surface, as well as the convective heat loss to the environment through the outer surface of the converter. The energy balance for the solid phase becomes,

$$\dot{E}_{CV,s} = \sum \dot{Q}_i - \overset{0}{\dot{W}} = \dot{Q}_{diff,s} - + \dot{Q}_{conv,g-s} + \dot{Q}_{gen,\mathrm{HC}} + \dot{Q}_{gen,\mathrm{CO}} - \dot{Q}_{amb} \tag{4.40}$$

The terms can be developed similar to the gas phase with a governing partial differential equation per converter volume given by,

$$\rho_s \epsilon^* c_s \frac{\partial T_s}{\partial t} = \epsilon^* k_s \frac{\partial^2 T_s}{\partial z^2} + h \frac{F}{A_{cs}} (T_s - T_g) + \frac{F}{A_{cs}} \sum (-\Delta H_j R_j) - \frac{A_{out}}{V_s} h_{amb} (T_s - T_{amb}) \tag{4.41}$$

where ϵ^* is the fraction of solid cross-sectional area of the converter ($\epsilon^* \equiv 1 - \epsilon$), T_s the temperature of the solid phase, ΔH_j heat release from reaction j, R_j rate of reaction of j per active surface, A_{out} the outer surface area of the converter that is the boundary to the environment, V_s the volume of the solid phase, h_{amb} the convective heat transfer coefficient between converter and the environment, and T_{amb} the ambient temperature.

The governing partial differential equations (Equation 4.39, and Equation 4.41) describing the temperature evolution in the gas and solid phase respectively are coupled by the convective heat transfer between the two phases. Both equations are elliptic partial differential equations (PDEs) with the one time t and one space z variable. The system of elliptic PDEs can be solved numerically as an initial-boundary problem with a commercially available solver in Matlab (*pdepe*). And an approximate numerical solution always exists. At cold-start the converter is in equilibrium with the environment, and hence the ambient temperature serves as the initial condition or mathematically,

$$T_s(t = 0, z) = T_{amb} \tag{4.42}$$

$$T_g(t = 0, z) = T_{amb} \tag{4.43}$$

and the boundary conditions are given by,

$$\frac{\partial T_s(z_l,t)}{\partial z} = 0 \tag{4.44}$$

$$\frac{\partial T_s(z_r,t)}{\partial z} = 0 \tag{4.45}$$

$$T_g(z_l,t) = T_g^{in} = T_1 \tag{4.46}$$

$$\frac{\partial T_g(z_r,t)}{\partial z} = 0 \tag{4.47}$$

where z_l is the position of the left boundary, and z_r the one of the right boundary. Setting the temperature gradient at the boundary to zero is a simplification that is not true in reality. However, it is a good approximation for the unknown boundary conditions that is also widely used in literature[35,61]. The method chosen could be improved by an iterative approach, where the results of the simulation in the vicinity of the boundary are used to calculate a linearized temperature gradient which serves as boundary condition for the subsequent run, which would be repeated until the difference in temperature from simulation to simulation is below a defined threshold.

There is a discontinuity in the converter due to the space between the two bricks, compare Figure 3-1. And hence the model is solved for each, the first, the second second brick as well as for the space between the two, where the fraction of open cross-sectional area (ϵ) changes. For a flow from left to right, the calculated values for the right boundary of the first brick serve as the input for the left boundary of the empty space, which results in a right boundary condition serving as the input for the left boundary of the second brick.

The simulation results agree well with the temperature transients observed during the engine experiment, compare Figure 4-15. However, the model does not include condensation of water vapor on the catalytic surface. While there is a difference during the temperature transients around the saturation temperature of 54.2 °C and 61.5 °C for low and high back pressure respectively, this is not significant for the overall light-off process. The latent heat absorbed by the converter during condensation is recovered by the water when it vaporizes again before leaving the converter. Further-

more the saturation temperature at which the temperatures plateau are significantly below the temperature at which conversion first occurs.

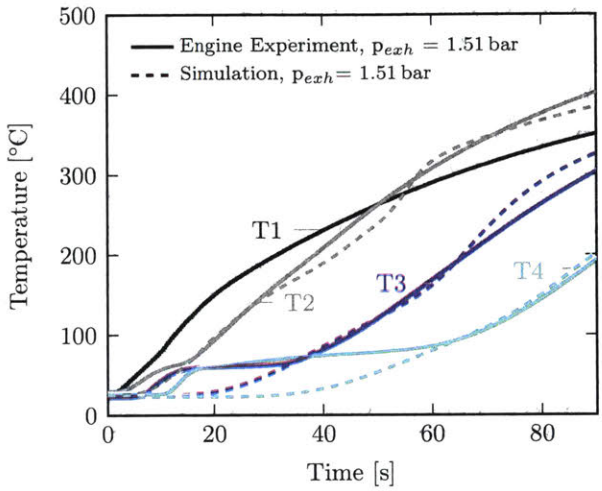

Figure 4-15: The converter light-off model with back pressure agrees well with experimental data from engine bench tests. The model does not include condensation as it is not important to the overall light-off behavior, and hence there is a difference between observation and simulation at low temperatures.

The model derived above is numerically simple to solve, and applicable to any three-way catalytic converter. It does, however, require a hydrocarbon and carbon monoxide light-off curve as a function of temperature from a flow bench test. Any other geometric properties can easily be measured or estimated from manufacturer's data.

Chapter 5

Conclusion Converter Light-Off with Back Pressure

Flow bench experiments have shown that back pressure had no influence on the three-way catalytic converter HC-conversion efficiency for space velocity ranging from $10{,}000\,h^{-1}$ to $34{,}000\,h^{-1}$, which is typical during operation before light-off. It was confirmed that neither static nor dynamic back pressure changes had any influence of the converter's light-off behavior for the operating conditions investigated.

Furthermore it was found that the mass flow rate at quasi-steady state had no influence on the conversion kinetics, for rates ranging from $30\,kg\,h^{-1}$ to $40\,kg\,h^{-1}$. And that the ratio of oxygen molecules to reactants had no influence on the conversion efficiency as long as there were enough O_2 molecules to oxidize that not fully oxidized species in the exhaust gas, i.e. for stoichiometric or lean exhaust gas composition. And hence it can be concluded that the converter's conversion efficiency is a function of temperature only, and that three-way catalytic converter light-off with back pressure is a physical effect through change in engine operation only.

It was found that back pressure increases the pumping work of the engine. To maintain the same net indicated mean effective pressure and engine speed during the fast idle condition, the engine needs to be de-throttled resulting in a larger air intake and exhaust gas mass flow rate. Simulations confirmed by experiment showed that the exhaust gas mass flow rate increased linearly with back pressure, from $34.7\,kg\,h^{-1}$

at 1.02 bar to 45.5 kg h^{-1} at 2.0 bar for the specific engine and operating condition investigated. Furthermore the exhaust gas temperature in the exhaust runner increased due to lesser expansion during the blow down process, which was confirmed by simulations. At a clock time of 90 s the observed exhaust gas temperature with a back pressure of 1.51 bar was 480 °C compared to 400 °C for the baseline case at 1.02 bar back pressure, a change of 80 °C or 20 %.

The higher temperature in the exhaust runner with back pressure was compensated by larger post-oxidation in the low back pressure case resulting in the same temperatures at converter inlet with and without back pressure. The slightly larger enthalpy flow rate of the exhaust gas at converter inlet at the same temperature level is attributed to increased exhaust gas flow rate from engine de-throttling.

A one-dimensional thermal model based on energy conservation was developed that agrees well with experimental results from converter light-off during bench tests. The model for solid converter and exhaust gas phase incorporates convection and diffusion, while radiative heat transfer is only lumped into the convective heat loss to the environment. Heat release from hydrocarbon, and carbon monoxide conversion on the catalytic surface is assumed to happen in the solid phase, and conversion is simulated to occur based on the static, temperature dependent light-off curves from the flow bench experiment. An oxygen storage sub-model was ignored as it is not significant for the investigated operating condition, based on observations from literature.

The model is easily transferable to any other system of engine, and three-way catalytic converter. It only requires temperature dependent light-off curves for HC and CO conversion, which will vary for various converters.

5.1 Recommendations for Future Work

In this research the effect of back pressure on engine and three-way catalytic converter during fast-idle following cold-start was investigated for a constant nominal engine operating point to further fundamental understanding of the physical and chemical

processes involved. Modern production engines usually depend on a highly transient fast-idle strategy following cold-start in regard to engine speed and spark timing as a trade-off to achieve optimum emissions, fuel consumption, cat light-off, and driveability such as noise vibration, and harshness. The following research ides can further a more complete understanding of the areas mentioned.

- Development of a detailed, cycle resolved post-oxidation model from engine exhaust valve to converter inlet for transient strategies
- Experimental validation of back pressure model under transient engine operating strategies at fast-idle

Chapter 6

Part II: Cycle-to-Cycle Variation

This chapter will discuss the importance of cycle-to-cycle variation (CCV) on engine operation and fuel efficiency. Furthermore it will discuss the current state of research in that area, and some current technical solutions to mitigate the impact of CCV. Lastly, the research goal of this study will be outlined.

6.1 Motivation

Cycle-to-cycle variation potentially reduces the emissions and fuel consumption performance of the internal combustion engine significantly. Additionally cycle-to-cycle variation limits the possible range of engine operating conditions. At low speeds and low loads CCV increase[28], which in turn increases the noise, vibration, and harschness (NVH) notably impacting driveability. Furthermore CCV impacts the lean burn and knock limit. In lean burn engines with potentially higher thermal efficiency combustion eventually becomes unstable with increasing dilution levels[4], large CCV requires nominal engine operation further away from the limit to avoid misfire, causing increase in emissions and fuel consumption, and hence limits the possible benefits from lean operation. In analogy, large cycle-to-cycle variation can lead to large fluctuations in knock intensity[51] and knock onset requiring mitigating strategies for this detrimental phenomena, such as enrichment or spark retard to be more aggressive further reducing engine efficiency.

A fundamental understanding of the causes for cycle-to-cycle variation is necessary to improve the development of future engine generations to further efficiency and emissions. Research has shown that causes for cycle-to-cycle variation of combustion are among others, the CCV of the in-cylinder flow field, the local and global air-fuel ratio, temperature and residual gas distribution, as well as ignition energy[28]. However, a thorough understanding of these highly stochastic phenomena is missing in literature, to the author's knowledge.

6.2 Background and Literature Review

Research by Kubota et al.[38] suggests that the local air-fuel ratio in spark plug vicinity impacts the cycle-to-cycle variation. They measured the air-fuel ratio next to the spark plug with an in-cylinder micro-Cassegrain sensor and found that variations in the local air-fuel ratio correlated well with the combustion variability, suggesting that homogenization can possibly reduce the cycle-to-cycle variation of combustion[38].

In addition to the local air-fuel ratio the spark plug itself can influence the cycle-to-cycle variation of combustion substantially. A detailed investigation by Pischinger and Heywood[59] into ignition systems showed that a larger breakdown energy caused faster initial flame development. However, they found in experiments with shrouded valves that the flame development angle (0-10% mass fraction burned, $\theta_{0-10\%}$) was not affected significantly by the faster initial flame growth when the flow energy increased substantially[59]. Furthermore they found in a different study, that CCV in the heat loss to the spark plug cause significant CCV in flame development at engine operating close to the stable limit[60]. The spark plug acts as a heat sink and can absorb part of the electrical spark energy directly as well as through heat transfer from the flame kernel[60]. Next to the size of the spark plug, the contact area between flame and electrode was found to be strongly dependent on the local flow field around the spark plug with smaller contact areas for cycles in which the flame was convected away from the electrode compared to cycles with a flame centered in the spark gap[60].

Aleiferis et al.[1] investigated the influence of spark plug orientation on CCV of

combustion in a lean burn stratified engine and found that a cross-flow orientation resulted in the lowest CCV of net indicated mean effective pressure, followed by a downstream and an upstream orientation, the latter resulting in the highest CCV. They also found that the crank angle of 5% mass fraction burned correlated well with the flame size and volume estimated from a two-view projected enflamed area at 40 °CA after ignition timing[1]. The results from Pischinger and Heywood[59,60] and Aleiferis et al.[1] suggest the a strong influence of the flow field on cycle-to-cycle variation of combustion beyond the ignition system.

The influence of charge motion on dilute combustion, either in lean burn engines or at high exhaust gas recirculation (EGR) rates, has been investigated widely in literature. Berntsson et al.[7] found the benefits of increased tumble motion to be a higher EGR tolerance and combustion efficiency of the single cylinder engine used, at the same time leading to increased combustion stability and reduced combustion duration. Similarly Dulbecco et al.[19] found that the cycle-to-cycle variation of the net indicated mean effective pressure was reduced as the tumble intensity and motion was increased over a wide range of operating conditions. Omura et al.[56] observed an increase in flow velocity for high tumble and as a result reduced CCV in the flame development angle ($\theta_{0-10\%}$), which in turn improved the CCV in the combustion center ($\theta_{50\%}$).

Efforts have also been made to develop detailed simulation models to describe cycle-to-cycle variation in combustion. Scarcelli et al.[66] developed a Reynolds Averaged Navier-Stokes (RANS) simulation and found that CCV of combustion were mainly caused by the variability of the in-cylinder flow after investigating significant physical and chemical quantities. Zhao et al.[75] used a more detailed large-eddy simulation (LES) approach with similar result that the cycle-to-cycle variation in burn rates can be attributed to the change in velocity flow-field in vicinity of the spark gap at ignition timing. Furthermore they found that there was no pattern in the occurrence of high and low cycles confirming the stochastic nature of cycle-to-cycle variation in simulation and experiment[75]. In an effort to reduce lengthy computation times of tens to hundreds of consecutive cycles that can be in the order of months

for detailed LESs Ameen et al.[2] have developed a parallel LES approach that was able to give accurate predictions of CCV in less than one-tenth the time for conventional approaches. Their approach was based on dissecting the consecutive cycles into multiple, shorter simulations that were run in parallel where the initial velocity field was perturbed based of in-cylinder turbulence intensity as a surrogate for a previous virtual cycle[2].

6.3 Research Goals

This study aims to quantify the cycle-to-cycle variation of combustion for a modern modern turbocharged 4-stroke passenger car SI engine. Specifically it will,

- quantify the influence of engine and operating parameters on cycle-to-cycle variation
- quantify the influence of cycle-to-cycle variation on knock behavior of the engine

Chapter 7

Experimental Setup Cycle-to-Cycle Variation

This chapter describes the class of modern turbocharged four-stroke passenger car SI-engines that the research engine used in this study belongs to. Furthermore it outlines the experimental setup that was used to investigate cycle-to-cycle variation, from the setup of the engine on the test bench to peripherals and data acquisition system used. This is important to interpret the experimental results properly.

7.1 Engine

The General Motors Company LTG engine is the third generation of Ecotec engines, and hence the successor of the second generation LNF engine used for the converter light-off experiments, compare Section 3.3.

Even though the basic engine architecture is similar to the LNF engine and displacement is the same, important updates have been made especially in regard to improve friction and fuel economy as well as durability for higher engine loads. Table 7.1 lists the engine specifications of the LTG Ecotoc gen III engine. The compression ratio of the 4-cylinder in-line engine has been increased to 9.5:1, and there have been slight improvements in the peak power output from 190 kW to 205 kW and in the peak torque output from 353 N m to 400 N m. In its stock configuration

the LTG engine is equipped with a twin-scroll turbocharger. In this research setup, however, the turbocharger has been replaced by an externally powered supercharger. Furthermore a chamber for external pre-mixed fuel delivery has been added to allow for either pre-mixed of direct-injected fuel delivery, compare Section 7.2 for the setup of the engine on the test bench, supercharger, and pre-mixed chamber location.

Table 7.1: General Motors Ecotec generation III LTG engine specifications. The twin-scroll turbocharger of the production engine setup is not used in this research. Power and torque were SAE certified with Chevrolet Camaro and may differ for other models.

Engine Specifications	Value and Unit
Type	2.0 L I-4
Displacement	1998 cm^3
Compression Ratio	9.5:1
Valve Configuration	Dual overhead camshafts, VVT
Valves per Cylinder	4
Valve Lifters	Hydraulic roller finger follower
Bore / Stroke	86.00 / 86.00 mm
Fuel System	DI or Pre-Mixed
Horsepower	205 kW @ 5600 min^{-1}
Torque	400 N m @ 3000 min^{-1} to 4500 min^{-1}
Maximum Engine Speed	7000 min^{-1}
Block	Cast aluminum 319T7
Cylinder Head	Cast aluminum 356T6 Rotocast
Crankshaft	Steel
Camshaft	Assembled steel
Connecting Rod	Forged powdered metal

Cylinder Head and Camphasers

The dual overhead camshafts are equipped with camphasers that can be actuated independently of each other. In the parked position there is a negative valve overlap of 20 °CA symmetrically around top dead center, compare Table 7.2 for valve opening and closing for parked and fully phased camshaft positions. In the fully phased position there is a positive valve overlap of 80 °CA.

The baseline valve timing chosen for all experiments except if specifically noted otherwise was IVO at 0 °CA aTDC and EVC at −10 °CA aTDC with a negative valve overlap of 10 °CA. The detailed baseline valve timing information is noted in Table 7.3.

Table 7.2: Cam timing for parked and fully phased position of the LTG engine as well as opening duration and maximum cam lift. The valve timing noted corresponds to 0.25 mm valve lift.

Valve	Parked Position	Fully Phased Position
Intake valve opening (IVO)	10 °CA aTDC	−40 °CA aTDC
Intake valve closing (IVC)	60 °CA aBDC	10 °CA aBDC
Intake valve opening duration	230 °CA	
Maximum intake valve lift	10.4 mm	
Exhaust valve closing (EVC)	−10 °CA aTDC	40 °CA aTDC
Exhaust valve opening (EVO)	−50 °CA aBDC	0 °CA aBDC
Exhaust valve opening duration	220 °CA	
Maximum exhaust valve lift	10.5 mm	

There are several reasons this specific timing with slightly negative valve overlap was chosen. First, it reduces flow interactions between the intake and exhaust which differ significantly with engine operating point. With positive valve overlap, the flow reverses during overlap for heavily throttled low load operation, and for wide open throttle or boosted operation there is significant scavenging. Second, some of the experiments occurred with a 3D-printed polymer insert in the intake port to change the intake flow and tumble characteristic of the engine, a reverse flow of the hot burned gases to the intake port would have significantly damaged that part. And third, while the chosen valve timing does not exactly equal the stock calibration it is close to it over a wide range of operating conditions.

Table 7.3: Baseline cam timing used for the cycle-to-cycle variation experiments, unless specifically noted otherwise. All valve timing noted corresponds to 0.25 mm valve lift.

Valve	Baseline Experiment Position
Intake valve opening (IVO)	0 °CA aTDC
Intake valve closing (IVC)	50 °CA aBDC
Exhaust valve closing (EVC)	−50 °CA aBDC
Exhaust valve opening (EVO)	−10 °CA aTDC

Combustion System

The LTG engine and its combustion system are representative for an entire class of downsized, turbocharged gasoline engines. It features a dual overhead camshaft with

hydraulic roller finger followers, four valves per cylinder, pent-roof comubstion chamber with center mounted spark plug, and side mounted injector with high pressure common rail. The high pressure fuel pump allows for injection pressures of up to 200 bar. The piston surface is shaped to increase tumble motion inside the engine.

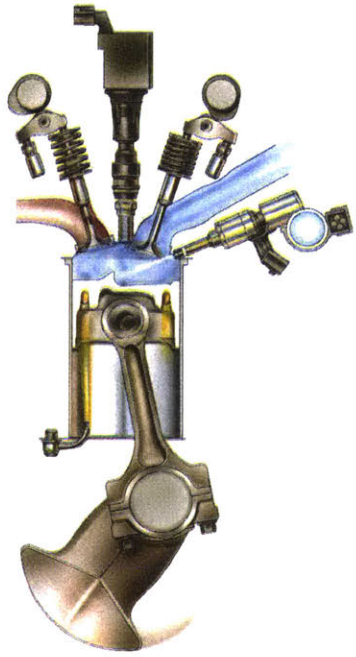

Figure 7-1: The combustion system of the LTG engine. Dual overhead camshaft with hydraulic roller finger followers, four valves per cylinder, center mounted spark plug, and side mounted injector with high pressure common rail. © General Motors

Combustion chamber and In-Cylinder Measurements

The pent-roof combustion chamber was outfitted with AVL GH14D piezoelectric pressure transducer with AVL's PH08 flame arrestor to reduce the influence of thermal shock on the measurements. Additionally the pressure transducer is mounted to the side of the combustion chamber away from the spark plug to reduce the influence of the flame front on the pressure measurements, compare Figure 7-2.

The spark plug is located in the center between the intake and exhaust valves. The side mounted high pressure fuel injector is on the intake side to support the charge motion of the intake air.

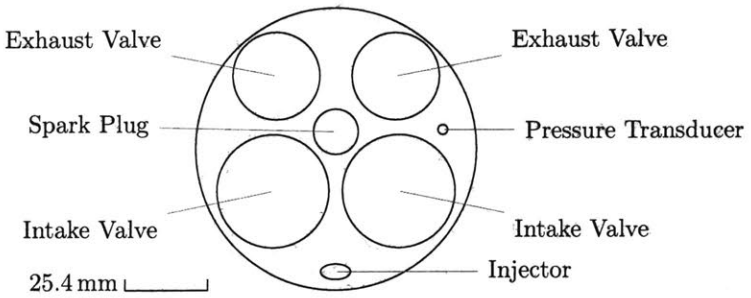

Figure 7-2: Pent-roof cylinder head design of the LTG research engine. Center spark plug, valves, fuel injector and the location of the pressure transducer are shown. Drawing to scale.

7.2 Test Bench and Auxiliaries

The LTG engine is setup on a test bench, in a configuration that differs from the stock engine setup significantly. The four cylinder in-line engine is operated as a single-cylinder engine and hence requires support from an electrical motor during low load operation to overcome the friction load from the three cylinders that are not fired. Single cylinder operation also results in a stronger pulsating flow requiring damping volumes in intake air and exhaust path. Furthermore an external supercharger is used instead of the twin-scroll turbocharger used in the stock configuration, resulting in additional modifications of the air path, which will be detailed in the following.

Motor and Dynonometer

The electrical motor, dynamometer and LTG engine are setup in a serial configuration with a fixed shaft that connects these devices permanently. The electrical motor can be used to motor the engine or support it during low load operation. The dynamometer controls the engine speed to a set value by absorbing the corresponding load. The brake torque of the engine as measured by the dynamometer is not recorded because it has no meaning given the additional friction torque from the motor and unfired cylinders.

Air Path

Single cylinder operation causes a more unsteady air flow into the engine compared to full engine operation. For that purpose damping volumes were installed into the intake air path to reduce pressure fluctuations and undesired pressure wave phenomena.

The air intake flow path is shown in Figure 7-3, after the air enters the air-filter there is a first, low pressure surge tank with a large volume. Downstream of the first surge tank is the supercharger, which is electrically driven and can be controlled independently of engine operation. Another, high pressure surge tank is located after the compressor functioning as a reservoir just upstream of the throttle valve. The butterfly throttle valve with a diameter of 36 mm from Bosch is controlled independently of the engine with a PID motor controller.

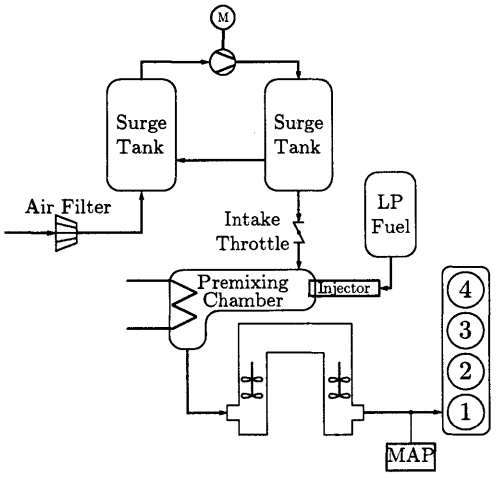

Figure 7-3: The air intake path from air-filter to the intake runner of the LTG engine.

Next is the heated premixing chamber where fuel can be injected, if the engine is not operated in direct injection mode. Another large volume, in similar function to the surge tanks further upstream, was installed upstream of the intake runner. This U-shaped volume is forty times larger than the intake port volume and there are two fans installed inside the straight parts of the U-shape to increase the air-fuel mixture quality. The intake air path is connected to the intake runner of cylinder one. The other three cylinders, suck ambient air directly through an intake air manifold separated from the environment only by small air filters.

Gasoline Mixing Chamber

The mixing chamber is made of an L-shaped copper pipe, that is wrapped in heating tape and an insulation, compare Figure 7-4. An active heating element is necessary to ensure the fuel gasifies completely, as the temperature can drop significantly because of the gasoline's heat of vaporization. A thermocouple measures the surface temperature of the mixing chamber, which is used as the process variable for a custom built LabVIEW code that controls the heater power with a PI-controller keeping the temperature steady within $\pm 0.25\,°C$.

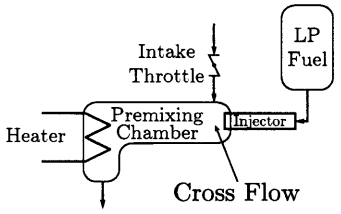

Figure 7-4: Mixing chamber in the air intake path of the LTG engine with heating element and injector.

The liquid fuel is injected along the axis of the mixing chamber in cross-flow to the air coming from the throttle valve. The injector used is a commercially available port fuel injector from Mazda. A damping tank in the fuel supply system ensures a constant fuel delivery pressure of 3 bar or 300 kPa.

The Mazda injector has been calibrated for a fuel pressure of 300 kPa. The fuel mass delivered through the injector is a linear function depending on the opening duration of the injector for all durations relevant in this investigation. The fuel mass delivered can be approximated by the following linear relationship,

$$m_f = 2.754 \cdot \Delta t_{inj} - 1.966 \quad [mg] \tag{7.1}$$

where m_f is the mass of fuel injected in mg, and Δt_{inj} the injection duration in ms.

Engine Coolant and Exhaust System

The exhaust manifold of the unfired cylinders, number two to four, exhausts air directly into the environment to reduce additional losses. The fired cylinder's exhaust runner exhausts the burned mixture directly into a straight pipe where the NDIR and oxygen sensor are located, compare Figure 7-5.

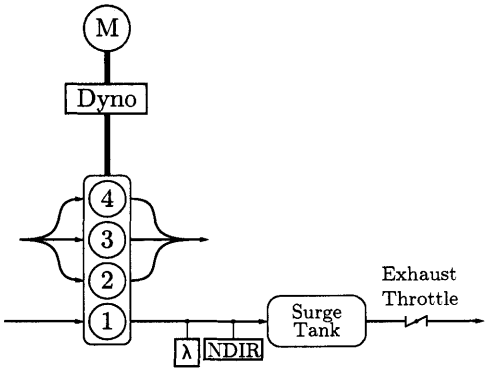

Figure 7-5: Exhaust system of the LTG research engine with locations of oxygen sensor and nondispersive infrared detector.

The engine coolant is conditioned to be at 85 °C when entering the engine block. It is pumped by an electrical pump that is independent of the engine, and which is downstream of a large damping tank with an immersion heater, compare Figure 7-6. Once the engine coolant has reached its operating temperature heat is rejected by the heat exchanger in the circuit to an external, unconditioned water circuit. A LabVIEW PID controlled solenoid valve adjusts the water flow rate through the heat exchanger such that the coolant temperature is kept at 85 °C with an observed maximum deviation of ±0.15 °C.

The entire aforementioned setup including all relevant sensors is shown in Figure 7-7.

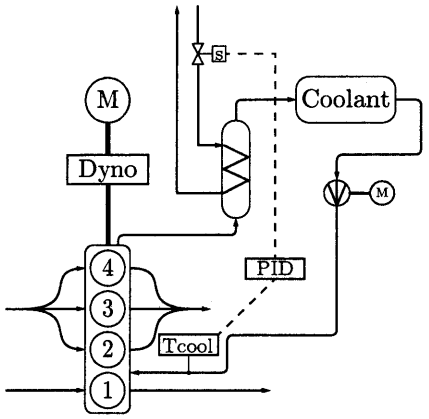

Figure 7-6: Engine coolant system circuit with PID controlled solenoid valve that controls the flow rate of the external water cooling circuit.

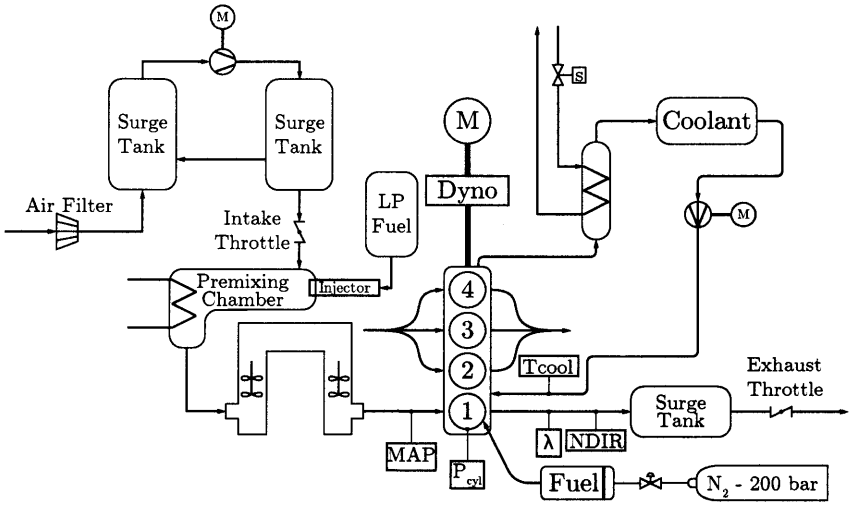

Figure 7-7: Test bench setup of the LTG engine including peripherals, intake air and exhaust path, gasoline premixing chamber, cooling system, dynanometer and electric motor.

7.3 Data Acquisition and Processing

The National Instrument cDAQ-9172 data acquisition chassis was used to record the sensor signals for all non-knocking experiments. Analogue samples were sampled with input modules of type NI-9215, while thermocouple signals were recorded with input modules of type NI-9211. The sampling rate was always one sample per crank angle degree for a total of 360 samples per crank angle revolution per channel.

For the knocking experiments, an Ethernet DAQ of type cDAQ-9188 was used, since it allowed the simultaneous sampling in the crank angle and time domain. The sampling rate of the cylinder pressure signal in the time domain was 100 kHz to capture the high frequency oscillations of the knocking combustion.

Pegging

Pressure measurements obtained by the AVL in-cylinder pressure transducer need to be corrected or pegged to a known absolute pressure, since piezoelectric pressure transducers inherently measure pressure changes rather than absolute pressures[12]. Other inherent measurement errors include a long-term or inter-cycle drift of the piezoelectric sensor requiring a pegging procedure for each and every cycle[12,39,63]. An approach widely used in literature is the one described by Randolph[62], where the cylinder pressure is pegged in the vicinity of intake bottom dead center to the absolute pressure in the intake manifold. In this case where the engine is operated in a single-cylinder configuration, it is pegged to the pressure in the intake pipe 10 cm upstream of the intake valve. At intake bottom dead center the intake valve is opened reasonably wide and there is little piston motion reducing dynamic pressure and wave effects.

The pegging approach used in this study is based on the Randolph[62] one with slight modifications. In the original paper the pressure offset was calculated by averaging three data points, sampled at bottom dead center, as well as one degree crank angle before and after. In this study the averaging window is ten degree crank angle wide (cf. Figure 7-8) increasing robustness against noise in the pressure signal. Furthermore the averaging window is offset from bottom dead center by five degree crank angle past bottom dead center, where the piston speed is still low but with less apparent flow reversal effects. The difference between the averaged in-cylinder pressure signal and manifold air pressure signal is the offset, whereas the absolute manifold air pressure is assumed to be the true pressure. The in-cylinder pressure for the entire cycle is offset by the scalar value calculated for each corresponding cycle.

Pegging the in-cylinder pressure signal is of extreme importance for the accuracy

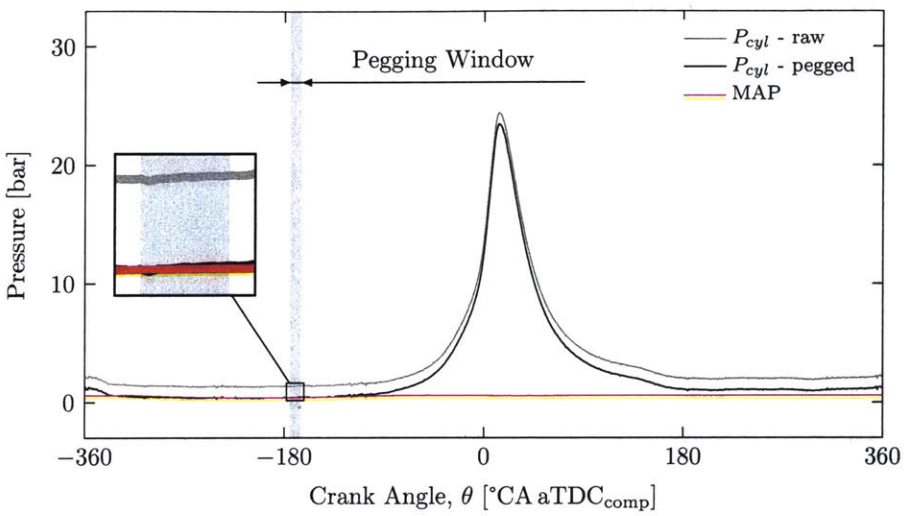

Figure 7-8: Pegging procedure adopted in this study. The raw pressure signal from the piezoelectric sensor is offset to match the manifold air pressure in the pegging window, with a width of 10 °CA.

of derived quantities such is polytropic index, apparent heat release rate, and gross indicated mean effective pressure. The net indicated mean effective pressure on the other hand is not sensitive to the pegging procedure since it is a closed integral over the entire cycle it only depends on pressure difference[16]. However, since the net indicated mean effective pressure is the volume weighted pressure integral the phasing of the in-cylinder pressure signal with respect to the crank angle position and thus cylinder volume is paramount. A mechanical gauge with an accuracy of 0.1 °CA was used to determine the bottom dead center signal (encoder) offset from the actual bottom dead center.

Effective Pressures

The engine load is characterized by the net indicated mean effective pressure in this study. It is useful as it denotes the work delivered to the piston over the entire four-stroke cycle per swept volume of the cylinder, thus making comparable between engines of different volumes. Mathematically it is defined as the integral of in-cylinder pressure with respect to cylinder volume over the entire cycle divided by the swept

volume[27],

$$W_{c,in} = \oint p\,\mathrm{dV} \equiv IMEP \cdot V_d \tag{7.2}$$

$$NIMEP = \frac{\oint p\,\mathrm{dV}}{V_d} \tag{7.3}$$

Apparent Heat Release Rate

The Rassweiler-Withrow method is a common way to calculate the apparent heat release rate found in literature. Rassweiler and Withrow[64] derived a method for sorting out the pressure changes due to combustion from an observed pressure card, which on a percentage basis was approximately equal to the percent of charge burned by weight at the corresponding instants in the combustion period. So it is essentially based on crank angle resolved in-cylinder pressure measurement. Even though this method includes several simplifications, mainly it neglects heat transfer effects, it is widely used and appears to be quite accurate[27]. The method defines the mass fraction burned by,

$$x_b = \frac{p^{\frac{1}{n}} \cdot V - p_0^{\frac{1}{n}} \cdot V_0}{p_f^{\frac{1}{n}} \cdot V_f - p_0^{\frac{1}{n}} \cdot V_0} \tag{7.4}$$

where x_b denotes the mass fraction burned, p the in-cylinder pressure, V the cylinder volume, and V_0, p_0 and V_f, p_f the volume and pressure at time of spark and end of combustion respectively. The Matlab code used to calculate the apparent heat release rate was developed by McKenzie[49].

Heat Release Schedule and Burn Angles

The cumulative heat release schedule is a non linear function of the crank angle and thus in itself difficult to compare with one another, compare Figure 7-9.

Several scalar values are commonly used to give a simplified description, whereas two types can be distinguished. The first being the angle of a particular mass fraction burned, and the second being burn angles. The former describes the absolute crank

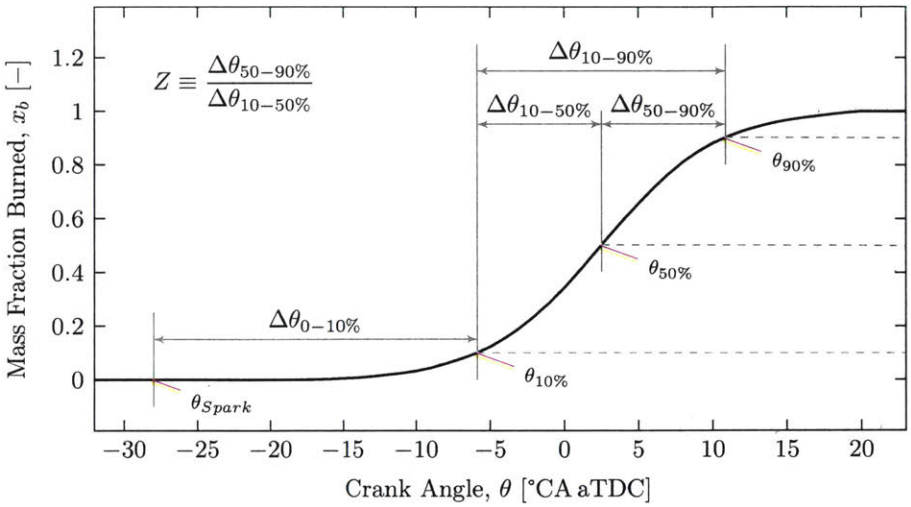

Figure 7-9: Definition of burn angles with an exemplary cumulative heat release schedule.

angle relative to the top dead center of the engine where a specific mass fraction was burned, i.e. $\theta_{50\%}$ denotes the crank angle where a mass fraction of 50 % was burned. Burn angles on the other hand denote the duration it takes the charge to burn from one specific mass fraction to another, i.e. $\Delta\theta_{0-10\%}$ is the duration it takes to burn from zero to ten percent of the mass in crank angles. A mass fraction of zero denotes the spark timing. The cumulative heat release schedule is computed for any crank angle with the Rassweiler-Withrow method and linearly interpolated. Commonly used mass fraction burned, and burn angles used in this study are:

- $\theta_{50\%}$ - combustion center
- $\theta_{0-10\%}$ - flame development angle
- $\theta_{10-90\%}$ - rapid burn angle

Knock

The in-cylinder pressure signal is filtered with a phase conserving digital high pass Butterworth filter to determine whether or not a cycle knocked. In this study a high pass filter with a cutoff frequency of 2.5 kHz was used at a pressure signal sampling frequency of 100 kHz, which is also used in literature[49]. Band pass filters with band

pass frequencies of 5 kHz to 12 kHz[13] or 5 kHz to 15 kHz[50] are also sometimes used, though they led to the same results here.

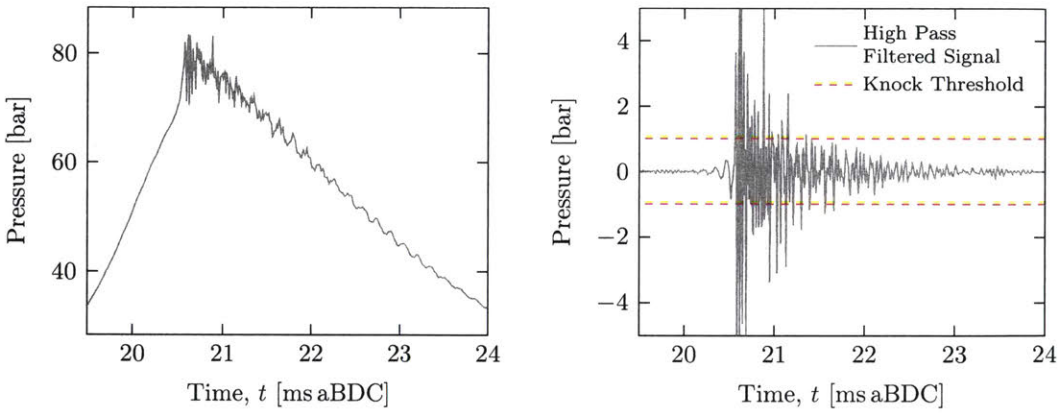

Figure 7-10: In-cylinder pressure signal sampled at 100 kHz for knocking combustion (left), and corresponding high pass filtered pressure signal (right) crossing the knock threshold of 1 bar several times.

Knock is said to occur when the high pass filtered in-cylinder pressure signal crosses the knock threshold commonly defined to be of an amplitude of 1 bar, compare Figure 7-10. The magnitude of knock is characterized by the knock intensity (KI), which is defined as the maximum absolute value of the filtered pressure signal, compare Figure 7-11. And thus the KI is independent of the pressure amplitude's sign.

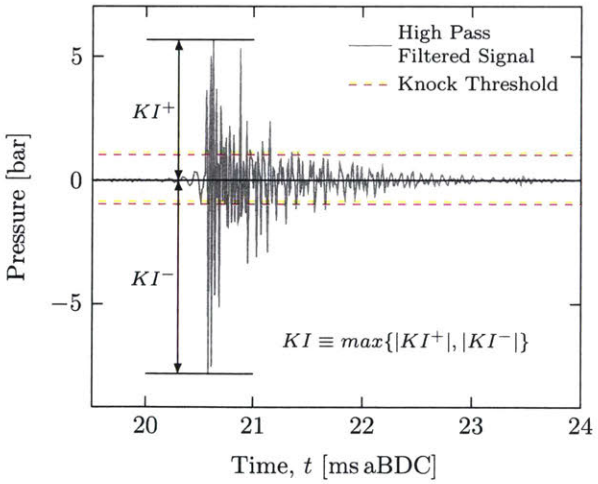

Figure 7-11: Definition of Knock intensity as the absolute value of the maximum amplitude of the filtered pressure signal.

Chapter 8

Cycle-to-Cycle Variation in Gasoline Engines

In this chapter a parameterization of the heat release schedule is defined that serves as a metric to quantify CCV of combustion. Subsequently the influences of intrinsic charge motion, residual gas mass fraction, engine speed and load, and increased charge motion on CCV are quantified for direct-injection and premixed combustion. Lastly, the influence of CCV on knock is investigated.

8.1 Parameterization of the Heat Release Schedule

The heat release schedule will serve as a metric to compare cycle-to-cycle variation of combustion. In itself it is a non trivial function of crank angle, and hence it is relatively difficult to compare the shape of the entire heat release schedule from cycle-to-cycle for a large number of data points. For a more practical approach the goal is to parameterize heat release schedule sufficiently with as little parameters as possible for a meaningful metric.

A wide range of operating points is needed to validate the parameterization universally across the engine operating map. The spark timing, engine speed, and load will be varied over a fairly wide range for that purpose. To ensure the same mass of fuel is trapped for each operating point with the same nominal load, the engine

is operated only with direct-injection for parameterization. The range of operating points is shown in Figure 8-1, where each point represents one thousand consecutive cycles for a total of forty-one thousand cycles.

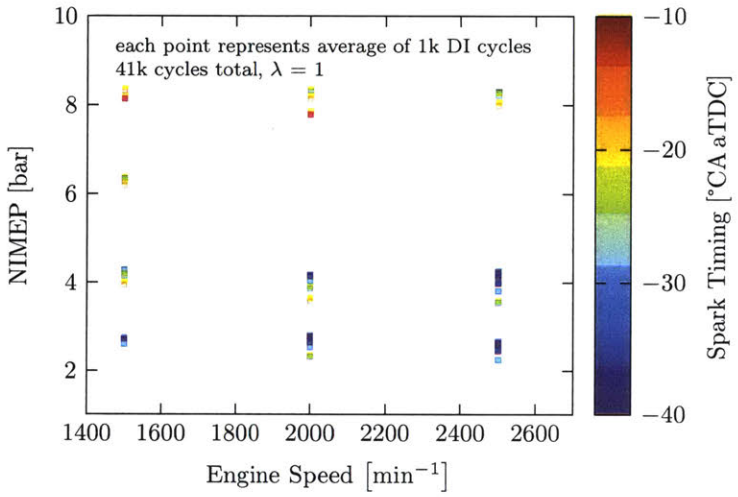

Figure 8-1: Operating conditions of the forty-one thousand direct injected cycles used for parameterization of the heat release schedule.

In a first step two parameters are chosen to parameterize the heat release schedule, the combustion center $\theta_{50\%}$ and the rapid burn angle $\theta_{10-90\%}$. The relationship between those two parameters for all forty-one thousand cycles is shown in Figure 8-2 in a relative frequency plot. To determine how well the heat release schedule can be parametrized by combustion center and rapid burn angle ($\theta_{50\%}$ and $\theta_{10-90\%}$) an arbitrary and exemplary three value pairs were chosen at a location with relatively high number of cycles observed but at the same time significantly different enough for to be representative for the entire sample taking into account fast- and slow-burn rates ($\theta_{10-90\%}$), as well as early and late combustion phasing ($\theta_{50\%}$). These value pairs are marked with P1-P3 in Figure 8-2.

The selection process for these points was as follows. All forty-one thousand cycles were binned by their combustion center with a fairly narrow bin width of 0.2 °CA. Subsequently all cycles from an arbitrarily chosen bin were chosen and these cycles were binned by their rapid burn angle in bins the size of 0.2 °CA. Out of these, a bin with a large number of cycles was chosen, and the heat release schedules of those

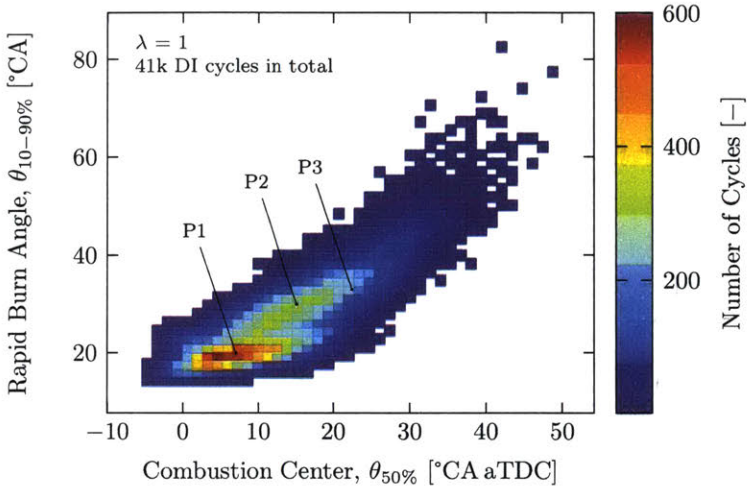

Figure 8-2: The rapid burn angle increases exponentially as a function of the combustion center and is largely independent of the operating condition. Compare Figure 8-1 for the various operating conditions of the forty-one thousand direct injected cycles shown above. The three points P1, P2 and P3 will be used to validate parameterization of the heat release schedule for their respective combustion center and rapid burn angles.

cycles as well as their corresponding operating points were compared.

For instance the combustion center for P1 is 7 ± 0.1 °CA aTDC, and 357 cycles out of the forty-one thousand satisfy this condition, compare the histogram in Figure 8-3a. From these cycles all the ones that had a rapid burn angle of 20 ± 0.1 °CA aTDC were chosen. A total number of 15 cycles, compare the histogram in Figure 8-3a. The corresponding heat release schedules were plotted in Figure 8-4 along with their corresponding operating points. The same process was repeated for a combustion center of 14.2 °CA aTDC and 21.4 °CA aTDC and a rapid burn angle of 30 °CA and 33 °CA respectively, compare Figure 8-5 to 8-8.

Two observations can be made for all those cases. First, heat release schedules from significantly different operating conditions can be described by the parameters and fall in the same bin when windowed by the aforementioned process. Second, while the difference between the heat release schedules in crank angle for the fifty percent mass fraction burned is inside a narrow window of 0.2 °CA width (by design), the spread increases for mass fractions burned towards either end of the S-curve. The reason is that the second parameter defines the duration of the fast burn angle, but not its symmetry around the combustion center. And hence a heat release schedule

with a long initial burn period ($\theta_{10-50\%}$) and short tail ($\theta_{50-90\%}$) can have the same overall rapid burn angle as a heat release schedule with short initial burn period and long tail as well as similar combustion center. That means that for asymmetric heat release schedules the parameterization becomes worse for heat release schedules as the symmetry parameter Z deviates from one. The symmetry parameter Z is defined by

$$Z \equiv \frac{\theta_{50-90\%}}{\theta_{10-50\%}} \tag{8.1}$$

compare Figure 7-9 for a geometric interpretation of Z.

From the aforementioned observations it seems reasonable that a better parameterization can be obtained using three parameters, combustion center ($\theta_{50\%}$), rapid burn angle ($\theta_{10-90\%}$), and symmetry parameter (Z). Using the same windowing process as for the two variable parameterization the corresponding heat release schedules and operating points are plotted in Figure 8-9 to Figure 8-14.

Since this parameterization is more restricting less cycles will have a heat release schedule within a narrow window, and hence the windowing process was performed twice, once for a bin width of 0.2 °CA and once for a bin width of 0.6 °CA. In either case the spread between the heat release schedules remains approximately constant throughout the entire burn duration indicating that the three variables parameterize the heat release schedule sufficiently well. The three-variable parameterization works well for heat release schedules across a wide range of operating points, same as with the two-variable parameterization.

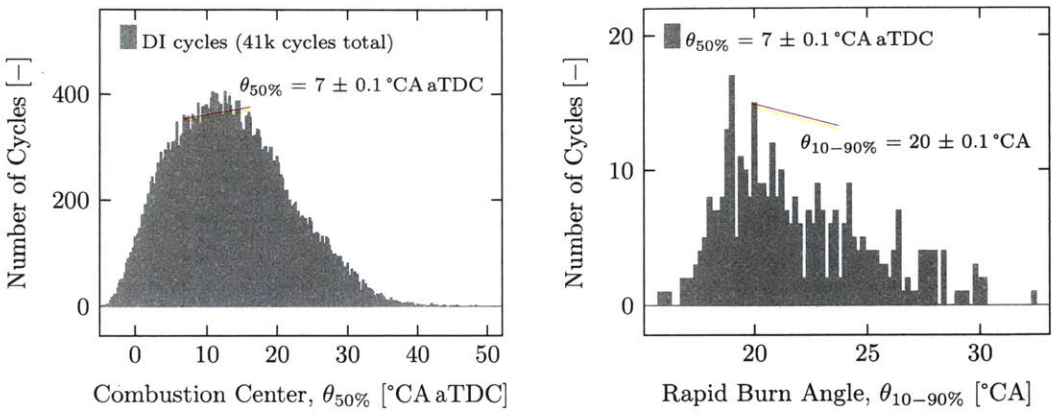

Figure 8-3: The forty-one thousand DI cycles are windowed out by a combustion center of 7 °CA aTDC (Figure 8-3a) and then according to a rapid burn angle of 20 °CA (Figure 8-3b).

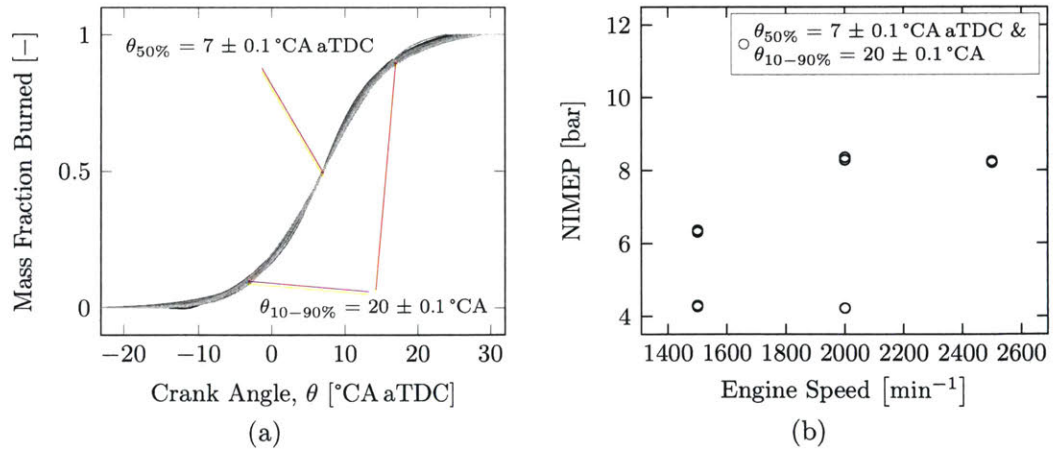

Figure 8-4: Heat release schedules resulting from the windowing process shown in Figure 8-3 are shown in the left figure (total of 15). The spread of the curves increases for crank angles further away from the combustion center. Their respective operating point is shown on the right.

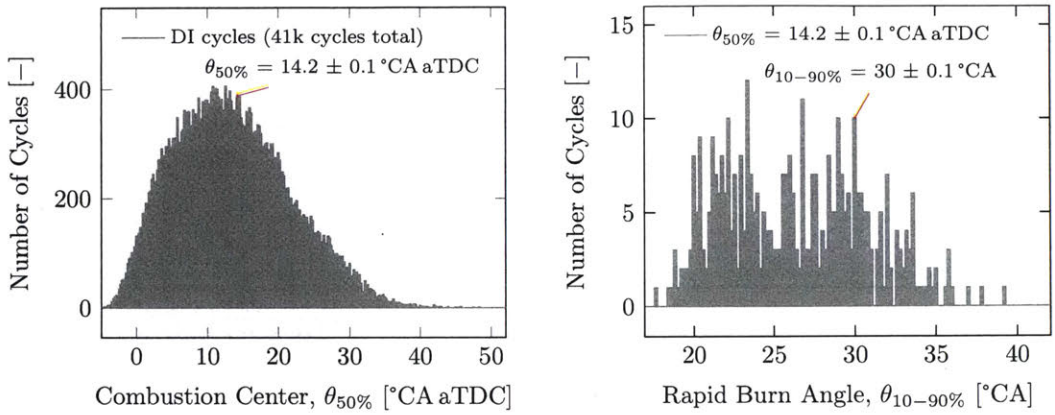

Figure 8-5: The forty-one thousand DI cycles are windowed out by a combustion center of 14 °CA aTDC (Figure 8-5a) and then according to a rapid burn angle of 30 °CA (Figure 8-5b).

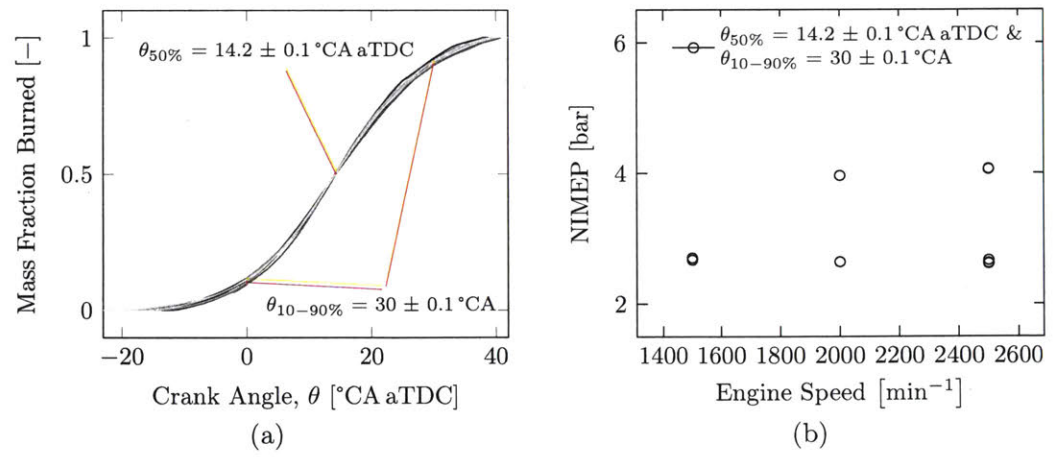

Figure 8-6: Heat release schedules resulting from the windowing process shown in Figure 8-5 are shown in the left figure (total of 10). The spread of the curves increases for crank angles further away from the combustion center. Their respective operating point is shown on the right.

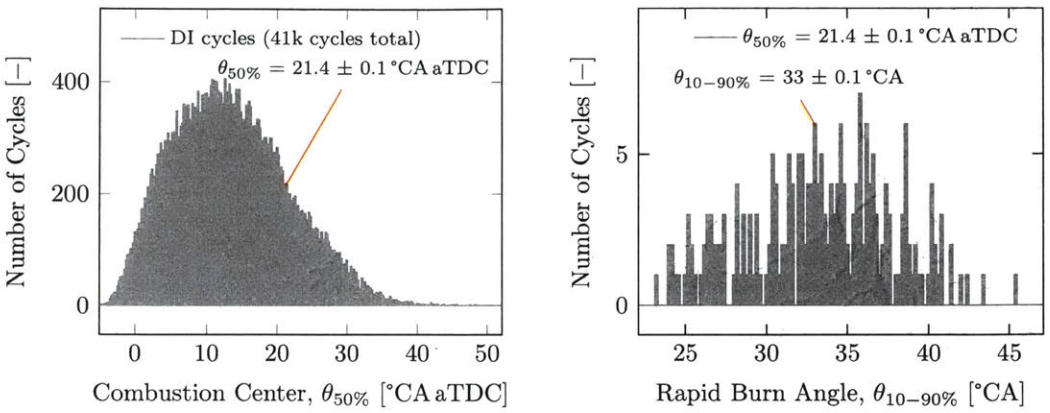

Figure 8-7: The forty-one thousand DI cycles are windowed out by a combustion center of 21.4 °CA aTDC (Figure 8-7a) and then according to a rapid burn angle of 33 °CA (Figure 8-7b).

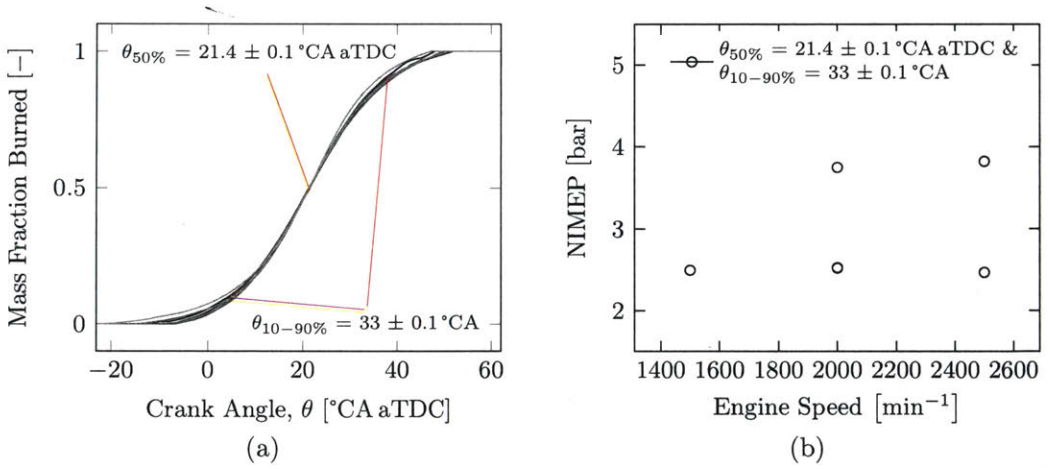

Figure 8-8: Heat release schedules resulting from the windowing process shown in Figure 8-7 are shown in the left figure (total of 6). The spread of the curves increases for crank angles further away from the combustion center. Their respective operating point is shown on the right.

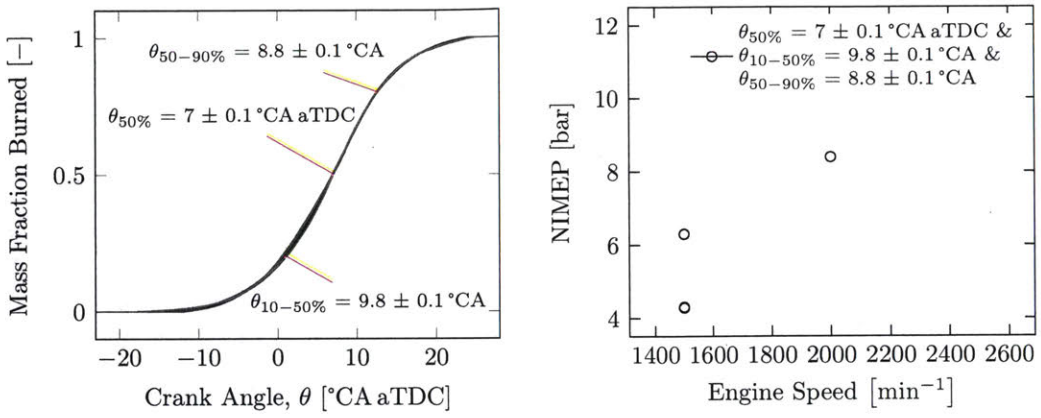

(a) Total of four cycles.

(b) Total of thirty-three cycles.

Figure 8-9: Three-variable parameterization with narrow window, the spread of the burn rates is equal to the window size (total of 5 points).

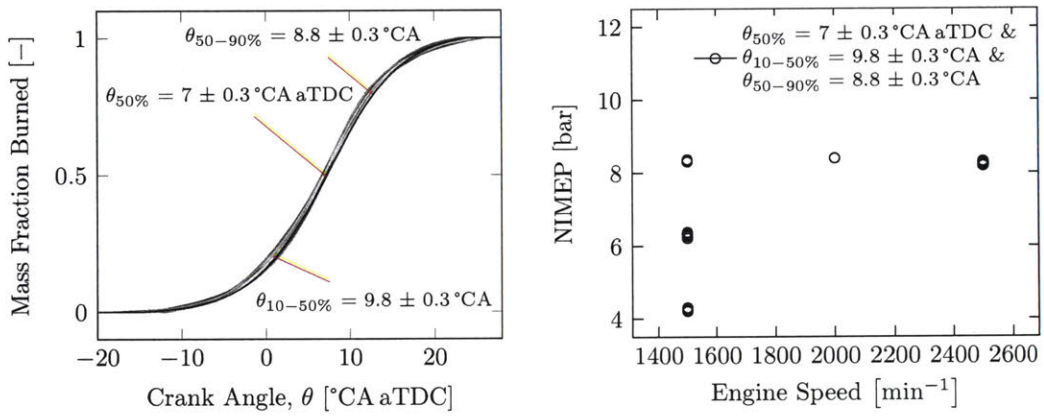

(a) Total of four cycles.

(b) Total of thirty-three cycles.

Figure 8-10: Three-variable parameterization with wider window, the spread of the burn rates is equal to the window size (total of 33 points).

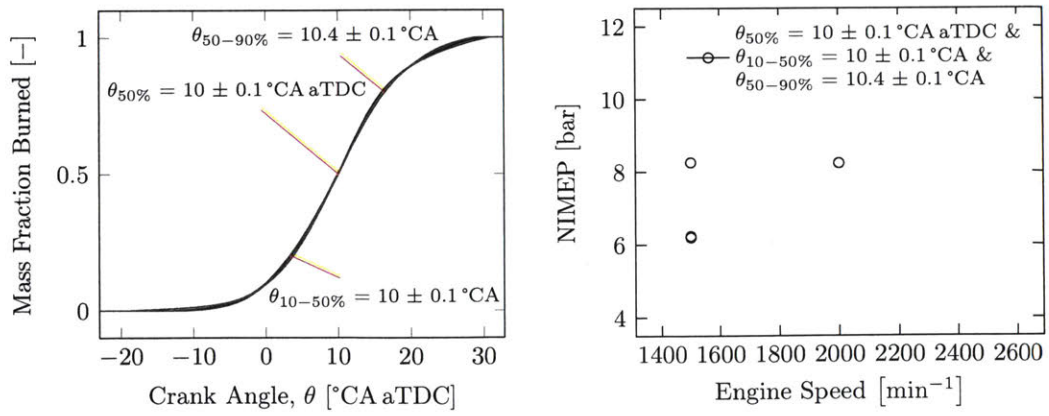

(a) Total of four cycles.

(b) Total of thirty-three cycles.

Figure 8-11: Three-variable parameterization with narrow window (total of 4 points).

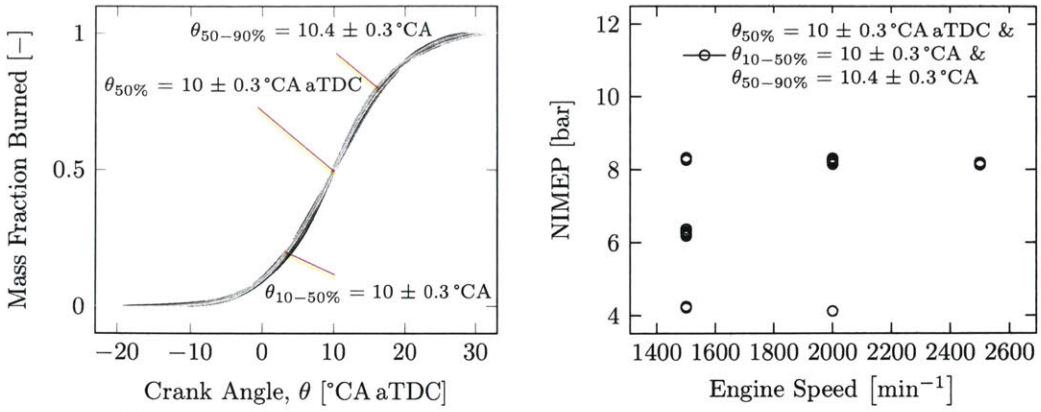

(a) Total of four cycles.

(b) Total of thirty-three cycles.

Figure 8-12: Three-variable parameterization with narrow window (total of 32 points).

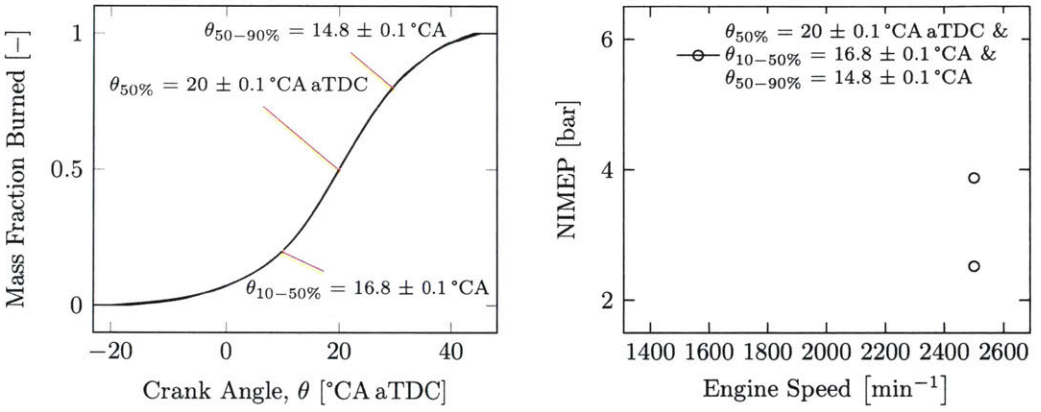

(a) Total of four cycles.

(b) Total of thirty-three cycles.

Figure 8-13: Three-variable parameterization with narrow window (total of 2 points).

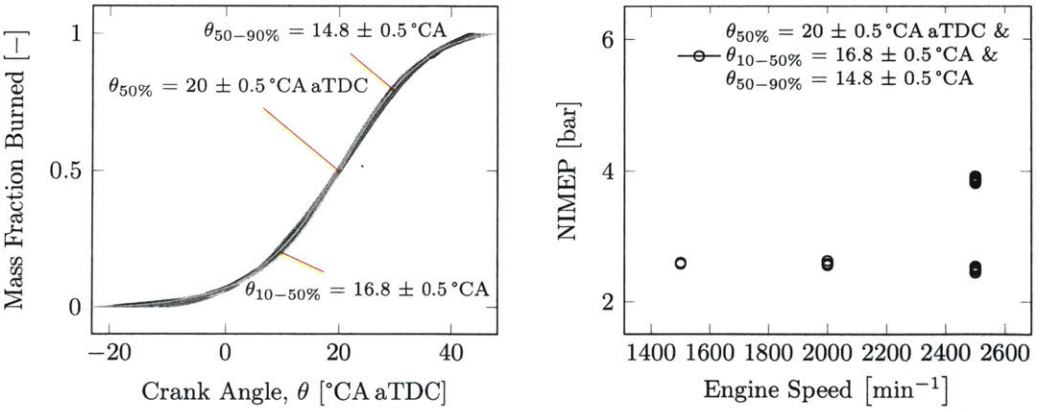

(a) Total of four cycles.

(b) Total of thirty-three cycles.

Figure 8-14: Three-variable parameterization with narrow window (total of 30 points).

Influence of Symmetry Parameter Z

The two- and three-variable parameterization of the heat release schedule derived in the previous section differs by the value of the symmetry parameter Z, that determines the symmetry of cumulative burn fraction around its center point. And hence it is important to understand how the combustion behavior is affected by Z. The range for parameter Z is 0.5 to 2, though most of the forty-one thousand direct-injected cycles have a Z-value between 0.8 and 1.25, compare Figure 8-15 for distribution of the parameter Z.

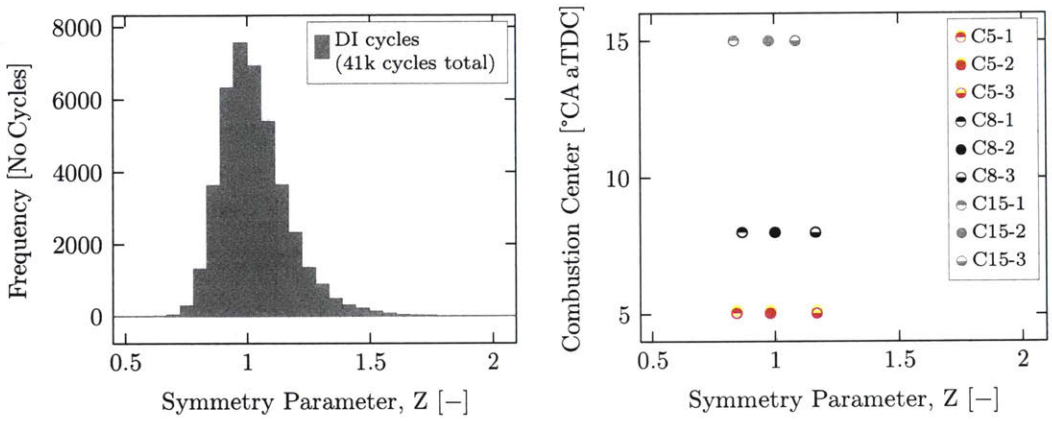

Figure 8-15: The distribution of symmetry parameter Z for the forty-one thousand direct-injected cycles shown on the left. On the right the combustion center for three distinct operating each with low, middle and high value for Z.

Table 8.1: Validation data set of three different operating conditions each with distinct cycles similar in combustion center and rapid burn angle, but with a wide spread in Z.

Cycle -	Speed min^{-1}	NIMEP bar	$\theta_{50\%,nom}$ °CA aTDC	$\theta_{10-90\%,nom}$ °CA	Z -	$\theta_{50\%}$ °CA aTDC	$\theta_{10-90\%}$ °CA
C5-1					0.845	4.953	20.042
C5-2	2500	8.3	5 ± 0.1	20 ± 0.1	0.979	5.020	19.969
C5-3					1.166	4.950	20.041
C8-1					0.869	7.957	19.905
C8-2	2500	8.3	8 ± 0.1	20 ± 0.1	1.000	7.995	20.076
C8-3					1.163	7.993	20.097
C15-1					0.838	15.014	20.063
C15-2	1500	8.1	15 ± 0.1	20 ± 0.1	0.978	15.030	20.072
C15-3					1.085	14.908	20.043

A validation data set of three different operating conditions was chosen, each with

a distinct set of heat release schedules similar in combustion center and rapid burn angle within a small window, but with a wide spread of the symmetry parameter Z, compare Figure 8-15. The operating condition as well as exact values for the parameterization are given in Table 8.1. The measured pressure traces for those cycles, together with the end-gas temperature simulated in GT-Power is shown are shown in Figure 8-16. The symmetry parameter Z does not seem to have a significant influence on in-cylinder pressure and end-gas temperature, as the curves for each operating condition practically lie on top of each other.

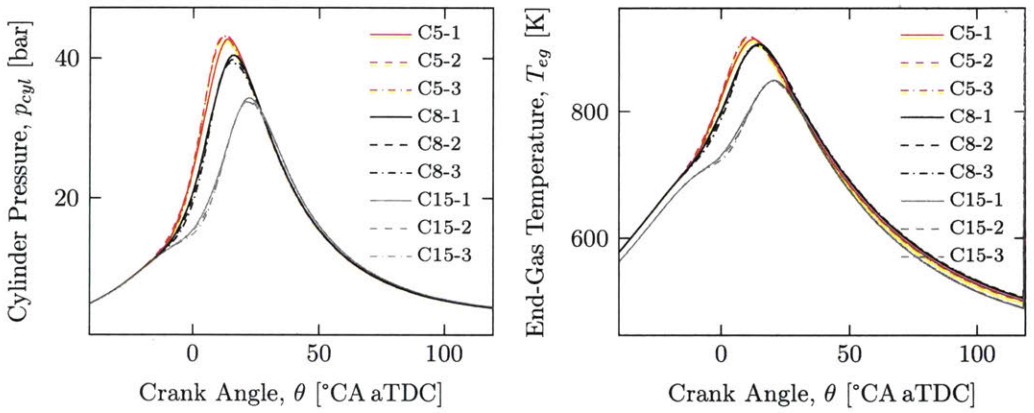

Figure 8-16: Pressure and end-gas temperature traces for the validation data. Each color represents an operating condition with a cycle for each low, medium and high Z value.

The pressure and end-gas temperature are important factors in determination of a knocking cycle, as they determine the likelihood of autoignition in the unburned end-gas. Douaud and Eyzat[18] developed an empirical expression for the ignition delay of the end-gas, which was slightly adjusted to reflect SI-units or their derivatives and is given by,

$$\tau_{DE}(p,T) = 0.01932 \cdot \left(\frac{ON}{100}\right)^{3.4017} \cdot p^{-1.7} \cdot e^{\frac{3800}{T}} \qquad [s] \tag{8.2}$$

Where τ is the ignition delay in seconds as defined by Douaud and Eyzat[18], p is the pressure in bar, T the temperature in K and ON the fuel's octane number. The auto ignition delay can be computed with the Livengood-Wu or autoignition integral[48]

defined by,

$$I_{AI}(t) = \int_{t_0}^{t} \frac{1}{\tau_{DE}(p(t), T(t))} dt \tag{8.3}$$

where t_0 is the time at spark ignition, and τ_{DE} is the ignition delay defined in Equation 8.2. This empirical method predicts autoignition or knock to occur when the autoignition integral reaches a value of one[48]. The time dependent trajectory of the autoignition integral was computed for all the cycles in Table 8.1. While the final value and trajectory of the autoignition integral varies significantly for the different operating conditions, the symmetry parameter Z does not seem to have significant influence, compare Figure 8-17.

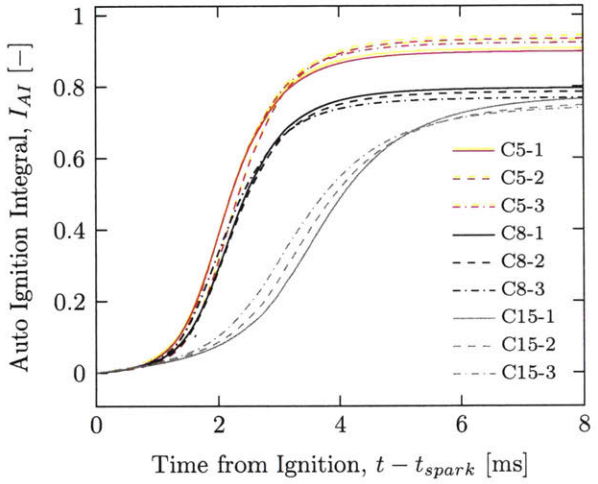

Figure 8-17: Influence of symmetry parameter Z on auto ignition integral.

It can be concluded that for cycles with the same combustion center ($\theta_{50\%}$) and rapid burn angle ($\theta_{10-90\%}$) the symmetry of the heat release schedule around the combustion center, or mathematically the value of symmetry parameter Z has negligible influence on:

- the in-cylinder pressure trace,
- the end-gas temperature,
- and the knock integral trajectory and final value.

Since the influence of Z is negligible on combustion and knock relevant parameters, the simpler parameterization of the heat release schedule with only two variables, combustion center ($\theta_{50\%}$) and rapid burn angle ($\theta_{10-90\%}$) is chosen to be sufficient.

8.2 Mixture Quality

A multi injection strategy was used in combination with the pre-mixing chamber to improve the mixture quality for pre-mixed combustion. The amount of fuel injected was equally split into six injections per cycle, compare Figure 8-18 for the actuator signal of the injector. The reason for that was to mix the fuel better with the non steady air flow to the engine. Furthermore a large U-shaped volume was installed upstream of the engine cylinder head, but downstream from the mixing chamber to dampen out the unsteady flow and to house four fans that further blended the air-fuel mixture.

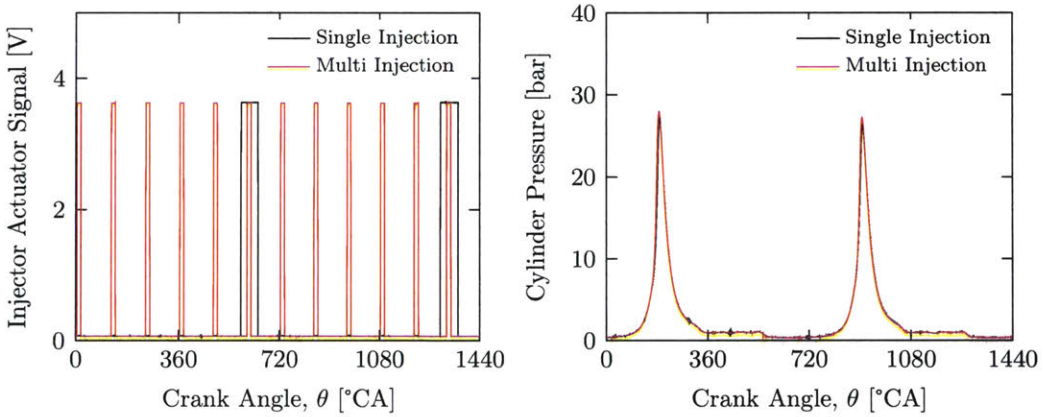

Figure 8-18: The injector actuator signal for the multi-injection strategy with six equal injections per cycle is shown on the left in comparison to a standard single injection strategy. The corresponding pressure traces on the right serve as a reference for the injection timings.

A lambda sweep ($n = 1500\,\mathrm{min}^{-1}, NIMEP = 4\,\mathrm{bar}$) was used to evaluate the mixture quality by measuring the carbon monoxide concentration in the exhaust gas. For direct-injection local inhomogeneities lead to incomplete combustion and there is still a substantial CO concentration in the exhaust gas for an overall lean combustion of lambda equal to 1.05, compare Figure 8-19. For pre-mixed combustion both the

average CO concentration as well as the standard deviation are significantly lower and converge towards a minimum at around 1.04 lambda, that is within the range of error of the analyser indicating the volume fraction of CO is practically zero. Furthermore the standard deviation of the CO concentration falls to almost zero indicating the minimum voltage readout of the analysec, compare Figure 8-20. However, it is important to note that for pre-mixed combustion there remain inhomogeneities for an overall stoichiometric combustion, though the CO concentration is significantly lower compared to direct-injection.

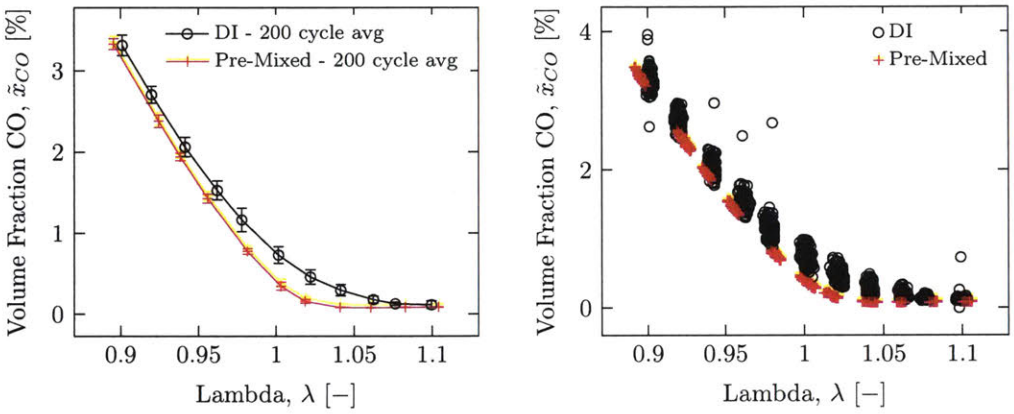

Figure 8-19: The mixture quality is significantly improved in the pre-mixed case as indicated by the lower volume fraction of CO for lean combustion and slightly rich combustion, i.e. $\lambda \geq 0.98$. The volume fraction of CO is slightly lower in the pre-mixed case, even for rich combustion. Average values shown on the left for clarity, and distribution of data points shown on the right.

Eltinge[20] derived a method to determine the air-fuel ratio and distribution from the measured exhaust gas composition. The underlying idea of the detailed method derived can be summarized as such; suppose the mole fraction for each species as a function of the actual and local air-fuel ratio was known, when weighted with the probability density function of lambda, the sum over all possible values of lambda would result in the exhaust gas concentration for the respective species. Assuming the probability density function to be a normal distribution with mean μ and standard

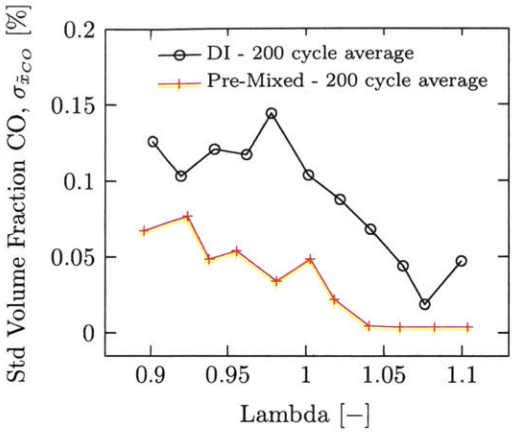

Figure 8-20: The variability or standard deviation of the CO emissions decreases as lambda increases. The overall standard deviation is smaller for direct injection compared to the pre-mixed combustion. For $\lambda > 1.04$ the standard deviation is practically zero as the CO concentration is within the noise of the analyser.

deviation σ, then the theoretical exhaust gas mole fraction for CO is given by,

$$x_{\mathrm{CO}} = \int_0^\infty x_{\mathrm{CO}}(\lambda) \cdot f(\lambda|\mu, \sigma^2)\, d\lambda \tag{8.4}$$

$$f(\lambda|\mu, \sigma^2) = \frac{1}{\sqrt{2\pi\sigma^2}} \cdot e^{-\frac{(x-\mu)^2}{2\sigma^2}} \qquad \text{(Gaussian)}. \tag{8.5}$$

The water-gas shift reaction is used to determine the distribution of CO as a function of lambda ($x_{\mathrm{CO}}(\lambda)$), a simplification that proves quite precise in practice[20].

The exhaust mole fractions computed from the water gas reaction model are depicted in Figure 8-21, next to exhaust CO mole fraction computed by the integral in Equation 8.4 for different mean lambda values as a function of its standard deviation. Experimentally an exhaust gas CO mole fraction of 0.335 % was measured in the lambda sweeps for pre-mixed combustion for a mean lambda value of one, which indicates a standard deviation of 0.0268 in lambda. Figure 8-22 depicts that probability density function, showing that the local mixture deviation from stoichiometry are indeed relatively small.

There is also a noticeable effect on the cycle-to-cycle variation of combustion, compare Figure 8-23. At this low load and speed point the covariance of net indi-

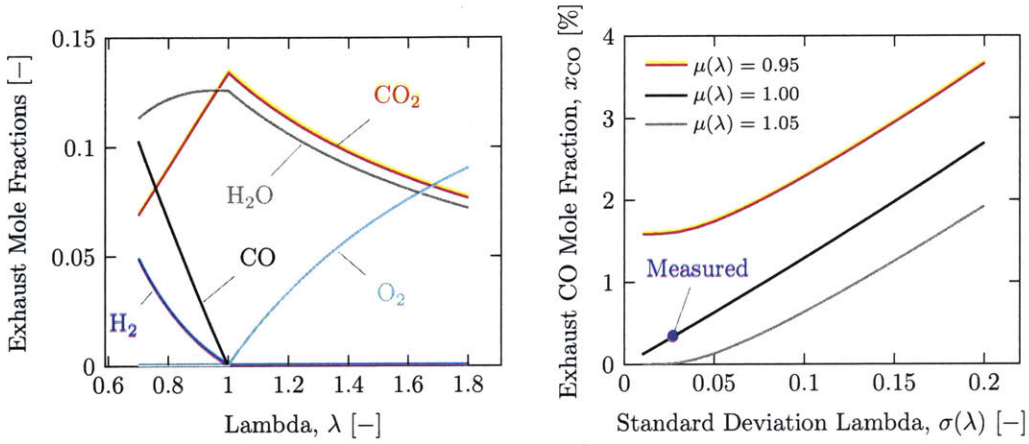

Figure 8-21: Exhaust gas composition as a function of lambda for water gas shift equation. The hydrogen to carbon ratio is equal to 1.887 as per analysis of the test fuel. The water gas shift equilibrium constant is chosen to be 3.5 (from Eltinge[20]).

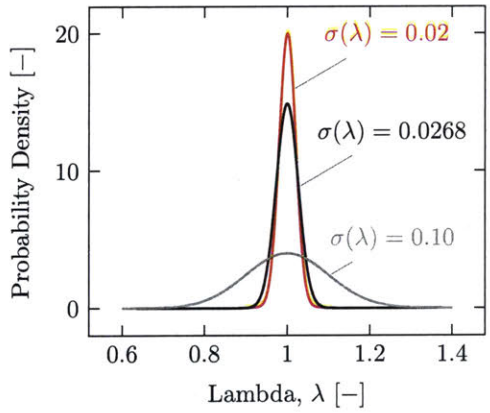

Figure 8-22: Gaussian probability density function as a function of lambda for various standard deviations, all with a mean value of one. The distribution with a standard deviation of 0.0268 depicts the variation of lambda as determined by Eltinge[20]s method for pre-mixed combustion.

cated mean effective pressure is a common measure to determine the variability of combustion as it indicates the vibration level experienced by a driver, which is defined by,

$$COV_{x_i} = \frac{\sigma_{x_i}}{\overline{x_i}} \cdot 100\% \tag{8.6}$$

$$\text{COV}_{NIMEP} = \frac{\sigma_{NIMEP}}{\overline{NIMEP}} \cdot 100\% \tag{8.7}$$

The covariance of net indicated mean effective pressure does not seem to depend much on lambda for combustion with direct-injection, compare Figure 8-23. However, the

covariance of net indicated mean effective pressure of pre-mixed combustion depends strongly on lambda and decreases with increasing lambda by more than thirty percent. While it is only slightly lower compared to the direct-injected case for rich combustion, it increases significantly for lean combustion.

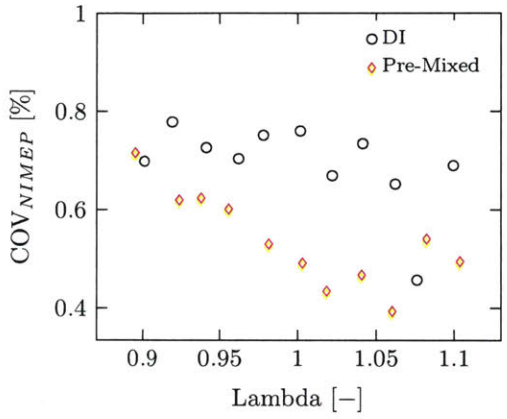

Figure 8-23: The covariance of net indicated mean effective pressure (COV_{NIMEP}) is significantly smaller for pre-mixed combustion compared to the direct injected case.

8.3 Intrinsic Charge Motion Effect

The effect of intrinsic charge motion on cycle-to-cycle variation of combustion will be investigated in the following for combustion phasing associated with normal engine operation. Very late spark timing such as those used in cold start catalyst warm-up strategy is not within the scope. Intrinsic charge motion refers to the charge motion of the baseline flow field created by the tumble motion under normal operating conditions for this specific engine. The parameterization of the heat release schedule will be used as a metric for the influence of intrinsic charge motion on combustion variability. From the two previous sections it can be concluded that:

- A parameterization of the heat release schedule with the two parameters, combustion center ($\theta_{50\%}$) and rapid burn angle ($\theta_{10-90\%}$) allows comparison independent of the load. And hence, it is not sensitive to small fluctuations in fuel delivery and fuel mass trapped in the cylinder prior to combustion.

- The charge is relatively homogeneous for the pre-mixed combustion system with a local standard deviation of approximately 0.0268 in lambda. The influence of air-fuel mixture on cycle-to-cycle variation of combustion is thus deemed to be relatively small.

For premixed combustion, the variability in combustion is hence dependent on charge motion as well as residual-gas fraction and temperature. To single out the intrinsic charge motion effect a *skip fire* experiment was designed. For the skip fire experiment, the only modification to engine operation is that every tenth cycle was not fired ("skipped"). While fuel is injected, the spark plug skips a cycle not firing the charge, resulting in a negative net indicated mean effective pressure for that specific cycle, compare Figure 8-24. The residual gas fraction of the skipped cycle is the one typical for the respective operating condition, while in the following cycle it is diluted by approximately the compression ratio, since the mixture was not burned. As a result the residual gas fraction in the cycle (*Cycle 1*) following the skip fire is very low, in the order of less than one percent.

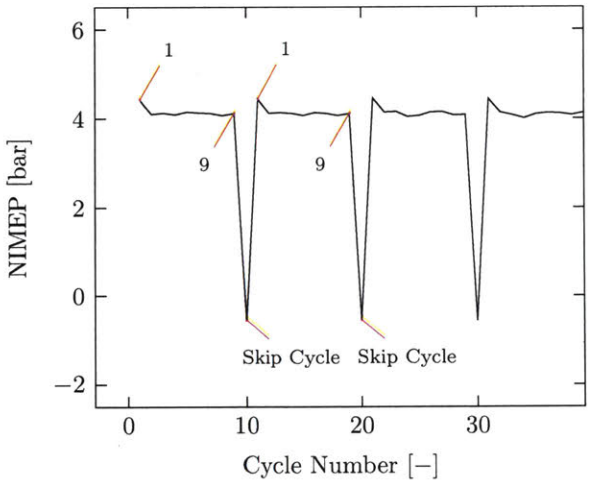

Figure 8-24: During the skip fire experiment the ignition of every tenth cycle is skipped, as indicated by the negative NIMEP. As a result, the following cycle's residual gas is mainly unburned mixture resulting in a very low fraction of burned residuals in the cycle denoted as *Cycle1*. The following cycle's burned residual gas fraction is that one typical for the respective operating condition, these cycles are denoted as *Cycle2-9*.

The main influencing factor for cycle-to-cycle variation in the cycle following the skip fire with pre-mixed combustion is thus due to the intrinsic charge motion, since

air-fuel mixture inhomogeneities and residual gas fraction are negligible. Before analyzing how the intrinsic charge motion effects the variability of combustion it is informative to determine the influences on the position of the combustion center. Not surprisingly, the average combustion center is a linear function of the spark timing, compare Figure 8-29. The slope and intercept may, however, differ by operating condition. For the operating condition shown with an engine speed of 1500 min^{-1} and a nominal net indicated mean effective pressure of 4 bar, there is practically no difference between the low residual case (Cycle1) and the baseline residual case(Cycle2-9).

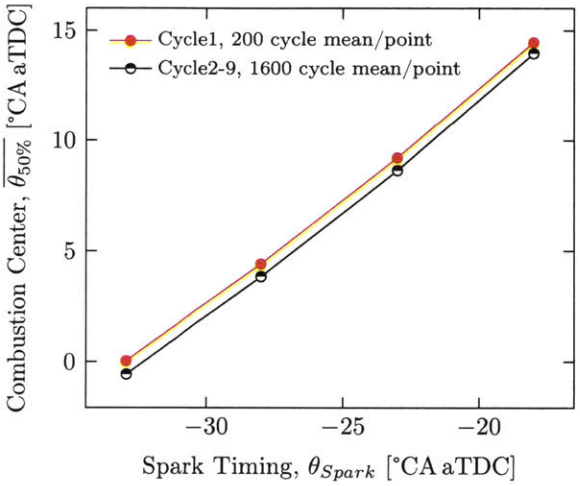

Figure 8-25: The average combustion center is a linear function of the spark timing. The range of the combustion center for a specific spark timing is approximately ±6 °CA due to cycle-to-cycle variations. The difference of residual gas between the skipped and normal cycles is negligible for this operating condition with $n = 1500\,\mathrm{min}^{-1}$ and $NIMEP = 4\,\mathrm{bar}$.

There is a relatively small number of spark timings for the spark sweep in Figure 8-29 each with a relatively large spread in combustion center. A more detailed understanding of the relationship between spark timing and combustion center can be obtained if the data is binned and averaged by combustion center. A bin width of 1 °CA is chosen, compare Figure 8-30. The relationship is again linear and there is no significant difference between the low residual and baseline residual cycle, compare Figure 8-26. The curve flattens out towards the extreme spark timings, since no spark timings are observed beyond this bounds so that the length of the of the flat curve indicates the range of combustion center observed for that particular spark timing.

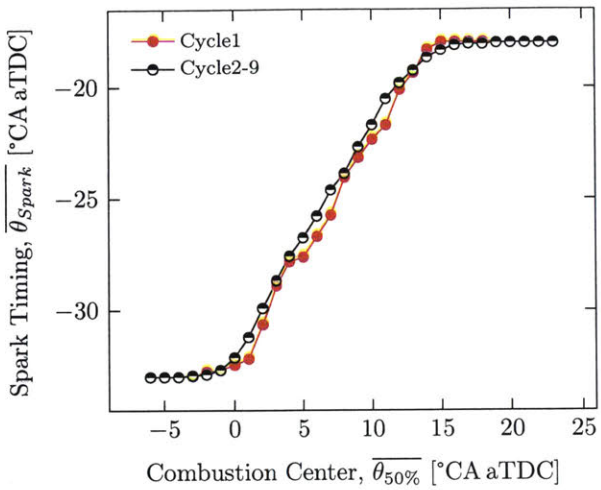

Figure 8-26: The relationship between the spark timing and the combustion center is linear. The plot shows the average spark timing calculated from values binned by combustion center with a window width of 1 °CA according to the binning process shown in Figure 8-30. The curve flattens out towards the sides at the extreme values of spark timing investigated. The flat part is hence a measure of the variation due to cycle-to-cycle variation.

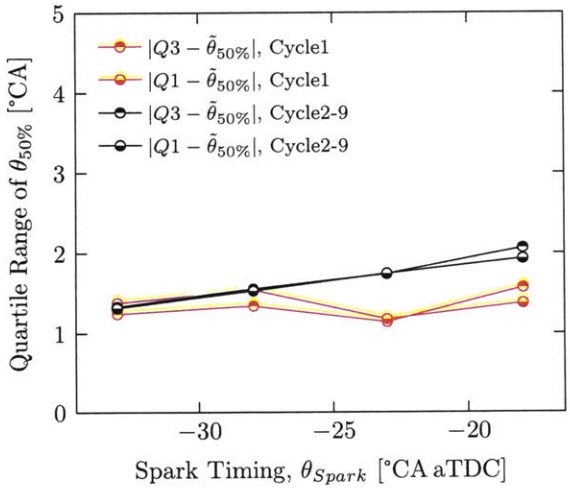

Figure 8-27: The distance between the 25 % quantile ($Q1$) and the median is approximately the same as between the 75 % quantile and the mean, indicating a symmetric distribution.

While it is important to note that the relationship between combustion center and spark timing is linear for the engine operation, the variability of the combustion center for a specific spark timing is what will effect the cycle-to-cycle variation of combustion. Comparing distributions or functions for a large number of data sets can be tedious, as there is no obvious metric on how to quantify the difference between two shapes. It is therefore useful to find a meaningful scalar that can quantitatively

describe the distributions to compare them. The data shows that the distribution of the combustion center for a given spark timing is relatively symmetric, because the distance between the 25 % quantile ($Q1$) and the median is approximately the same as between the 75 % quantile and the mean, compare Figure 8-27.

Another measure for the symmetry of a distribution is the skewness s, which is defined by

$$s(x) \equiv \frac{E(x-\mu)^3}{\sigma^3} \tag{8.8}$$

where μ is the mean of x, σ the standard deviation of x, and $E(t)$ the expected value of quantity t. The bias corrected skewness (s_0) a Matlab standard function that is used here to evaluate the data is given by,

$$s_0 = \frac{\sqrt{n(n-1)}}{n-2} \cdot s_1, \text{with} \tag{8.9}$$

$$s_1 = \frac{\frac{1}{n}\sum_{i=1}^{n}(x_i - \overline{x})^3}{\left(\sqrt{\frac{1}{n}\sum_{i=1}^{n}(x_i - \overline{x})^2}\right)^3} \tag{8.10}$$

Skewness values of one or greater indicate that the distribution is in fact skewed in a direction depending on its sign, whereas values below one indicate that the distribution is relatively symmetric. The skewness of the combustion center as a function of spark timing is computed in Figure 8-28. All absolute skewness values are well below 0.5 confirming that the distribution is in fact relatively symmetric. Henceforth the standard deviation will be used as a single scalar to quantify the shape of the distribution.

The standard deviation of the combustion center appears to be almost independent of the spark timing, compare Figure 8-29. It appears to be almost constant at a value of approximately two for this operating point with an engine speed of $1500\,\mathrm{min}^{-1}$ and a nominal NIMEP of 4 bar. This agrees well with the observed range of $\pm 6\,^{\circ}\mathrm{CA}$, which is ± 3 standard deviations. Additionally there is little difference in the standard deviation for the low residual cycle (Cycle1) and the baseline residual cycles (Cycle2-9).

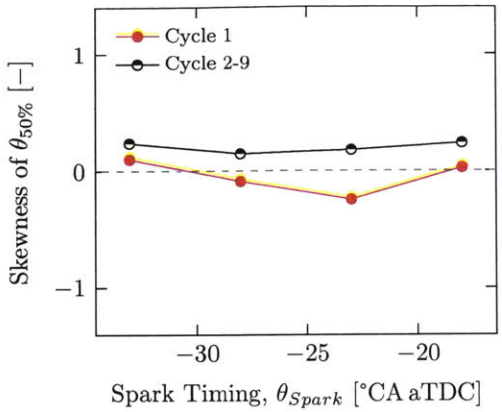

Figure 8-28: Skewness of the combustion center distribution as a function of spark timing. Values below one indicate that the distribution is relatively symmetric.

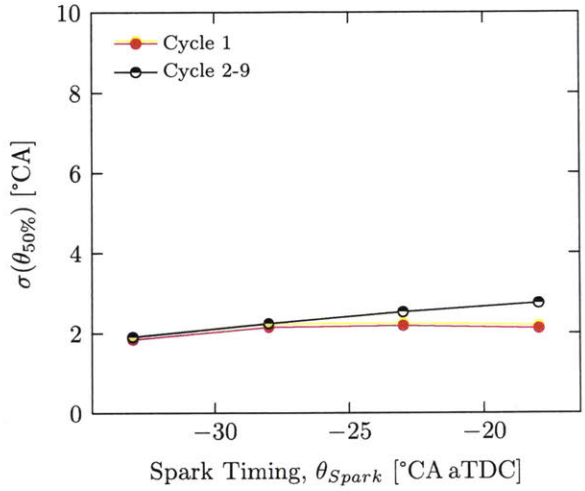

Figure 8-29: Standard deviation of the center of combustion as a function of spark timing.

It can hence be concluded for the combustion center that:

- Any average $\theta_{50\%}$ can be achieved by varying the spark timing accordingly.
- For a given spark timing, the distribution of the combustion center around its average value is symmetric and can be described by its standard deviation
- The value of the standard deviation or the spread in the distribution does not seem to depend on the spark timing and is approximately a constant for a given operating condition.
- There seems to be no significant difference in the standard deviation of the

combustion center for the skipped cycle with low residuals (in the order of less than one percent), compared to the cycles with baseline residuals approximately ten times as high.

So far only the combustion center ($\theta_{50\%}$) has been investigated, in a next step the rapid burn angle ($\theta_{10-90\%}$) is investigated to quantify the total variability of the heat release schedule. To connect the two variables, the variability of the rapid burn angle as a function of combustion center will be investigated, using conditional statistics. That means that the rapid burn angle is binned by its respective combustion center and that mean and standard deviation quantities are computed for each bin.

An arbitrary bin width is chosen for the binning process. Here, the bin width is equal to 1 °CA for good resolution, while at the same time guarantying a reasonably large sample size per bin. Each binning interval is centered around an integer value and includes the left boundary of the interval, which can formally be expressed as,

$$[a_i, a_{i+1}) = \{\theta_{50\%} \in \mathbf{R} \mid a_i \leq \theta_{50\%} < a_{i+1}\} \qquad \text{with,} \tag{8.11}$$

$$a_{i+1} - a_i = 1 \tag{8.12}$$

$$\frac{a_{i+1} - a_i}{2} = k \qquad (k = \text{integer}) \tag{8.13}$$

A graphical interpretation is given in Figure 8-30, where the mean for a large sample size of each bin is computed. Binned quantities are only computed for a minimum sample size of twenty data points, while the typical sample size is significantly larger.

The average rapid burn angle is increasing exponentially with combustion center phasing for the baseline operating condition with an engine speed of 1500 min^{-1} and a nominal NIMEP of 4 bar, compare Figure 8-31. There seems to be negligible difference between the low residual cycles (Cycle1) and the baseline residual cycles (Cycle2-9).

The standard deviation of the rapid burn angle does not seem to depend on the phasing of the combustion center for the baseline residual case of the baseline operating condition, compare Figure 8-32. While the standard deviation fluctuates more in the low residual case, it does so around a constant average value independent of combustion center. The higher volatility might be caused by the significantly lower

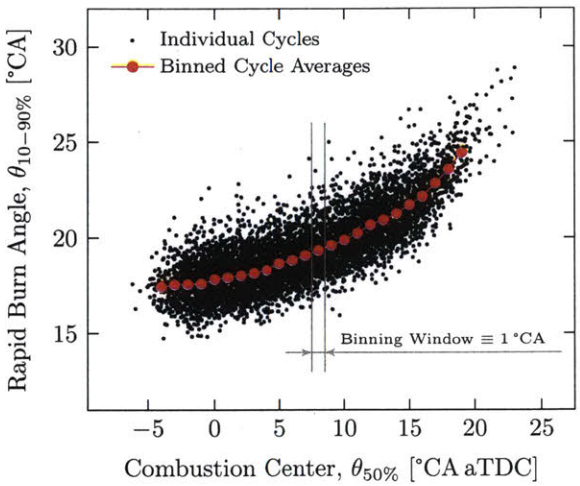

Figure 8-30: Rapid burn angle data is grouped and averaged in bins with a width of 1 °CA according to its combustion center. Averages are only computed for a minimum group size of twenty data points per bin.

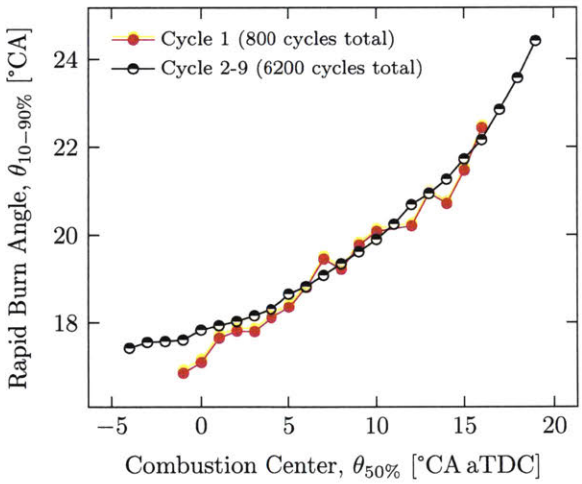

Figure 8-31: The average rapid burning angle increases exponentially with combustion center. Spark sweep for a single operating condition is shown, for an engine speed of 1500 min^{-1} and nominal load of 4 bar net indicated mean effective pressure.

sample size in the low residual case. In general no significant difference between the low and the baseline residual cases could be observed.

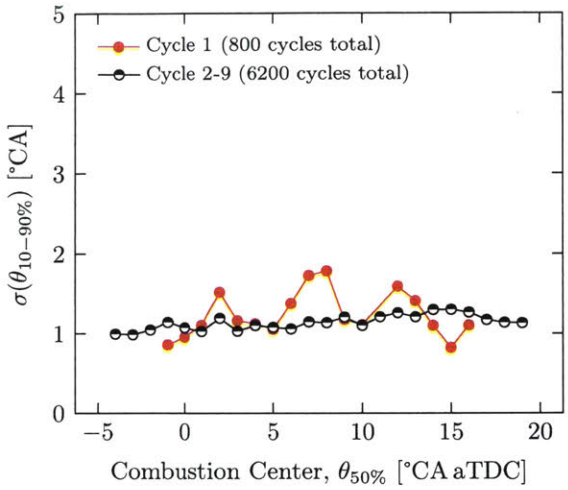

Figure 8-32: The standard deviation of the rapid burn angle appears to be independent of combustion center phasing with an approximately constant value of 1 °CA for the baseline residuals case.

Cycle-to-Cycle Variation of Combustion for Baseline Charge Motion

After quantifying average and standard deviation of the parameterization of the heat release schedule for the baseline case a physical interpretation and discussion of those results is necessary for a complete understanding and to derive a broader validity. First a physical explanation for the relationship between the rapid burn angle and the combustion center will be derived. A quadratic fit approximates the relationship between those parameters well, indicating that the overall combustion duration increases more and more as the combustion center is phased further past the top dead center, compare left plot in Figure 8-33.

At the same time the cylinder volume increases exponentially with crank angle after top dead center, due to the non-linear link between crank shaft and piston. It appears that the expansion due to increasing volume with later crank angle slows the overall combustion rate in crank angle and hence results in longer rapid burn angles. A linear fit correlates the average rapid burn angle with the cylinder volume extremely well with an almost perfect coefficient of determination ($R^2 = 0.992$). This could indicate that the total cylinder volume is the major influencing factor on the

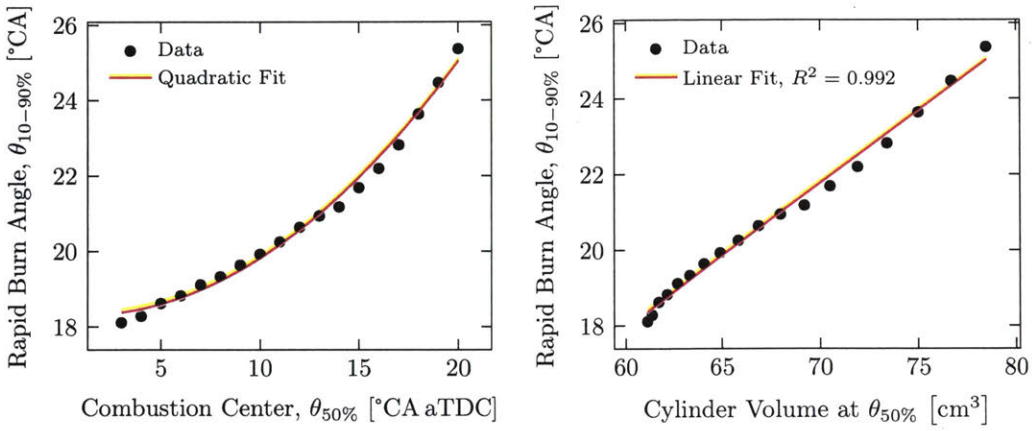

Figure 8-33: The rapid burn angle as a function of combustion center can be approximated by a quadratic function that increases with increased combustion phasing (left). When plotted against the cylinder volume at combustion center the data becomes linear with a coefficient of determination $R^2 = 0.992$, indicating a strong influence of the total cylinder volume on the burn duration.

burn duration of the charge, and that the expansion effect is through temperature and pressure.

Given that the heat release schedule can be fully parameterized by only two parameters ($\theta_{50\%}$, and $\theta_{10-90\%}$) the cycle-to-cycle variation of combustion can be explained by the mean value and standard deviation of these parameters only. Results from the previous sections have shown, that any average combustion center can be obtained by varying the spark timing accordingly. The standard deviation of the combustion center is not a function of spark timing, but is approximately constant and its value depending on operating condition. Similarly, the standard deviation in rapid burn angle does not seem to depend on the combustion phasing and is approximately constant for a given operating condition. Furthermore, there is an exponential relationship between the average rapid burn angle and average combustion center that is intrinsic in nature due to the piston motion, though the vertical position depends on the operating condition.

Taken these observations into account one can derive a simple geometric interpretation of the cycle-to-cycle variation of combustion. Considering a two-dimensional plane with an abscissa for the center of combustion and the ordinate for the rapid burn angle. Then for a given operating point, the average rapid burn angle for an

arbitrarily chosen average center of combustion is explicitly defined, such a pair of values is denoted with μ_1 in Figure 8-34. And 99.7 % of all cycles for this operating condition will be in an area within three standard deviations for each the combustion center and the rapid burn angle, which are roughly constant for a given operating condition. Given that the overall CCV of combustion is of stochastic nature and not dependent on the previous cycle, then the largest distance between any two points in the area enclosed is proportional to the CCV of combustion. This is illustrated by the distance denoted $\overline{AB}$ in Figure 8-34 for an average combustion phasing and duration of μ_1. Due to curvature of the relationship between the average quantities, this distance increases for larger values of the combustion center even if the standard deviations for both phasing and rapid burn angle remain the same.

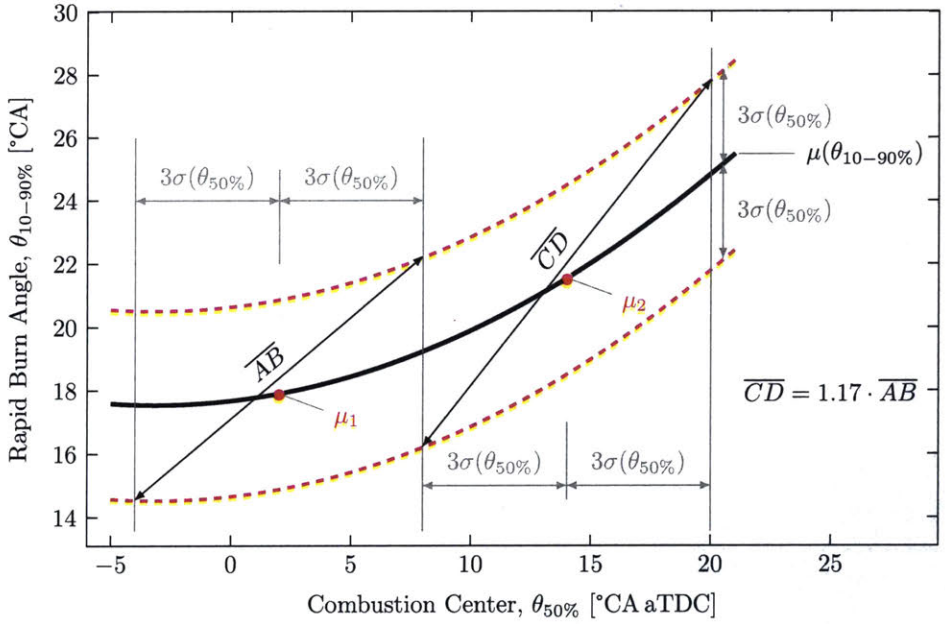

Figure 8-34: For an average operating condition $\mu_1 = (\overline{\theta}_{50\%}, \overline{\theta}_{10-90\%})$, 99.7 % of cycles will be in the area enclosed by three standard deviations in each direction, which is proportional to the entire probability space. Assuming a constant standard deviation and a parabolic function of the average rapid burn angle with respect to the average combustion center, then the size of the probability space will increase with increasing combustion center. Assuming there is no pattern or relationship from one cycle to another, then the largest distance within the probability space is proportional to the largest variability. The longest distance for the area with an average combustion center of 2 °CA aTDC is 14.24 °CA, whereas it is 16.7 °CA for an average combustion center of 14 °CA aTDC or 17.26 % longer.

To support the argument instead of binning the data, the standard deviation of

the rapid burn angle was computed as a function of the average combustion center for each nominal constant operating condition of a spark sweep, compare Figure 8-35. There is an increasing trend for larger average combustion centers, indicating that indeed the variability observed for a nominal constant operating condition increases with its average combustion center.

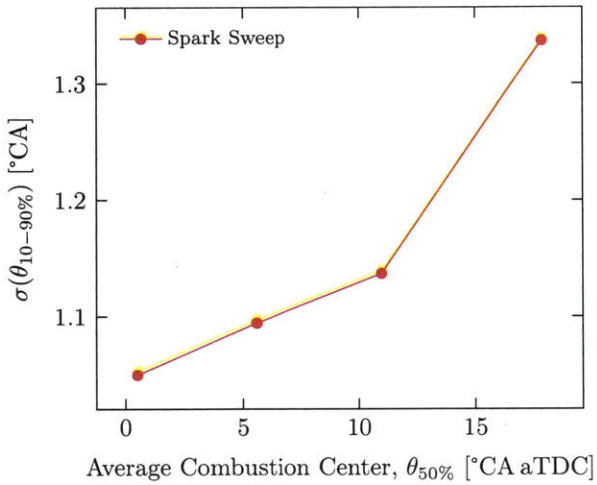

Figure 8-35: Increasing trend in the variation of the rapid burn angle for nominal constant operating condition of a spark sweep with increasing average combustion center.

From this simple geometric interpretation it is obvious that under the validity of the previous results, there are only three parameters determining the magnitude of the cycle-to-cycle variation of combustion:

- The relationship between the average quantities of combustion parameters, i.e. $\overline{\theta}_{10-90\%} = f(\overline{\theta}_{50\%})$ (combustion phasing effect)
- The standard deviation of the combustion center, $\sigma(\theta_{50\%})$ (combustion characteristic)
- The standard deviation of the rapid burn angle, $\sigma(\theta_{10-90\%})$ (combustion characteristic)

The influence of operating parameters, engine speed, load, residual gas fraction, and increased charge motion on the aforementioned parameters will be investigated in the following.

Influence of Load and Speed on Combustion Variability

Engine speeds of 1500 min^{-1} , 2000 min^{-1}, and 2500 min^{-1} were investigated, as well as nominal engine loads of 4 bar, 6 bar, and 8 bar net indicated mean effective pressure . The engine speed appears to hardly influence the variability of the combustion, whereas an increase in load reduces the variability of the combustion center, compare Figure 8-36. The variability of the combustion center, however, is not sensitive to the combustion phasing. The data was obtained with spark sweeps, and nominal load depicts the engine load at MBT. Since the amount of fuel injected as well as the air-fuel ratio was kept constant for a given nominal operating condition the actual load decreases slightly for spark advance and retard. Furthermore only the cycles with baseline residual mass fraction (Cycle2-9) from the skipfire experiment are shown since the difference between the skipped cycle (*Cycle1*) and the baseline residual cycles is negligible. And hence, only Cycle2-9 are shown due to larger sample size and for clarity.

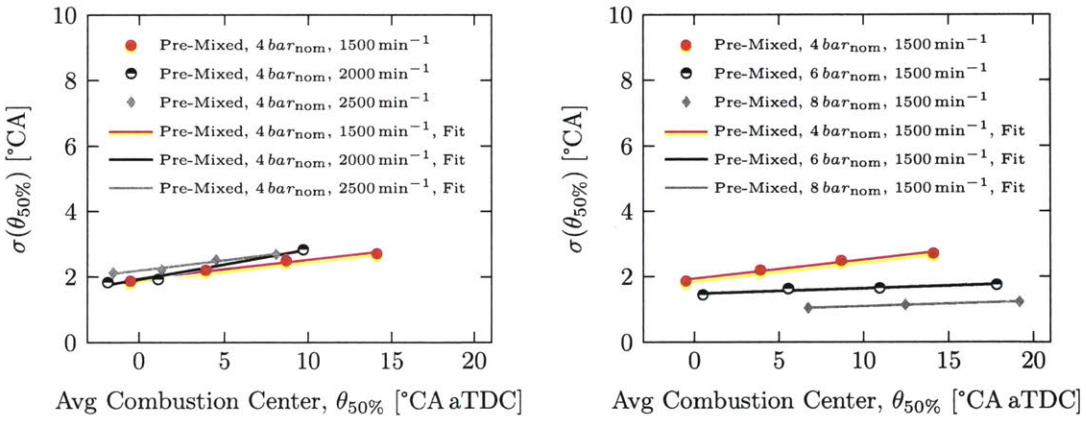

Figure 8-36: Influence of engine speed (left) and engine load (right) on the variability of the combustion center for premixed combustion.

The average combustion center refers to the average for a given spark timing, and is only shown instead of the spark timing itself as it differs significantly from one operating condition to another. Windowing the data when computing the standard deviation of a variable on itself does not make much sense mathematically.

An increase in engine speed appears to shift the curve describing the relationship

between the rapid burn angle and combustion center towards longer burn durations in the crank angle domain, though it doesn't seem to alter the shape of the curve significantly, compare Figure 8-37. Around the MBT combustion phasing the shift per 500 min^{-1} increment of engine speed appears to be approximately constant. The effect of engine load appears to be the opposite, as the curve shifts towards shorter burn durations with increasing engine loads. The data was binned by combustion center with a window width of 1 °CA before computing the averages.

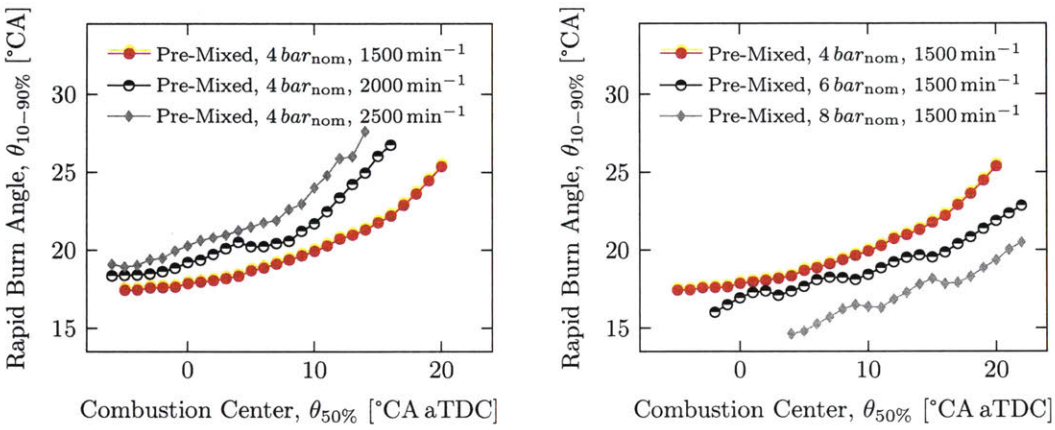

Figure 8-37: Influence of engine speed (left) and engine load (right) on the relationship between rapid burn angle and combustion center for premixed combustion. Data binned by combustion center with a window width of 1 °CA.

The 10 % to 90 % burn time (τ) scales with the rapid burn angle and engine speed by the following correlation,

$$\tau \propto \frac{1}{N^{\alpha}}, \quad \text{and hence} \tag{8.14}$$

$$\theta_{10-90\%} \propto N \cdot \tau \propto \frac{N}{N^{\alpha}} \propto N^{(1-\alpha)} \tag{8.15}$$

where N is the engine speed and α is a constant. The data scales relatively well for different engine speeds and early combustion center, when a value of α equal to 0.725 is assumed, compare Figure 8-38. The difference for retarded combustion could be explained by the further effect of turbulence decay which is detrimental to burn rate for later combustion. The amount of decay is time dependent, and the decay is more severe at low speed. Thus for the retarded combustion ($\theta_{50\%} > 10$ °CA aTDC), the

left plot in Figure 8-38 over-corrects the engine speed N effect. The data does not scale well with load though.

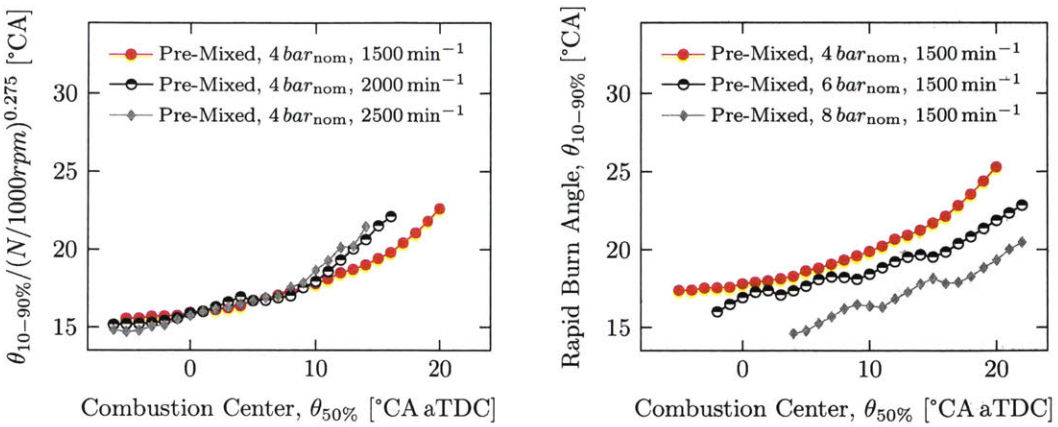

Figure 8-38: Rapid burn angle scales with engine speed for combustion centers below 10 °CA aTDC (left). Deviation for retarded combustion could be explained by turbulence decay.

The rapid burn angle is determined by combustion in the turbulent regime; thus the laminar flame speed (which, as a function of temperature and pressure, would be sensitive to load) does not play a role. The burn rate is limited by u', the turbulent velocity fluctuation. The value of u' is determined by the intake kinematic, and is not sensitive to load. However, the specific kinetic energy $\rho u'^2$ increases with load. The burn rate depends on u' at the time of burning. Hence, there is a dependence on load, which determines how much turbulent kinetic energy is left by the time of burning. Since the influence on u' is indirect (through heat transfer; see below), the burn rate is much less sensitive to load.

More quantitatively, let ρ_0 and u'_0 be the density and turbulent velocity at induction. Note that u'_0 is governed by kinematics, and is only a function of piston speed, and not load. At the time of combustion, the density and turbulent velocity are ρ and u'. If the turbulence decay factor is ξ, which is insensitive to load (the dependence is through the kinematic viscosity μ), u' is given by,

$$u' = \sqrt{\frac{\rho_0 u_0'^2 \xi}{\rho}} \tag{8.16}$$

The unburned gas state may be approximated by isentropic compression from the

end of the intake process; thus

$$u' = \left(\frac{p}{p_0}\right)^{\frac{1}{\gamma}} \cdot \sqrt{u_0'^2 \xi} \tag{8.17}$$

If there was no heat transfer p/p_0 would be independent of load. With heat transfer, p/p_0 increases with load, but the dependence is weak.

Lastly, the engine speed increases the variability of the rapid burn angle, which in itself increases slightly with increasing combustion center, compare Figure 8-39. Increasing engine load decreases the variability of the rapid burn angle, which in this case does not seem to depend on the combustion center.

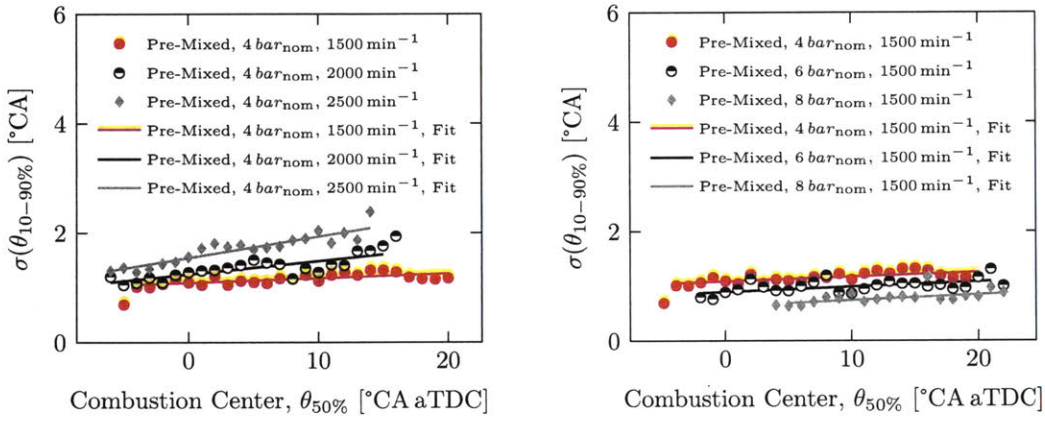

Figure 8-39: Influence of engine speed (left) and engine load (right) on the variability of the rapid burn angle for premixed combustion. Data binned by combustion center with a window width of 1 °CA.

In conclusion an increase in engine speed at constant load increases the cycle-to-cycle variation of combustion, whereas an increase in load decreases the CCV of combustion. Additionally the influence of the load is more dominant, as it affects variability of both combustion center and rapid burn angle, whereas the change in engine speed merely influences the variability of the rapid burn angle. However, the change of all quantities effected by a variation of speed and load appears to be approximately proportional to the change in the respective parameter.

8.4 Increased Residual Gas Effect

The influence of the residual gas fraction on cycle-to-cycle variation of combustion will be investigated in this section. The results from the skipfire experiment in Section 8.3 have shown that for the operating conditions investigated a reduction in the residual gas mass fraction by approximately 90 % to an absolute residual gas mass fractions in the order of 1 % had little influence on the combustion. However, the absolute residual gas mass fraction was moderate with less than 10 % for the low load operating condition. To investigate a larger mass fraction of residual gases valve sweeps were performed to increase the fraction of internal exhaust gas recirculation. The mass fraction of residuals as a function of valve overlap for different loads was simulated in GT-Power and is depicted in Figure 8-40. The exhaust valve closing valve timing was kept constant and the intake valve timing was swept to vary the valve overlap. The mass fraction of residual gases increases for all load conditions with increasing valve overlap and is generally lower for higher loads.

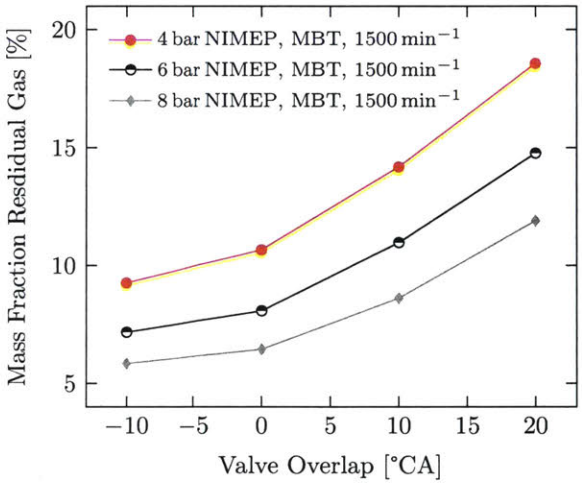

Figure 8-40: Residual gas mass fraction as simulated in GT-Power for for different valve overlap and loads at constant engine speed. The exhaust valve timing is kept constant at $EVC = -10\,°\text{CA}$ aTDC. The nominal net indicated mean effective pressure depicted in the graph is for maximum brake torque spark timing and the base valve timing of $-10\,°\text{CA}$ valve overlap.

For this experiment only the valve timing was swept and no spark sweep was done, and hence the variation of the combustion center as a function of spark timing consists of only one data point. However, binning the data by combustion center shows that

increasing the residual gas fraction up to 18.6 % seems to only slightly influence the variability of the rapid burn angle, compare Figure 8-41. An explanation for this could be that dilution fundamentally slows the laminar burning speed, as the overall burning speeds in this engine are relatively fast (in the order of 20 °CA) the turbulent flame speed might be dominant reducing the importance of the laminar flame speed. And hence the rapid burn angle would only be slightly longer, thus the increased residuals do not appear to influence the relationship between the average rapid burn angle and average combustion center much.

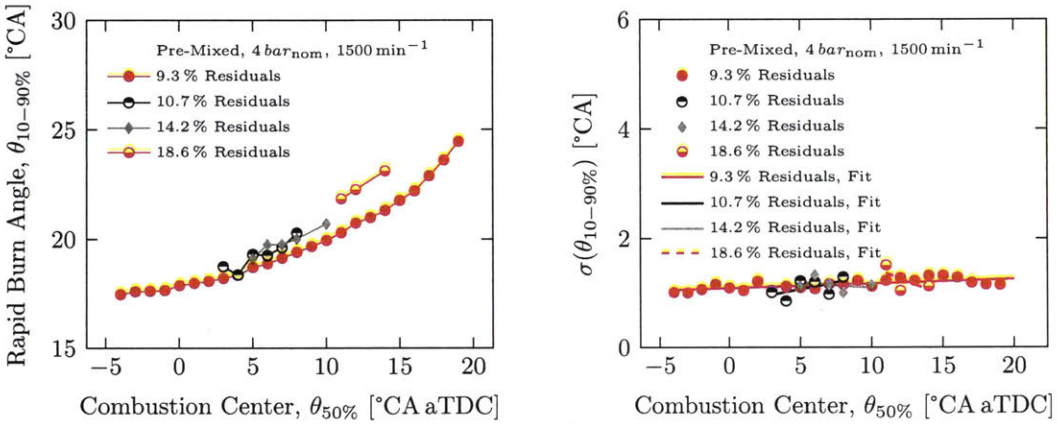

Figure 8-41: Rapid burning angle (left), and variability of rapid burn angle (right) as a function of combustion center. Data for increased residuals from valve timing sweep is shown for a single spark timing, at an engine speed of 1500 min^{-1} and nominal load of 4 bar net indicated mean effective pressure.

8.5 GDI Effect

In this section the influence of direct-injection versus premixed combustion on cycle-to-cycle variation will be investigated, subsequently the influence of load and speed on the CCV for direct-injection. All direct-injection data was recorded with a start of injection (SOI) at 50 °CA aTDC, and an injection pressure of 200 bar.

GDI compared to Pre-Mixed Combustion

The relationship between the average combustion center and spark timing is approximately linear for direct-injection. though compared to premixed combustion it is shifted slightly towards later combustion center, compare Figure 8-42. In other words the spark timing needs to be advanced slightly with direct-injection for the same average combustion center as with premixed combustion. There seems to be no difference in the variability of the combustion center between premixed combustion and direct-injection.

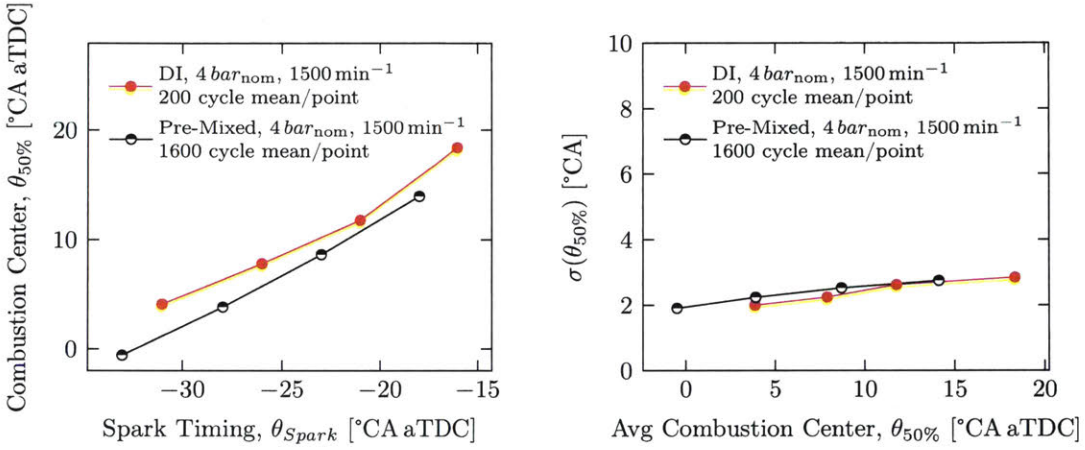

Figure 8-42: Comparison between premixed combustion and direct-injection. Influence of spark timing on average combustion center (left) and influence of average combustion center on its variability (right).

The relationship between the average combustion center and rapid burn angle is rather similar for direct-injection and premixed combustion, compare Figure 8-43. However, the variability of the rapid burn angle seems to be significantly larger for direct-injection as compared to premixed combustion. This could be due to stochastically appearing local inhomogeneities that influence the combustion duration of the diffusion flame.

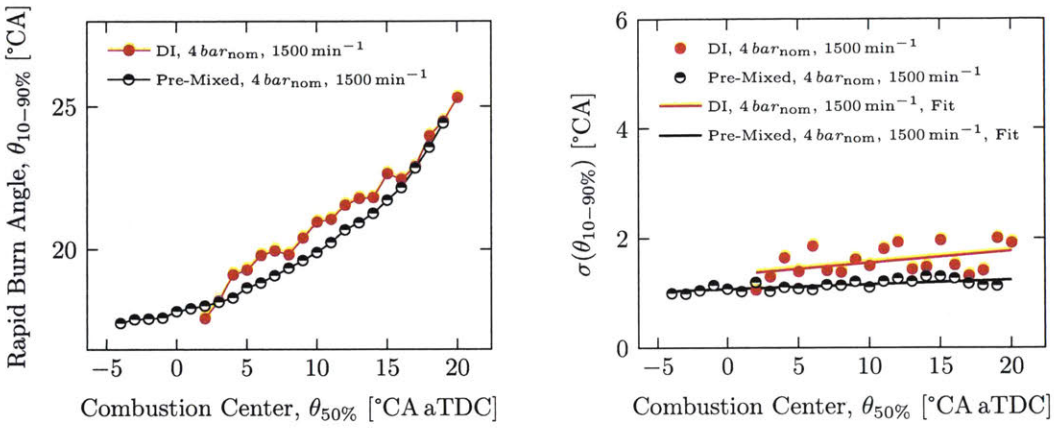

Figure 8-43: Relationship between average rapid burn angle and average combustion center for direct-injection and premixed combustion (left). The variability of the rapid burn angle increases for direct-injection compared to premixed combustion (right).

Influence of load and speed on CCV with GDI

There seems to be no strong influence of neither engine speed nor load on the variability of the combustion center, compare Figure 8-44. Furthermore variability of the combustion center appears to be little sensitive to the combustion phasing.

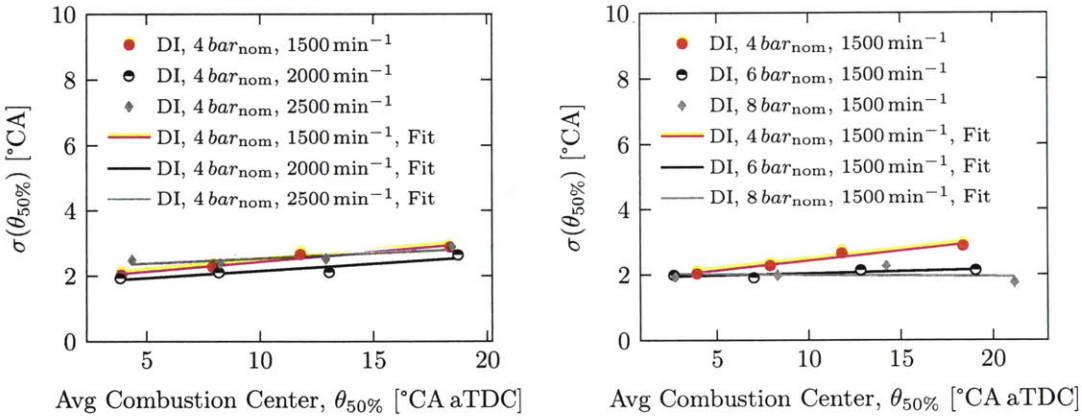

Figure 8-44: Variability of combustion center for different engine speeds (left) and loads (right) for direct-injection.

The rapid burn angle increases with engine speed, while it decreases with engine load, compare Figure 8-45. The trend is similar to the trend observed for premixed combustion.

The engine speed, however, seems to have little influence on the variability of the

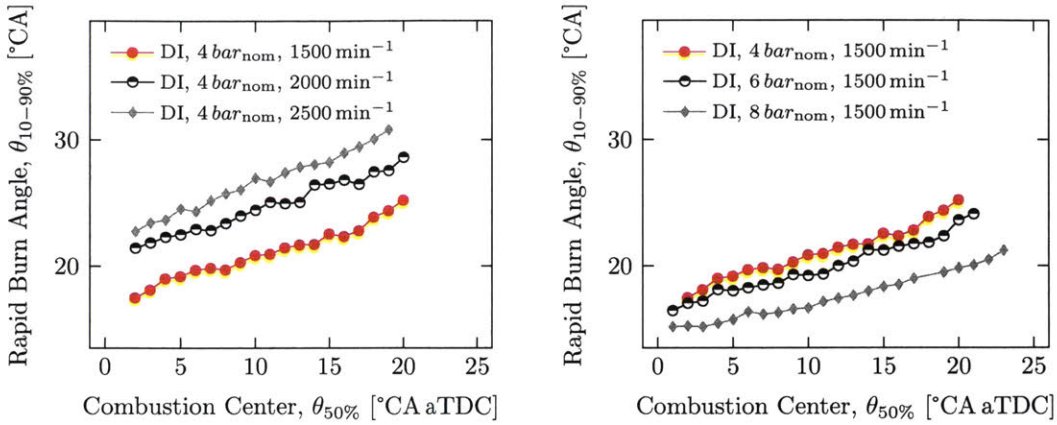

Figure 8-45: Relationship between rapid burn angle and combustion center for different engine speeds (left) and engine loads (right). The general trend is similar to the case with premixed combustion.

rapid burn angle, compare Figure 8-46. Whereas increasing engine load reduces the variability of the rapid burn angle in analogy to the premixed case.

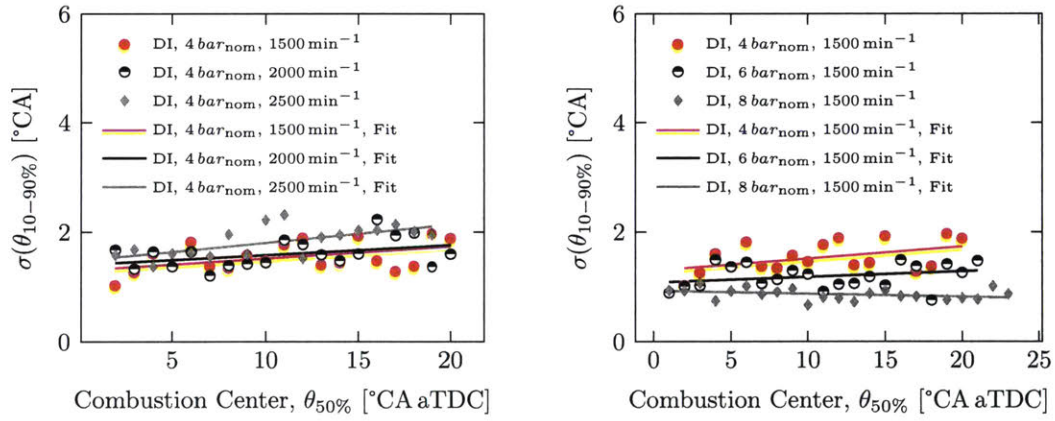

Figure 8-46: Influence of engine speed (left) and engine load (right) on the variability of the rapid burn angle for direct injection. While the engine speed appears to have little influence on the variability, it is reduced significantly for increasing engine load.

In conclusion the following was observed for non-knocking combustion with the LTG engine, over a load interval of 4 bar to 8 bar, and an engine speed interval of 1500 min^{-1} to 2500 min^{-1}.

- The heat release schedule can be parameterized reasonably well with two parameters only:
  - the combustion center ($\theta_{50\%}$),

  - and the rapid burn angle ($\theta_{10-90\%}$).

- And hence the CCV of combustion can be characterized by those two parameters only.

- An exponentially increasing relationship between the rapid burn angle and the combustion center inherently leads to an increase in CCV for larger values of the combustion center, which is purely a combustion phasing effect

- For premixed combustion:

  - the engine speed increases the variability of the rapid burn angle, but not of the combustion center

  - the engine load reduces the variability of the rapid burn angle, and of the combustion center

  - Residuals from approximately 1 % to 20 % mass fraction do not appear to influence the combustion variability significantly.

- The variability of the rapid burn angle is significantly larger for combustion with direct-injection compared to premixed combustion.

- Furthermore for direct-injection,

  - engine load and speed hardly influence the variability of the combustion center,

  - an increase in engine speed increases the variability of the rapid burn angle only slightly.

  - And an increase in engine load decreases the variability of the rapid burn angle.

8.6 Increased Charge Motion - Insert

The charge motion was increased significantly with an intake port insert, reducing the port's cross-sectional area to 30 % of its original value. The resulting change of

tumble motion was measured on a flow bench by GM resulting in an increased tumble index over the entire valve lift period, compare Figure 8-47. The setup used is similar to the one described by Halsall et al.[24]. The tumble index was normalized by the largest value of the baseline case to allow for comparison, as the absolute values would depend on the flow bench and sensor setup.

The tumble intensity with the insert is on average 77 % larger compared to the baseline case. At the same time, however, the air mass flow into the engine is largely reduced due to the flow restriction. For the same manifold air pressure the mass flow rate over the entire valve lift is reduced by $50\,\mathrm{g\,s^{-1}}$ on average, requiring an increase in manifold air pressure for the same mass trapped at intake valve closing. At part load this can be achieved by de-throttling, however, at full load to boosted operation it requires increased boost pressure that may not be available.

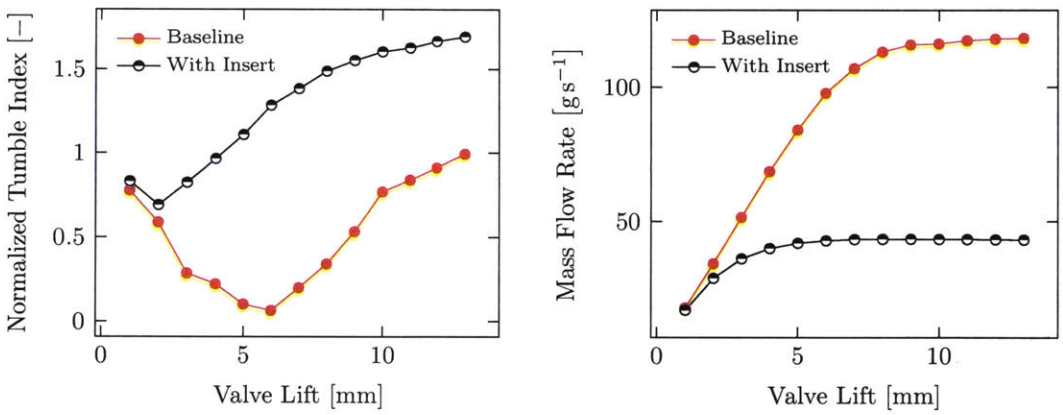

Figure 8-47: The increase in tumble index with insert compared to the baseline configuration (left), and the decrease in mass flow for constant manifold air pressure as a function of valve lift (right). Tumble index is normalized by largest tumble value of baseline case.

The insert reduces the variability of the combustion center significantly by up to 50 % compared to the baseline configuration, equally affecting direct-injection and premixed combustion.

The insert reduces the rapid burn angle significantly as it is shifted towards shorter burn durations by up to 5 °CA for both direct-injection and premixed combustion, compare Figure 8-49. Also the variability of the rapid burn angle is reduced significantly. While the variability without insert is significantly higher for direct-injection

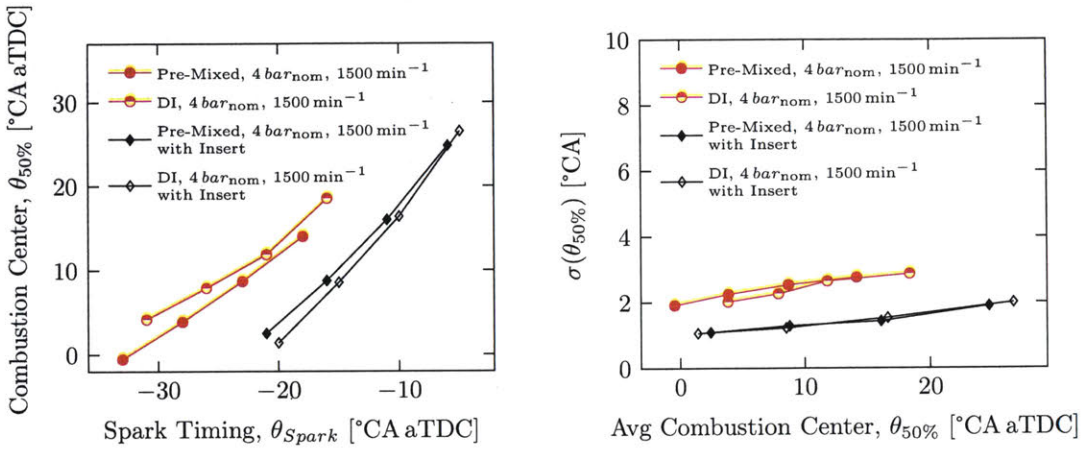

Figure 8-48: Influence of the increased tumble motion caused by the intake port insert on average combustion center relativ to spark timing (left), as well as on the variability of the combustion center (right). The combustion center variability is decreased significantly by the insert, and there seems to be little difference between direct-injection and premixed combustion.

compared to premixed combustion it appears that with the insert the variability is lower and approximately the same with insert for both cases.

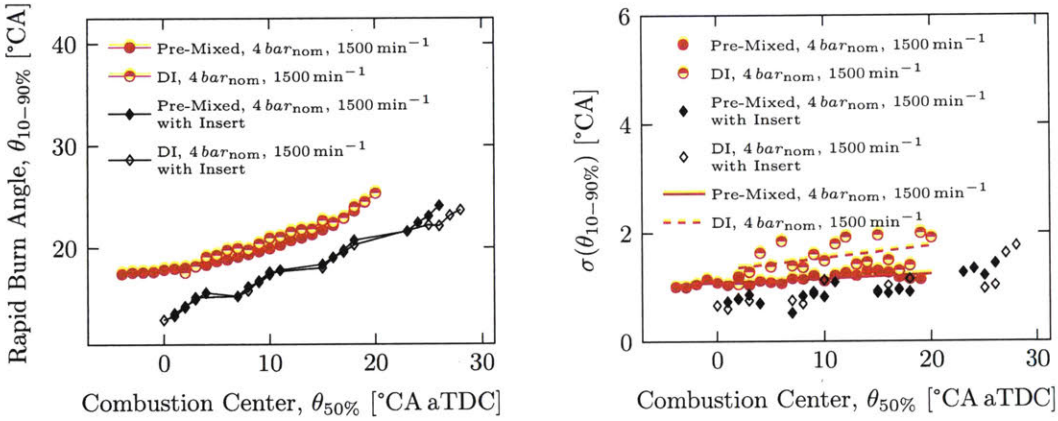

Figure 8-49: Influence of increased tumble motion on the relationship between rapid burn angle and combustion center (left), and on the variability of the rapid burn angle as a function of combustion center (right).

It can be concluded that for high tumble flow as caused by the insert, charge motion becomes the most important influence on the CCV of combustion, as

- the variability of combustion converges towards a common value independent of factors that otherwise influenced the CCV, such as direct-injection compared to premixed combustion.

- In this case the insert increased the tumble motion on average by 77 % over the entire valve lift. It appears to be reasonable that this behavior could be observed after a certain threshold value for tumble motion.

- The reduced CCV of combustion caused by the increase in tumble motion through the insert comes at the cost of reduced air mass flow into the engine, which

  - at part load, could be compensated for by de-throttling
  - at operation close to wide open throttle, could not be compensated for easily and lead to a slight decrease in performance
  - at highly boosted load, could be compensated for by delayed opening of the turbocharger waste-gate

8.7 Cycle-to-Cycle Variation and Knock

In this section the influence of cycle-to-cycle variation on knock will be investigated. In a first step the theoretical knock limit for the parameterization of the heat release schedule will be investigated in simulations using the Livengood Wu integral (LWI) and the ignition delay correlation from Douaud and Eyzat. Subsequently, the influence of the hot spot will be incorporated into this approach. And lastly a comparison with experimental data will serves to quantify the influence of the hot spot on the CCV of the knock limit.

Simulation

A widely used approach in literature to determine the autoignition time is the Livengood-Wu autoignition integral used together with an ignition delay correlation, a simplified approach that proves to be quite reliable in reality[30–32,48]. The Douaud and Eyzat ignition delay correlation will be used here[18]. The Livengood-Wu autoignition integral (I_{AI}) and the Douaud and Eyzat ignition delay correlation (τ_{DE}) are defined by

(compare Equation 8.3, and Equation 8.2 for a more detailed explanation),

$$I_{AI}(t) = \int_{t_0}^{t} \frac{1}{\tau_{DE}(p(t), T(t))}\, dt \equiv LWI \tag{8.18}$$

$$\tau_{DE}(p, T) = 0.01932 \cdot \left(\frac{ON}{100}\right)^{3.4017} \cdot p^{-1.7} \cdot e^{\frac{3800}{T}} \qquad [s] \tag{8.19}$$

The temperature in the Douaud and Eyzat correlation is the temperature of the unburned mixture, so called end-gas. Autoignition or knock occurs at the time when the Livengood-Wu integral reaches a value of one before the end of combustion. In other words knock occurs if autoignition in the end-gas occurs before the entire charge has been burnt by the flame front initiating at the spark plug.

A Wiebe combustion approach was used to compute the end-gas pressure and temperature for various values of combustion center and rapid burn angle in a GT-Power simulation. Subsequently, the value of the Livengood-Wu integral at end of combustion (LWI_{EOC}) was computed, to determine the knock limit (KL) as a function of the heat release schedule parameterization. A heavily knocking operating condition with an engine speed of $1500\,\mathrm{min}^{-1}$ and a net indicated mean effective pressure of 12 bar at maximum brake torque spark timing was chosen. A total of 66 operating points over the following interval were simulated,

$$[-4, -1, ..., 23, 27]_{\theta_{50\%}} \times [5, 10, ..., 30]_{\theta_{10-90\%}}. \tag{8.20}$$

The contour lines for the Livengood Wu integral as a function of combustion center and rapid burn angle are depicted in Figure 8-50. The knock limit occurs when the Livengood Wu integral approaches the value of one at the end of combustion. In other words the LWI predicts knock to occur for values equal or larger than one, whereas no knocking combustion is predicted for values smaller than one. The predicted knock limit where the LWI approaches the value one, appears to be more sensitive to the rapid burn angle for combustion phasing of approximately 8 °CA and earlier, whereas it becomes more and more a function of the combustion center for later combustion phasing.

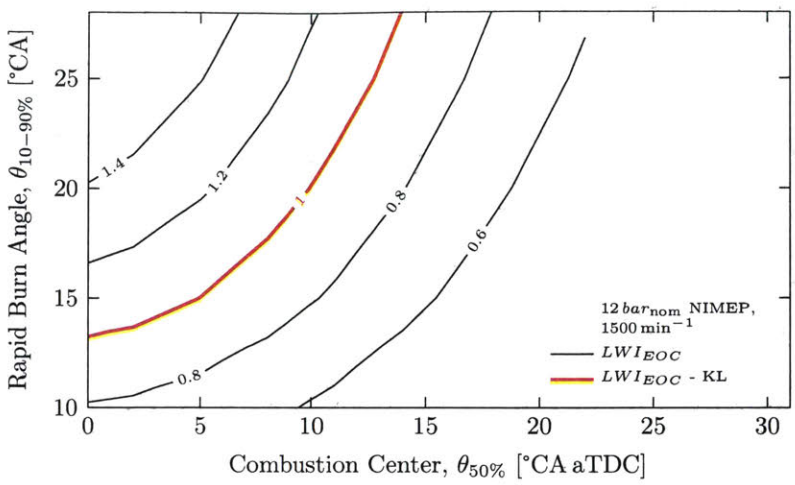

Figure 8-50: Contour lines of the Livengood Wu integral as a function of combustion center and rapid burn angle. Knock is predicted to occur in areas where the integral reaches values larger or equal to one.

The Livengood Wu integral does not explicitly account for cycle-to-cycle variations, as it only depends on the pressure temperature traces of the end-gas. And hence the knock limit is clearly defined in terms of rapid burn angle and combustion center in Figure 8-50. Before finding a way to account for cycle-to-cycle variation with the Livengood Wu integral, the dominant CCV at this operating condition will be identified.

Some of the cycle-to-cycle variation that could influence the knock behavior of the engine are variations in

- the flow field,
- the residual gas fraction, mixture and temperature,
- the trapped fuel and air mass,
- as well as the location and temperature of the hot spot.

Though it is difficult to quantify the amount of variability and the influence of the various sources on the knock behavior of the engine, it is possible to compare them qualitatively. At the considered high load operating condition, the flow field is comparatively stable. The GT-Power simulation indicates that the amount of residuals

are relatively low with a mass fraction of 3.9 %. Furthermore, the amount of trapped fuel and air mass is unlikely to change much due to slightly negative valve overlap, and for direct-injection there is practically no change in trapped fuel mass.

The hot spot is a relatively small area located on the surface of any solid part in the combustion chamber, with a locally highly elevated temperature compared to the surrounding area. The position and temperature of the hot spot can vary widely, and hot spot temperatures of up to 2000 K can be found in literature[52]. It is thus conceivable that the cycle-to-cycle variation of the hot spot can potentially influence the knock behavior strongly. Thus the influence of the hot spot on the end-gas is due to heat transfer from the hot surface area and due to locally higher temperatures due to residual temperatures and mixing. And hence the influence of the hotspot will be defined as a zone with locally higher temperature, though lower than the actual hot spot on the surface, caused by heat transfer and inhomogeneities. Ignoring the influence of the other aforementioned CCVs on the knock limit, an approach to incorporate the influence the hot spot on the Livengood Wu integral is developed in the following.

The LWI does not take temperature gradients or the location of the end-gas into account, and hence the results of the Livengood Wu integral can be interpreted differently. One interpretation is that the end-gas is a homogeneous mixture with a spatially constant temperature distribution, that is the way it was calculated in Figure 8-50. Since the LWI is practically a zero dimensional approach that only takes temperature and pressure into account, it could also be assumed that the Livengood Wu integral is only calculated for a small reactive center in the end-gas in the vicinity of the hot spot. If this center is sufficiently small, its rise in temperature through the hot spot would hardly influence the overall temperature of the entire end-gas nor the in-cylinder pressure much.

Given these assumptions the influence of the hotspot on the Livengood Wu integral can be simulated by adding a scalar value to the end-gas temperature trace from the GT-Power simulation, while keeping the same pressure trace. This way, however, the simulation cannot predict the location of the hot spot nor its actual temperature,

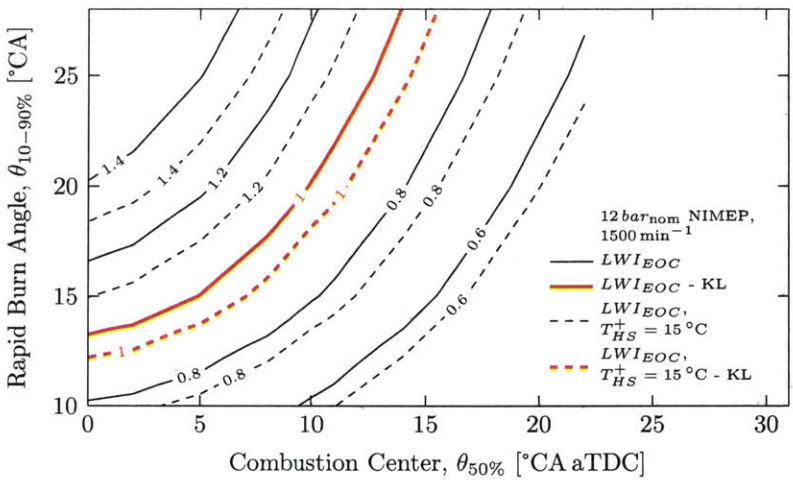

Figure 8-51: Influence of the rise in end-gas temperature caused by hot spot on the Livengood Wu integral (LWI) at the end of combustion. The simulated rise of the end-gas temperature pocket due to hot spot is equal to 15 °C (as denoted by T^{+}_{HS}).

but only by how much it causes the temperature of the adjacent end-gas pocket to rise. The influence of a 15 °C increase in end-gas temperature on the LWI is shown in Figure 8-51. The end-gas temperature increase due to hot spot in the simulation will be denoted by T^{+}_{HS}. An increase of end-gas temperature by 15 °C results in a shift of the knock limit towards later combustion phasing by approximately1.8 °CA and towards shorter rapid burn angles by approximately 1.9 °CA. This is consistent with the conventional wisdom that a 7 K rise in intake temperature would delay the knock limited spark advance by 1 °CA[3].

Experimental Observations

After establishing the theoretical impact of the hotspot on the knock limit a comparison with experimental data is necessary. Spark sweeps at a nominal net indicated mean effective pressure of 12 bar at MBT and an engine speed of 1500 min^{-1} were performed. A total of 22600 cycles with direct-injection and 28200 cycles with premixed combustion were recorded.

The data was binned into a two-dimensional mesh according to its combustion center and rapid burn angle. The mesh size was kept constant at 1 °CA for both combustion center and rapid burn angle. And the relative knock probability was

computed for each cell of the mesh with twenty data points or more, whereas cells with fewer data points were discarded due to insufficient sample size for the averaging process. A cycle was deemed to be a knocking cycle when the pressure amplitude of its filtered pressure signal was larger or equal to 1 bar, compare Section 7.3 for a detailed explanation. And the relative knock probability was defined as the ratio of knocking cycles to all cycles within a cell of the mesh. The relative knock probability was then interpolated for mesh cells that had a sufficient number of neighboring cells, but no extrapolation was performed. This process was applied to both direct-injection and premixed data independently, compare heat map in Figure 8-52 for the results.

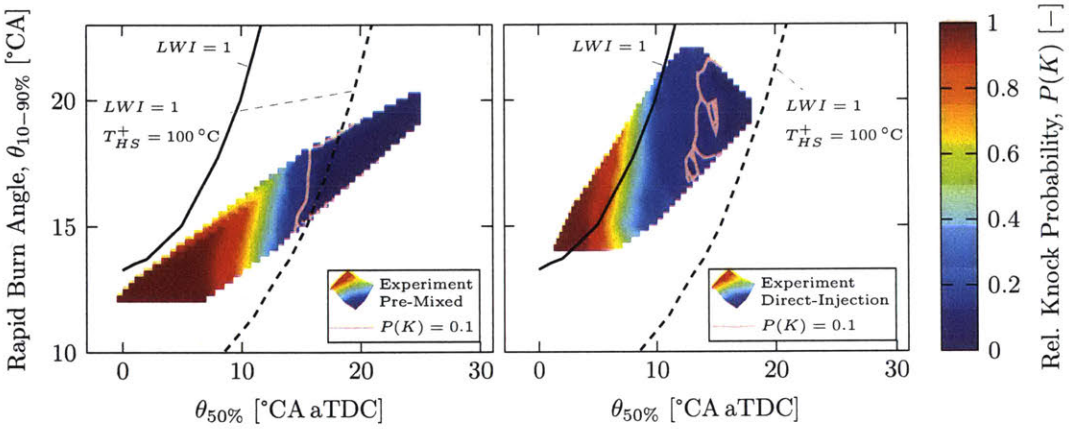

Figure 8-52: Relative probability of knock for premixed combustion (left) and direct-injection (right) as a function of combustion center and rapid burn angle. Data interpolated from quadratic mesh cells of size 1 °CA for twenty observations or more, data was not extrapolated. The black line indicate a value of one for the LWI, and the dashed balck line indicates a value of one for the LWI when the end-gas temperature is raised by 100 °C due to hot spot. It is important to notice that the LWI is not calibrated, so that the absolute position of the contours could be shifted by a fudge factor depending on a specific engine. And thus the focus is on the change of the LWI line due to hot spot.

For the premixed case the spread in $\theta_{50\%}$ of the knock limit agrees well with the prediction of the knock limit by the Livengood Wu integral for a temperature rise in the reactive end-gas center of 100 °C due to the hot spot ($T^+_{HS} = 100\,°C$) not taking other possible influences from CCV into account. The simulation predicts that the knock limit occurs for earlier combustion centers for rapid burn angles of less than 15 °CA. The data, however, indicates that the knock limit is mostly dependent on the combustion phasing even for shorter burn durations. It is important to note though

that the Livengood Wu integral was not calibrated and if offset by a fudge factor it would match the observations reasonably well. The focus here is on the how much the line is shifted by the hot spot, which is consistent with observation.

In the direct-injection case, the knock limit is shifted towards an earlier combustion center. The reason for that is probably the charge cooling effect from fuel vaporization during direct-injection that has been shown to reduce the likelihood of knock[69,70], which is absent in the case of premixed combustion and also not taken into account when the Livengood Wu integral was computed.

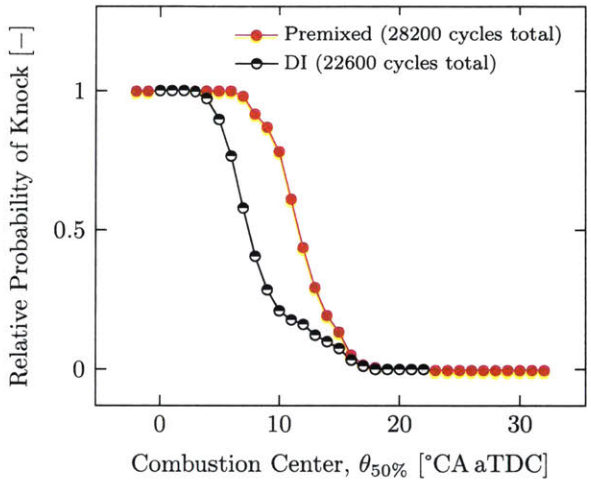

Figure 8-53: The zero percent knock probability for direct-injection occurs at a combustion center of 18 °CA, one degree earlier as for pre-mixed combustion with 19 °CA. The limit where the knock probability first becomes 100 % occurs at 2 °CA four degree crank angle earlier as for pre-mixed combustion with 6 °CA. And hence the spread is larger for direct-injection with 16 °CA compared to 13 °CA.

Since the data shows that the knock limit is mostly a function of the combustion center and little sensitive to the rapid burn angle it is informative to plot the relative probability of knock as a function of combustion center, compare Figure 8-53. Furthermore, binning the data only by combustion center significantly increases the sample size per bin. The bin width is equal to 1 °CA with an integer center. The knock limited combustion phasing occurs earlier for direct-injection, though the spread between 0 % to 100 % knock probability is larger compared to the premixed case. The slightly larger spread might be due to larger variations in local air-fuel ratio.

The influence of increased charge motion on the knock behavior of the engine was also investigated, compare Figure 8-54. Increased tumble motion was induced by a reduction of 70 % of the cross sectional area of the intake port with a port insert resulting on average in an increase of tumble motion by 77 %, compare Section 8.6. The increased charge motion reduces the burn duration, and the rapid burn angle is reduced for any combustion phasing. Reduction in rapid burn angle seems to retard the knock limited combustion center for premixed combustion, whereas it advances it for direct-injection reducing the knock tendency of the engine.

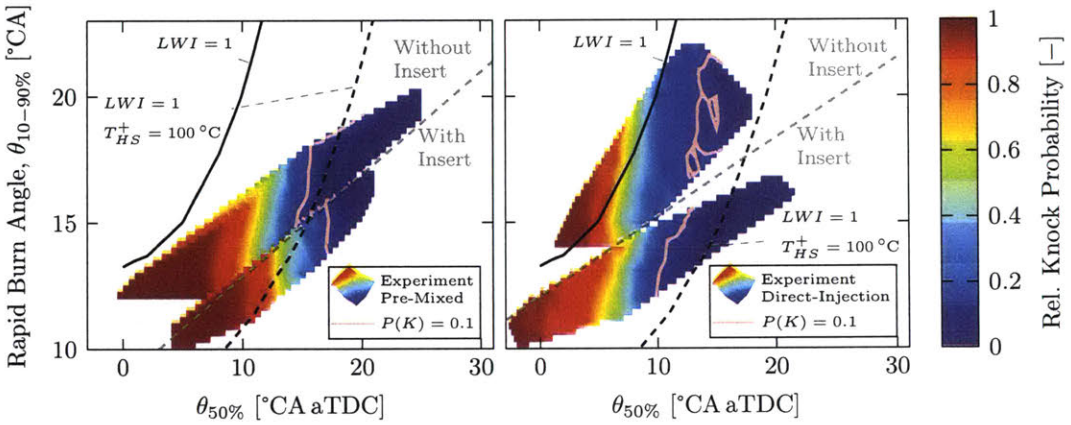

Figure 8-54: The insert decreases the knock resistance for premixed combustion (left) and increases the knock resistance of the engine for direct-injection (right). The prediction of the Livengood Wu integral for an increased end-gas temperature of 100 °C due to hot spot agrees qualitatively well with the experimental data for direct-injection with insert. It is important to notice that the LWI is not calibrated, so that the absolute position of the contours could be shifted by a fudge factor depending on this specific engine. And thus the focus is on the change of the LWI line due to hot spot.

In either case the time available for autoignition is reduced because the charge burns through faster. The competing effect is that a faster burning speed causes a quicker pressure rise increasing the likelihood of autoignition. It has been shown that knock can originate from local exothermic centers[37], in the premixed case the center might be more reactive due to higher mixture homogeneity. Whereas in the direct-injection case the air-fuel mixture in the reactive center might be less favorable to cause autoignition within the time available.

For direct-injection, the line of the knock limit for the rapid burn angle as a function of combustion center is somewhat more slanted for higher combustion speeds

which qualitatively agrees with the prediction of the Livengood Wu integral, though it appears to be less sloped in the experiments. Nevertheless the influence of the combustion center on the knock limit appears to be more significant. And since the combustion center is linearly dependent on the spark timing, it is directly correlated with the knock limited spark advance. This trend is reversed for premixed combustion as knock tendency seems to increase with decreasing rapid burn angle for constant combustion center. The knock limit only as a function of combustion center shows the same trend, compare Figure 8-55. In the case of premixed combustion the insert reduces the spread between 100 % and 0 % knock probability slightly by 1 °CA from 13 °CA to 12 °CA, though it increases the knock tendency of the engine for a given combustion phasing.

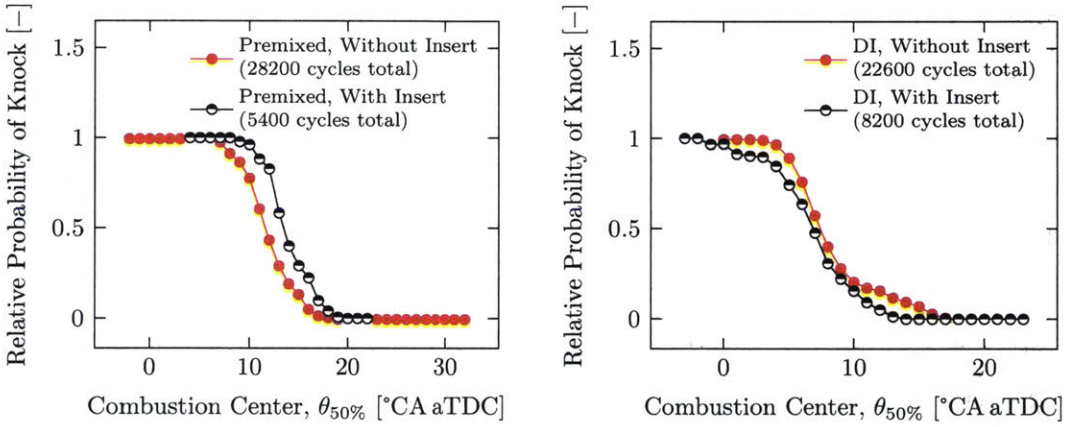

Figure 8-55: Relative probability of knock as a function of the combustion center with and without insert for premixed combustion (left) and direct-injection (right). While the insert has hardly any influence of the variability of the knock limit (smallest difference between 0 % and 100 % knock), it increases knock tendency for premixed combustion and reduces it for direct-injection.

Increased charge tumble motion by the insert retards the knock limited combustion center by 1 °CA from 19 °CA aTDC to 20 °CA aTDC in the case of premixed combustion, and hence the knock limited spark advance resulting in a reduction of engine performance or efficiency by approximately 1 % (compare Figure 8-56). In the case of direct-injection, however, the increased charge motion leads to an advance in knock limited combustion center by 4 °CA from 18 °CA aTDC to 14 °CA aTDC resulting in a three percentage point increase of engine performance or efficiency compared

to the case without the insert.

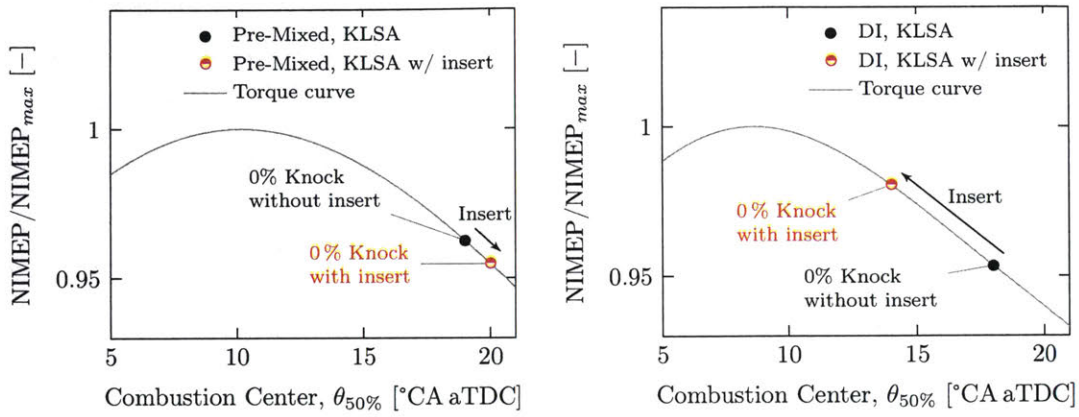

Figure 8-56: The insert retards knock limited combustion center for premixed combustion (left) by 1 °CA resulting in a decrease in efficiency of approximately 1 %. For direct-injection (right) the effect is the opposite, advancing the knock limited combustion center by 4 °CA increasing the efficiency by approximately 3 %.

So far only knock occurrence was considered as a binary event, however, for real world engine operation the knock amplitude is of significant importance as it relates directly to the possible harm it could cause. While all occurrences of knock are undesirable, it has been observed that significant damage can be caused when an engine is operated with a knock intensity (KI) of 5 bar or more[55]. The knock intensity here is defined to be the maximum amplitude's absolute value of the filtered in-cylinder pressure signal. Compare Section 7.3 for a more detailed explanation.

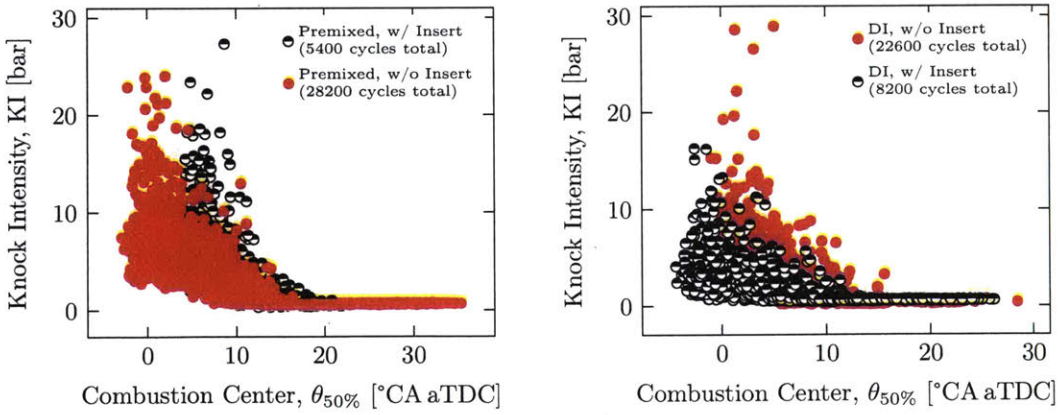

Figure 8-57: The knock intensity is signficantly higher for premixed combustion (left) as compared to direct-injection (right) for a nominal operating condition of 12 bar NIMEP at an engine speed of 1500 min^{-1}. While the insert influences the knock tendency of the engine negatively for premixed combustion, it improves knock behavior for direct-injection and reduces the maximum KI slightly.

It may be concluded, that the insert has a positive influence on the knock behavior of the engine when operated with direct-injection, as the knock limited spark advance is shifted towards earlier timing resulting in increased efficiency. At the same time increased tumble motion with direct-injection also appears to reduce the knock intensity, which potentially reduces the damage caused by a sporadic knocking event. However, the cycle-to-cycle variation of the knock limit (minimum distance between combustion center with 0 % and 100 % knock probability) appears to be unchanged by increased tumble motion. For premixed combustion the effect of increased tumble motion appears to be quite the opposite, as it delays the KLSA reducing efficiency, and increases the KI.

Lastly the influence of increased tumble motion on the covariance of net indicated mean effective pressure for the high load operating point with a nominal net indicated mean effective pressure of 12 bar and an engine speed of 1500 min^{-1} is investigated. Only engine operation with direct-injection is considered here, because the amount of fuel mass trapped is approximately constant in that case. The insert reduces the covariance of net indicated mean effective pressure by more than 60 % from 1.6 % to 0.58 % at the knock limited combustion center of 14 °CA aTDC, compare Figure 8-58.

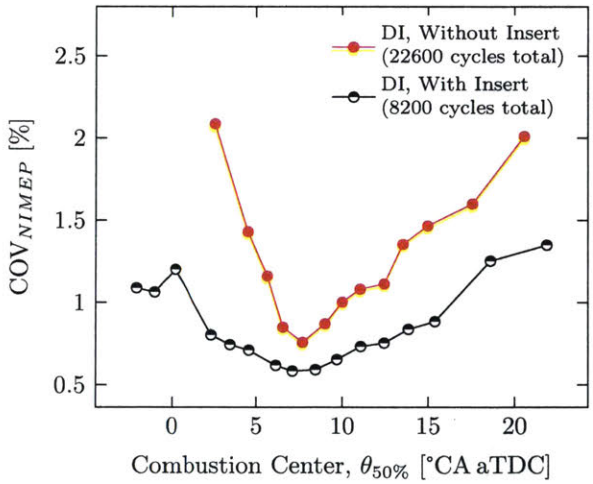

Figure 8-58: Increased tumble motion due to the insert reduces the covariance of net indicated mean effective pressure at maximum brake torque spark timing, and increasingly for delayed combustion. The unsteady behavior of the curve around top dead center is likely due to heavily knocking combustion.

It may be concluded from the simulation results of the Livengood Wu integral

together with the experimental data that,

- The KLSA is retarded for premixed combustion compared to direct-injection, most likely due to the charge cooling effect from the heat of vaporization.
- The influence of hot spot CCV on the variability of the knock limit is approximately the same for premixed combustion and direct-injection
  - the maximum variation of the knock limit corresponds approximately to a temperature rise of a reactive center in the end-gas by 100 °C due to hot spot
- The insert increases the tumble motion significantly resulting in reduced burn durations.
  - it needs to be noted that the insert is a flow restriction reducing the mass flow into the engine, which needs to be compensated by increased manifold air pressure
- The insert does not change the variation of the knock limit due to hot spot significantly, but
  - for premixed combustion it increases the knock tendency of the engine, whereas
  - for direct-injection it reduces the knock tendency of the engine.
- It is not clear why the insert improves knock behavior for direct-injection while it worsens it for premixed combustion. An explanation could be that the reactive center in the end-gas is better mixed, leading to faster autoignition compared to locally more heterogeneous mixture in the case of direct-injection. Since the rapid burn angle is reduced by the insert, in this case there would not be enough time for autoignition before the charge burned through.
- The insert advances the knock limited combustion center for direct-injection by 4 °CA improving the knock limited efficiency by 3 %.

Chapter 9

Conclusion Cycle-to-Cycle Variability

Cycle-to-cycle variation of combustion was investigated experimentally with a turbocharged, direct-injected two-liter, modern gasoline passenger car engine. The heat release schedule was used as a metric to characterize the variability of the combustion. It was shown that the heat release schedule can be parameterized sufficiently for this purpose with two parameters, the combustion center ($\theta_{50\%}$), and the rapid burn angle ($\theta_{10-90\%}$). Both non knocking and knocking combustion were investigated.

For non knocking combustion it was found that there are two types of influences on the cycle-to-cycle variation of combustion, the combustion phasing, and the operating or engine conditions such as load, speed, tumble flow and so on. The cycle-to-cycle variation increases inherently as the combustion phasing is retarded from the maximum brake torque phasing.

A skip fire experiment was used to single out the intrinsic charge motion effect on the CCV of combustion, with practically no residuals (in the order of 1 %). Subsequently with baseline residuals ($\approx$ 10 %), it was found that the cycle-to-cycle variation of combustion compared to only the intrinsic charge motion was hardly influenced.

Further increase of the residuals up to about 20 % also had little influence on the cycle-to-cycle variation of combustion. However, the rapid burn angle increased slightly. The minuscule increase in burn duration may be due to the fact that the engine generally burns fast (rapid burn angles in the order of 20 °CA), indicating that the burn speed depends more on the turbulent flame speed than on the laminar flame

speed that is slowed down with increasing dilution resulting only in small differences.

In the case of premixed combustion it was found, that increasing load generally decreases cycle-to-cycle variation and increasing engine speed generally increases the cycle-to-cycle variation. While the engine speed appears to have little influence on cycle-to-cycle variation for GDI. The overall cycle-to-cycle variation is larger for direct injection compared to premixed combustion. However, there is evidence that significantly increased charge motion compensates the difference, indicating that charge motion above a certain threshold becomes the determining factor on cycle-to-cycle variation. Though the threshold was not explicitly defined, a port insert increased the intrinsic charge motion of the engine by 77 % on average, resulting in the same cycle-to-cycle variation of for direct-injection and premixed combustion.

For knocking combustion, the hot spot was identified to have a significant influence on the cycle-to-cycle variation of the autoignition. However, the location and temperature of the actual hot spot on a surface inside of the combustion chamber was not quantified. Only the effect of a zone of locally higher temperature in the end-gas caused by the hot spot through heat transfer, but also by non-uniformly mixed hot residual gas pockets. The contribution of each was not quantified, and in the following the influence of the hot spot will refer to both phenomena.

Engine bench experiments showed that the influence of hot spot CCV on the total variability of the knock limit is approximately the same for premixed combustion and direct-injection. The maximum variation of the knock limit corresponds approximately to a temperature rise of the reactive center in the end-gas by 100 °C due to hot spot and non-uniform residual mixing, which was determined by a simulation of the Livengood Wu integral.

Furthermore increased charge motion due to the intake port insert increases the tumble motion significantly resulting in reduced burn durations. However, the insert does not change the total variation of the knock limit due to hot spot significantly, but it increases the knock tendency of the engine for premixed combustion whereas it reduces the knock tendency of the engine for direct-injection.

It is not clear why the insert improves knock behavior for direct-injection while it

worsens it for premixed combustion. An explanation could be that the reactive center in the end-gas is better mixed, leading to faster autoignition compared to locally more heterogeneous mixture in the case of direct-injection. Since the rapid burn angle is reduced by the insert, in this case there would not be enough time for autoignition before the charge burned through. The insert advances the knock limited combustion center for direct-injection by 4 °CA improving the knock limited efficiency by up to 3 % for the investigated operating condition of $1500\,\mathrm{min}^{-1}$ and a nominal load of 12 bar net indicated mean effective pressure.

9.1 Recommendations for Future Work

The engine used in this study was operated as a single cylinder engine to single out the cycle-to-cycle variation of combustion for a given cylinder without interference. In an actual passenger car, however, it would be operated as a four cylinder engine. As a result there is interaction between the cycle-to-cycle variation of each cylinder that was not investigated here. Furthermore, operating the engine with a turbocharger causes a feedback between the engine CCV and turbocharger CCV. The following experiments could be performed to gain further insight into the cycle-to-cycle variation of combustion under real world operating conditions.

- Cycle-to-cycle variation of turbocharger independently and interaction with CCV of engine operation
- Interaction of the cycle-to-cycle variation from one cylinder to another cylinder
- Influence of transient engine operation for instance during strong acceleration on CCV of combustion.

Furthermore the engine bench experiments indicated significant reduction in cycle-to-cycle variation for significantly increased charge motion. However, the flow restriction causes a reduced mass flow into the cylinder which needs to be compensated by higher manifold air pressure. In this study the pressure was adjusted by an externally

driven supercharger whereas on an actual engine the turbocharger would likely have to deliver increased boost pressure. Further experiments are necessary to understand the interaction between port flow restriction and turbocharger operation.

Bibliography

[1] P. G. Aleiferis, a. M. K. P. Taylor, J. H. Whitelaw, K. Ishii, and Y. Urata. Cyclic Variations of Initial Flame Kernel Growth in a Honda VTEC-E Lean-Burn Spark-Ignition Engine. *SAE Technical Paper*, (2000-01-1207), 2000. doi:10.4271/2000-01-1207.

[2] M. M. Ameen, M. Mirzaeian, F. Millo, and S. Som. Numerical Prediction of CCV in a PFI Engine Using a Parallel LES Approach. In *Proceedings of the ASME 2017 Internal Combustion Engine Fall Technical Conference ICEF2017*, pages 1–12, 2017.

[3] W. P. Attard, H. Blaxill, E. K. Anderson, and P. Litke. Knock Limit Extension with a Gasoline Fueled Pre-Chamber Jet Igniter in a Modern Vehicle Powertrain. *SAE International Journal of Engines*, (2012-01-1143), 2012. ISSN 1946-3944. doi:10.4271/2012-01-1143.

[4] F. A. Ayala and J. B. Heywood. Lean SI Engines: the Role of Combustion Variability in Defining Lean Limits. *SAE Technical Paper Series*, (2007-24-0030), 2007. doi:10.4271/2007-24-0030.

[5] D. Ball and D. Moser. Cold Start Calibration of Current PZEV Vehicles and the Impact of LEV-III Emission Regulations. *SAE Int. J. Fuels Lubr.*, (2012-01-1245), 2012. doi:10.4271/2012-01-1245.

[6] V. Bermúdez, J. M. Luján, H. Climent, and D. Campos. Assessment of pollutants emission and aftertreatment efficiency in a GTDi engine including cooled LP-EGR system under [...]. *Applied Energy*, 2015. ISSN 03062619. doi:10.1016/j.apenergy.2015.08.071.

[7] A. W. Berntsson, G. Josefsson, R. Ekdahl, R. Ogink, and B. Grandin. The Effect of Tumble Flow on Efficiency for a Direct Injected Turbocharged Downsized Gasoline Engine. *SAE International*, (2011-24-0054), 2011. doi:10.4271/2011-24-0054.

[8] P. Bielaczyc, J. Woodburn, and A. Szczotka. Exhaust Emissions of Gaseous and Solid Pollutants Measured over the NEDC , FTP-75 and WLTC Chassis Dynamometer Driving Cycles. *SAE International*, (2016-01-1008), 2016. doi:10.4271/2016-01-1008.

[9] J. Bolt, S. Bergin, and F. Vesper. The Influence of the Exhaust Back Pressure of a Piston Engine on Air Consumption, Performance, and Emissions. *SAE Technical Paper*, page SAE Technical Paper 730195, 1973. doi:10.4271/730195.

[10] M. Borland and F. Zhao. Application of Secondary Air Injection for Simultaneously Reducing Converter-In Emissions and Improving Catalyst Light-Off Performance. *SAE Technical Paper*, (2002-01-2803), 2002. doi:10.4271/2002-01-2803.

[11] C. Brinkmeier, G. Eigenberger, S. Buchner, and A. Donnerstag. Transient Emissions of a SULEV Catalytic Converter System Dynamic Simulation vs. Dynamometer Measurements. *SAE Technical Paper Series*, (2003-01-1001), 2003. doi:10.4271/2003-01-1001.

[12] M. F. J. Brunt and C. R. Pond. Evaluation of Techniques for Absolute Cylinder Pressure Correction. *SAE Technical Papers*, (412):SAE 970036, 1997. doi:10.4271/970036.

[13] K. Burgdorf and I. Denbratt. Comparison of cylinder pressure based knock detection methods. *Doktorsavhandlingar vid Chalmers Tekniska Hogskola*, (972932), 1997. ISSN 0346718X. doi:10.4271/972932.

[14] K. Cedrone and W. K. Cheng. Using Valve Timing and Exhaust Back Pressure to Improve Catalyst Warm-Up Time. *SAE International*, (2013-01-2656), 2013. doi:10.4271/2013-01-2656.

[15] M. Chambers and R. Schmitt. U.S. DOT Fact Sheet. Technical report, 2015.

[16] R. S. Davis and G. J. Patterson. Cylinder Pressure Data Quality Checks and Procedures to Maximize Data Accuracy in Thermal Fluid Sciences 2006. *Techniques*, 2006(724), 2006. doi:10.4271/2006-01-1346.

[17] R. Dijkstra, M. Boot, R. Eichhorn, D. Smeulders, J. Lennblad, and A. Serrarens. Experimental Analysis of Engine Exhaust Waste Energy Recovery Using Power Turbine Technology for Light Duty Application. *SAE International Journal of Engines*, 5(4):2012–01–1749, 2012. ISSN 1946-3944. doi:10.4271/2012-01-1749.

[18] A. Douaud and P. Eyzat. Four-Octane-Number Method for Predicting the Anti-Knock Behavior of Fuels and Engines. *SAE*, 87:294–308, 1978. ISSN 0148-7191. doi:10.4271/780080.

[19] A. Dulbecco, S. Richard, and C. Angelberger. Investigation on the Potential of Quantitatively Predicting CCV in DI-SI Engines by Using a One-Dimensional CFD Physical Modeling Approach: Focus on Charge Dilution and In-Cylinder Aerodynamics Intensity. *SAE International Journal of Engines*, (2015-24-2401), 2015. ISSN 1946-3944. doi:10.4271/2015-24-2401.

[20] L. Eltinge. Fuel-Air Ratio and Distribution from Exhaust Gas Composition. *SAE International*, (Technical Paper 680114), 1968. doi:10.4271/680114.

[21] U. EPA. Inventory of U.S. Greenhouse Gas Emissions and Sinks: 1990-2014. *Ipcc*, (EPA 430-R-10-006), 2016. ISSN 00976326. doi:EPA-430-R-13-001.

[22] W. L. R. Gallo and R. F. Guerra. Ignition Timing as a Strategy to Reduce Spark-Ignition Engine Emissions in the Cold Phase. *SAE Technical Paper*, (2013-36-0314), 2013. doi:10.4271/2013-36-0314.

[23] A. F. Ghoniem. Needs, resources and climate change: Clean and efficient conversion technologies. *Progress in Energy and Combustion Science*, 2011. ISSN 03601285. doi:10.1016/j.pecs.2010.02.006.

[24] S. Halsall, K. Luchansky, Y. Zeng, R. Davis, and R. Herrin. Development of the Combustion System for the General Motors Fifth Generation Small Block Engine Family. *SAE Technical Paper*, (2013-01-1732), 2013. doi:10.4271/2013-01-1732.

[25] F.-j. Hanel, A. Gmbh, E. Otto, B. M. W. Ag, R. Brück, and E. Gmbh. Electrically Heated Catalytic Converter (EHC) in the BMW ALPINA B12 5.7 Switch-Tronic. *SAE Technical Paper Series*, (960349), 1996. doi:10.4271/960349.

[26] S. Heller and G. Wachtmeister. Analysis and Modeling of Heat Transfer in the SI Engine Exhaust System During Warm-Up. *SAE Technical Paper Series*, (2007-01-1092):776–790, 2007. doi:10.4271/2007-01-1092.

[27] J. B. Heywood. *Internal Combustion Engine Fundementals*, volume 21. 1988. ISBN 007028637X.

[28] S. Hokimoto, T. Kuboyama, and Y. Moriyoshi. Analyses of Cycle-to-Cycle Variation of Combustion and In- Cylinder Flow in a Port Injection Gasoline Engine Using PIV and PLIF Techniques. *SAE Technical Paper*, (2017-01-2213), 2017. doi:10.4271/2017-01-2213.

[29] T. V. Johnson. Vehicular emissions in review. *SAE International*, (2012-01-0368), 2012. ISSN 1946-3936, 1946-3944. doi:10.4271/2012-01-0368.

[30] G. Kalghatgi, H. Babiker, and J. Badra. A Simple Method to Predict Knock Using Toluene, N-Heptane and Iso-Octane Blends (TPRF) as Gasoline Surrogates. *SAE International Journal of Engines*, 8(2):2015–01–0757, 2015. ISSN 1946-3944. doi:10.4271/2015-01-0757. URL `http://papers.sae.org/2015-01-0757/`.

[31] G. Kalghatgi, K. Morganti, I. Algunaibet, M. Sarathy, and R. Dibble. Knock Prediction Using a Simple Model for Ignition Delay. *SAE Technical Paper*, (2016-01-0702), 2017. doi:10.4271/2016-01-0702.

[32] E. Kasseris and J. B. Heywood. Charge Cooling Effects on Knock Limits in SI DI Engines Using Gasoline/Ethanol Blends: Part 2-Effective Octane Numbers. *SAE International Journal of Fuels and Lubricants*, 5(2):2012–01–1284, 2012. ISSN 1946-3960. doi:10.4271/2012-01-1284. URL `http://papers.sae.org/2012-01-1284/`.

[33] E. P. Kasseris and J. B. Heywood. Comparative Analysis of Automotive Powertrain Choices for the Next 25 Years. *SAE International*, (2007-01-1605), 2007. doi:10.4271/2007-01-1605.

[34] W. M. Kays and M. E. Crawford. *Convective Heat and Mass Transfer*. McGraw-Hill series in mechanical engineering. McGraw-Hill, 1993. ISBN 9780070337213.

[35] Y.-d. Kim, W.-s. Kim, and Y. Lee. International Journal of Heat and Mass Transfer Influences of exhaust gas temperature and flow rate on optimal catalyst activity profiles. *International Journal of Heat and Mass Transfer*, 85:841–851, 2015. ISSN 0017-9310. doi:10.1016/j.ijheatmasstransfer.2015.02.043.

[36] G. C. Koltsakis, P. A. Konstantinidis, and A. M. Stamatelos. Development and application range of mathematical models for 3-way catalytic converters. *Applied Catalysis B: Environmental*, 1997. ISSN 09263373. doi:10.1016/S0926-3373(96)00073-2.

[37] G. König, R. R. Maly, D. Bradley, A. K. C. Lau, and C. G. W. Sheppard. Role of Exothermic Centres on Knock Initiation and Knock Damage. (902136), 1990. doi:10.4271/902136. URL `http://papers.sae.org/902136/`.

[38] S. Kubota, K. Tanaka, and M. Konno. Effect of Relative Positions of Air-Fuel Mixture Distribution and Ignition on Combustion Variation in Gasoline Engine. *SAE International Journal of Engines*, 7(4):2014–01–2629, 2014. ISSN 1946-3944. doi:10.4271/2014-01-2629.

[39] R. H. Kuratle and B. Märki. Influencing Parameters and Error Sources During Indication on Internal Combustion Engines. *SAE Technical Paper Series*, (920233), 1992. doi:10.4271/920233.

[40] K. R. Lang and W. K. Cheng. A Novel Strategy for Fast Catalyst Light-Off without the Use of an Air Pump. *SAE International*, (2007-01-0044), 2007. doi:10.4271/2007-01-0044.

[41] B. Lecointe and G. Monnier. Downsizing a Gasoline Engine Using Turbocharging with Direct Injection. *SAE International*, (2003-01-0542), 2003. doi:10.4271/2003-01-0542.

[42] D. Lee and J. B. Heywood. Effects of Secondary Air Injection During Cold Start of SI Engines. *SAE Technical Paper*, (2010-01-2124), 2010. doi:10.4271/2010-01-2124.

[43] S. Lee, C. Bae, Y. Lee, and T. Han. Effects of Engine Operating Conditions on Catalytic Converter Temperature in an SI Engine Effects of Engine Operating Conditions on Catalytic Converter Temperature in an SI Engine. *SAE Technical Paper Series*, (2002-01-1677), 2002. doi:10.4271/2002-01-1677.

[44] E. Lemmon, M. McLinden, and D. Friend. Thermophysical Properties of Fluid Systems. *NIST Chemistry WebBook, NIST Standard Reference Database Number 69*, 2017. doi:10.18434/T4D303.

[45] J. M. Lyons, T. R. Carlson, and T. C. Austin. Evaluation of California Greenhouse Gas Standards and Federal Energy Independence and Security Act. *SAE International*, (2008-01-1852), 2008. doi:10.4271/2008-01-1853.

[46] N. Matthess, D. Schweich, B. Martin, and F. Castagna. From Light-Off Curves to Kinetic Rate Expressions for Three-Way Catalysts. *Topics in Catalysis*, 16 (4):119–124, 2001. ISSN 10225528. doi:10.1023/A:1016695101135.

[47] J. Matthey, L. Tao, E. Garnsey, and D. Probert. Innovation as Response to Emissions Legislation: Revisiting the Automotive Catalytic Converter at Johnson Matthey. 2009.

[48] J. McKenzie and W. Cheng. Ignition Delay Correlation for Engine Operating with Lean and with Rich Fuel-Air Mixtures. *SAE Technical Papers*, (2016-01-0699), 2016. ISSN 01487191. doi:10.4271/2016-01-0699.

[49] J. E. McKenzie. *The Autoignition Characteristics of Turbocharged Spark Ignition Engines with Exhaust Gas Recirculation.* PhD thesis, Massachusetts Institute of Technology, 2015.

[50] F. Mille and C. V. Ferraro. Knock in S . I . Engines : A Comparison between Different Techniques for Detection and Control. *SAE Technical Paper Series*, (982477), 1998.

[51] V. Mittal, B. M. Revier, J. B. Heywood, C. Town, and S. Africa. Phenomena that Determine Knock Onset in Spark-Ignition Engines. *SAE Technical Paper Series*, (2007-01-0007), 2007. doi:10.4271/2007-01-0007.

[52] M. J. Mubarak Ali, F. Hernandez Perez, S. Vedharaj, R. Vallinayagam, R. Dibble, and H. Im. Effect of Timing and Location of Hotspot on Super Knock during Pre-ignition. *SAE Paper 2017-01-0686*, 2017. ISSN 01487191. doi:10.4271/2017-01-0686.

[53] O. J. Murphy, R. T. Kukreja, and C. C. Andrews. Electrically initiated chemically heated catalytic converter to reduce cold-start emissions from automobiles. *SAE Technical Paper Series*, (1999-01-1233), 1999. doi:10.4271/1999-01-1233.

[54] L. Mussmann, D. Lindner, E. S. Lox, R. V. Yperen, T. P. Kreuzer, I. Mitsushima, S. Taniguchi, and G. Garr. The Role of Zirconium in Novel Three-Way Catalysts. *SAE Technical Paper Series*, (970465), 1997. doi:10.4271/970465.

[55] R. Nates and A. Yates. Knock damage mechanisms in spark-ignition engines. *SAE Technical Papers*, (942064), 1994. doi:10.4271/942064.

[56] T. Omura, K. Nakata, Y. Yoshihara, and D. Takahashi. Research on the Measures for Improving Cycle-to-Cycle Variations under High Tumble Combustion. *SAE Technical Paper*, (2016-01-0694), 2016. doi:10.4271/2016-01-0694.

[57] E. Otto, F. Albrecht, and J. Liebl. The Development of BMW Catalyst Concepts for LEV / ULEV and EU III / IV Legislations 6 Cylinder Engine with Close Coupled Main Catalyst. *SAE Technical Paper Series*, (980418), 1998. doi:10.4271/980418.

[58] L. Pace and M. Presti. An Alternative Way to Reduce Fuel Consumption During Cold Start: The Electrically Heated Catalyst. *SAE International*, (2011-24-0178), 2011. doi:10.4271/2011-24-0178.

[59] S. Pischinger and J. B. Heywood. A Study of Flame Development and Engine Performance with Breakdown Ignition Systems in a Visualization Engine. *SAE Technical Paper Series*, (880518), 1988. doi:10.4271/880518.

[60] S. Pischinger and J. B. Heywood. How Heat Losses to the Spark Plug Electrodes Affect Flame Kernel Development in an SI-Engine. *SAE Technical Paper Series*, (900021), 1990. ISSN 0148-7191. doi:10.4271/900021.

[61] C. Please, P. Hagan, and D. Schwendeman. Light-Off Behavior of Catalytic Converters. *Siam J. Appl. Math.*, 1994.

[62] A. L. Randolph. Methods of Processing Cylinder-Pressure Transducer Signals to Maximize Data Accuracy. *SAE Technical Paper*, 1990. ISSN 0148-7191. doi:10.4271/900170.

[63] A. L. Randolph. Cylinder-Pressure-Transducer Mounting Techniques to Maximize Data Accuracy. *SAE International*, 1990. doi:10.4271/900171.

[64] G. M. Rassweiler and L. Withrow. Motion Pictures of Engine Flames Correlated with Pressure Cards. *SAE Journal of Transactions*, 42(5):185–204, 1938. ISSN 0148-7191. doi:10.4271/380139.

[65] S. Sabatini, I. Kil, J. Dekar, T. Hamilton, J. Wuttke, M. A. Smith, M. A. Hoffman, and S. Onori. A new semi-empirical temperature model for the three way catalytic converter. *IFAC Proceedings Volumes (IFAC-PapersOnline)*, 2015. ISSN 14746670. doi:10.1016/j.ifacol.2015.10.062.

[66] R. Scarcelli, K. Richards, E. Pomraning, P. K. Senecal, T. Wallner, and J. Sevik. Cycle-to-Cycle Variations in Multi-Cycle Engine RANS Simulations. *SAE International*, (2016-01-0593), 2016. doi:10.4271/2016-01-0593.Copyright.

[67] B. T. Shaw, G. D. Fischer, and J. K. Hedrick. *A Simplified Coldstart Catalyst Thermal Model to Reduce Hydrocarbon Emissions*, volume 35. IFAC, 2002. doi:10.3182/20020721-6-ES-1901.01519.

[68] M. H. Shelby, R. a. Stein, and C. C. Warren. A New Analysis Method for Accurate Accounting of IC Engine Pumping Work and Indicated Work. *SAE Technical Paper Series*, 2004-01-12(724), 2004. ISSN 0148-7191. doi:10.4271/2004-01-1262.

[69] C. S. Sluder, J. P. Szybist, R. L. McCormick, M. A. Ratcliff, and B. T. Zigler. Exploring the Relationship Between Octane Sensitivity and Heat-of-Vaporization. *SAE International Journal of Fuels and Lubricants*, 9(1):2016–01–0836, 2016. ISSN 1946-3960. doi:10.4271/2016-01-0836.

[70] R. A. Stein, D. Polovina, K. Roth, M. Foster, M. Lynskey, T. Whiting, J. E. Anderson, M. H. Shelby, T. G. Leone, and S. VanderGriend. Effect of Heat of Vaporization, Chemical Octane, and Sensitivity on Knock Limit for Ethanol - Gasoline Blends. *SAE International Journal of Fuels and Lubricants*, 5(2): 2012–01–1277, 2012. ISSN 1946-3960. doi:10.4271/2012-01-1277.

[71] U.S. Department of State. Second Biennial Report of the United States of America Under the United Nations Framework Convention. 2016.

[72] A. Waltner, G. Loose, A. Hirschmann, L. Mußmann, D. Lindner, and W. Müller. Development of Close-Coupled Catalyst Systems for European Driving Conditions. *SAE Technical Paper Series*, (980663), 1998. doi:10.4271/980663.

[73] W. B. Williamson, M. G. Zammit, H. J. Robota, D. J. Ball, and D. G. Linden. Palladium and Platinum / Rhodium Dual-Catalyst Emission Solutions for Close-Coupled or Underfloor Applications. *SAE Technical Paper Series*, (2000-01-0860), 2000. doi:10.4271/2000-01-0860.

[74] K. Yoshizawa, K. Mori, and S. Kimura. Numerical Analysis of the Exhaust Gas Flow and Heat Transfer in a Close-Coupled Catalytic Converter System during Warm-Up. *SAE Technical Paper Series*, (2001-01-0943), 2001. doi:10.4271/2001-01-0943.

[75] L. Zhao, A. A. Moiz, S. Som, N. Fogla, M. Bybee, S. Wahiduzzaman, M. Mirzaeian, F. Millo, and J. Kodavasal. Examining the role of flame topologies and in-cylinder flow fields on cyclic variability in spark-ignited engines using large-eddy simulation. *International J of Engine Research*, 2017. doi:10.1177/1468087417732447.

Acronyms

ADI alternating direction implicit. 32

BDC bottom dead center. 42, 43, 88, 89

Bi Biot number. 64

BMW Bayerische Motoren Werke AG. 29, 31

CAD crank angle. 42, 54

CAFE Corporate Average Fuel Economy. 24

CCV cycle-to-cycle variation. 15, 21, 75–79, 81, 93, 107, 109–112, 118–120, 124–126, 130, 132, 133, 135, 136, 138, 143–147

COV$_{NIMEP}$ covariance of net indicated mean effective pressure. 15, 20, 107–109, 143

CPI cells per square inch. 36

CV control volume. 65–67

EGR exhaust gas recirculation. 77, 125

EPA Environmental Protection Agency. 24

EVC exhaust valve closing. 17, 40, 80, 81, 125

EVO exhaust valve opening. 40, 81

FFID fast flame ionization detector. 38, 42, 43, 46, 51

FTP75 federal test procedure. 8, 24, 27–30

GDI gasoline direct injection. 146

GHG greenhouse gas. 23–25

GIMEP gross indicated mean effective pressure. 89

GM General Motors Company. 8, 21, 36, 38, 39, 41, 79

ICE internal combustion engine. 23, 75

IMEP indicated mean effective pressure. 90

IVC intake valve closing. 40, 81, 131

IVO intake valve opening. 40, 80, 81

KI knock intensity. 13, 20, 92, 142, 143

KL knock limit. 134–136

KLSA knock limited spark advance. 137, 141, 143, 144

LES large-eddy simulation. 77, 78

LEV low emission vehicle. 29, 31

LWI Livengood Wu integral. 19, 20, 133–141, 143, 146

MAP manifold air pressure. 13, 18, 42, 43, 52, 88, 89, 131, 144, 147

MBT maximum brake torque spark timing. 20, 121, 122, 134, 137, 143

NDIR nondispersive infrared detector. 12, 42, 43, 86

NEDC New European Driving Cycle. 24

NIMEP net indicated mean effective pressure. 15, 16, 18, 20, 40, 43, 44, 52, 71, 77, 89, 90, 105, 110, 111, 113, 115, 116, 121, 125, 126, 134, 137, 142, 143, 147

NIST National Institute of Standards and Technology. 11, 21, 62

Nu Nusselt number. 64, 65

NVH noise, vibration, and harschness. 75

PDEs partial differential equations. 31, 67

PID proportional-integral-derivative. 12, 41, 84, 86, 87

PZEV partial zero emission vehicle. 30

RANS Reynolds Averaged Navier-Stokes. 77

SOI start of injection. 126

SV space velocity. 48, 71

TDC top dead center. 80, 91, 143

TWC three-way catalytic converter. 8, 24, 25, 27–29, 32, 33, 35–37, 45, 48, 51, 52, 59, 69, 71, 72

ULEV ultra low emission vehicle. 29

VVT variable valve timing. 30, 39, 80

WOT wide open throttle. 81, 133

Chemical Compounds